CHALMERS

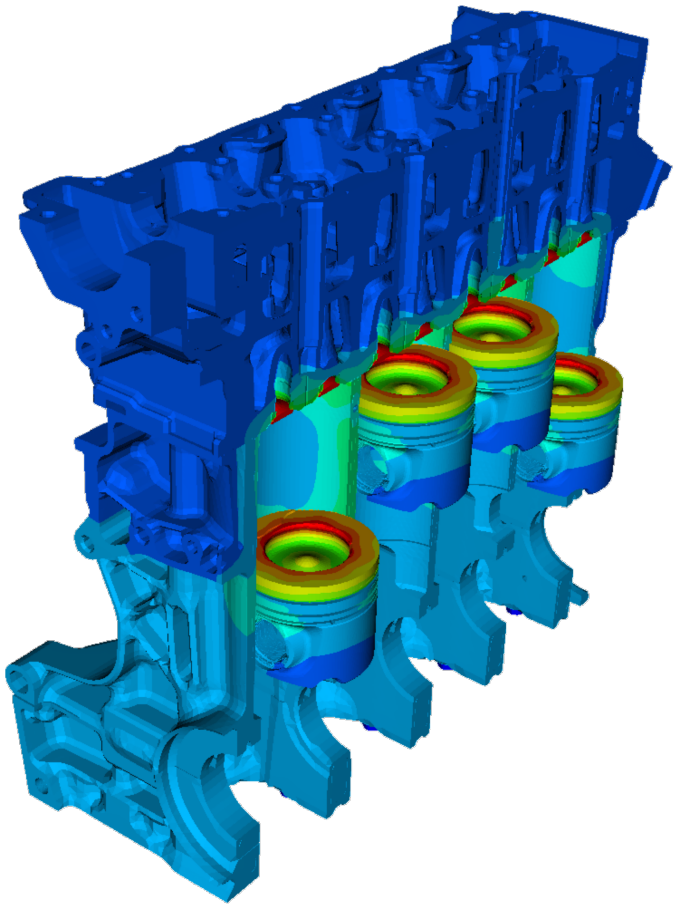

Thermal Analysis of a Diesel Piston and Cylinder Liner using the Inverse Heat Conduction Method

Master's thesis in Applied Mechanics

MARTIN GONERA
OLLE SANDIN

Department of Applied Mechanics
CHALMERS UNIVERSITY OF TECHNOLOGY
Göteborg, Sweden 2015

MASTER'S THESIS IN APPLIED MECHANICS

Thermal Analysis of a Diesel Piston and Cylinder Liner using the Inverse Heat Conduction Method

MARTIN GONERA
OLLE SANDIN

Department of Applied Mechanics
Division of Material and Computational Mechanics
CHALMERS UNIVERSITY OF TECHNOLOGY

Göteborg, Sweden 2015

Thermal Analysis of a Diesel Piston and Cylinder Liner using the Inverse Heat Conduction Method
MARTIN GONERA
OLLE SANDIN

Master's thesis 2015:43
ISSN 1652-8557
Department of Applied Mechanics
Division of Material and Computational Mechanics
Chalmers University of Technology
SE-412 96 Göteborg
Sweden
Telephone: +46 (0)31-772 1000

Cover:
Cross section of a four-cylinder diesel engine.

Chalmers Reproservice
Göteborg, Sweden 2015

Thermal Analysis of a Diesel Piston and Cylinder Liner using the Inverse Heat Conduction Method
Master's thesis in Applied Mechanics
MARTIN GONERA
OLLE SANDIN
Department of Applied Mechanics
Division of Material and Computational Mechanics
Chalmers University of Technology

Abstract

Purpose and scope

As the current trend in car engine development is to create smaller engines with higher specific power outputs to meet the demands of both lower emissions and costumer satisfaction, the thermal loads in engines are increasing.

This Master's thesis developed a thermal analysis model of a diesel piston that is used in Volvo Cars engines. A thermal analysis model of the piston enhances the possibilities to determine the complete thermal loads of the car engine and can be used as a boundary condition when performing combustion CFD-simulation. It may also serve as an aid in piston design.

Method

The development of a thermal analysis Finite Element model of the diesel piston consisted of determining the thermal boundary conditions for varying engine load cases. The thermal boundary conditions were applied to the piston surfaces as convective loads with ambient temperatures and heat transfer coefficients, ***HTCs***. As the ambient temperatures were provided by prior engine simulations or based on qualified assumptions, the main challenge was to calculate the piston boundary heat transfer coefficients. The Inverse Heat Conduction Method, ***IHCM***, was utilized in order to iteratively calibrate the piston boundary HTCs such that the piston temperature field correlated to piston temperature measurement data and such that the heat flux over the piston surfaces resembled quantities determined by the piston manufacturer Mahle. The HTC parameter calibration was executed by the use of optimization. Calibrated heat transfer coefficients were calculated iteratively according to IHCM for various engine load cases. The HTCs then were interpolated between the considered engine load cases in order to obtain a matrix of piston boundary HTCs for a larger number of engine loads.

The thermal analysis piston model was validated for ***rated*** load cases, i.e. load cases for which measurement data exist and ***assumed*** load cases for which no measurement data exist. For the rated load cases, the model was validated by comparing the reference measurement temperatures with the corresponding calculated nodal temperatures and by comparing the heat flux over the piston surfaces to the quantities determined by the piston manufacturer. For the assumed load cases only the heat flux over the piston surfaces was considered.

A method of determining the heat transfer from the piston surface to the engine cylinder liner by applying the transferred heat flux as a thermal load to a complete engine FE-model was created. This operation was performed by extracting the element face heat flux per unit area and mapping it onto the cylinder liner according to the piston movement.

Results

The results from the validations was that, for the intended engine load case span, the piston thermal analysis gave accurate results in terms of the piston structure temperature field and its surface heat flux. Consequently, the authors of this Master's thesis considers this thermal analysis model to generate results of high applicability and believe that the developed method of conducting a thermal analysis of a diesel piston is suitable. The procedure of mapping the element heat fluxes per unit area onto the cylinder liner was validated by reapplying the extracted thermal load onto the piston surface. The results indicated excellent resemblance to the original analysis results. As such, the element heat flux per unit area mapping methodology was considered to be feasible.

Keywords: Thermal analysis, Diesel piston, Cylinder liner, FEM, Inverse Heat Conduction Method, Parameter calibration, Optimization, Heat transfer coefficient

Preface

This Master's thesis was carried out at Volvo Cars Corporation engine development department to fulfill the requirements of a Master's degree in Applied Mechanics at Chalmers University of Technology. The work was conducted during the time period of January to June 2015. Stefan Eriksson, Senior CAE engineer at Volvo Cars, was the supervisor of the Master's thesis work and Professor Kenneth Runesson at Chalmers department of Applied Mechanics, division of Material and Computational Mechanics, was the examiner.

Acknowledgements

We are very thankful for all the experience and knowledge we have gained throughout this Master's thesis work. It has been both exciting and challenging to tackle such a comprehensive problem. Without the help from the personnel at Volvo Cars (and from the delicious coffee in the red coffee-machines), we surely wouldn't have gotten far.

We would especially like to thank Stefan Eriksson for his excellent guidance throughout this Master's thesis. He has been an encouraging support and a tremendous source of knowledge.
A big thank you to Johan Cederlund for sharing his expertise in Python scripting, to Mirko Bovo for patiently answering our questions regarding combustion, to Björn Jonsson for all the help with the vital GT-Power simulations, to Anant Patwari for the overall consulting regarding the thermal loads on a piston, to Akhil Krishnan for an insight regarding piston ring friction and to our examiner Kenneth Runesson. We would also like to thank Charlie Olofsson, Petter Hessö and Fredrik Strömstedt for providing us with important information about the pistons in order to bringing the thesis work forward.
Last but not least we like thank the department manager Anders Thorell and the entire structural- and fluid group for letting us do the Master's thesis work in this department, it has been truly inspiring to work in such a professional environment.

Göteborg, June 2015
Olle Sandin and Martin Gonera

Nomenclature

ρ = density $[\frac{kg}{m^3}]$
μ = dynamic viscosity $[\frac{kg}{sm}]$
k = Thermal conductivity $[\frac{W}{mK}]$
h = Convective heat transfer coefficient $[\frac{W}{m^2K}]$
HTC = Heat Transfer Coefficient $[\frac{W}{m^2K}]$
CFD = Computational fluid dynamics
IHCM = Inverse Heat Conduction Method
FEM = Finite Element Method
FEA = Finite Element Analysis
DFLUX = Distributed flux load $[\frac{W}{m^2}]$. Abaqus defined thermal load.
RFLE = Total heat flux at the node $[\frac{W}{m^2}]$. Abaqus output variable.

Subscripts

CG = Cooling gallery
PRA = Piston Ring Assembly

Contents

1 Introduction

Today, the pistons in Volvo Cars engines are designed by the suppliers based on load data determined by the engine performance targets. From this data the supplier estimates the temperatures of the piston and recommends a design that is suitable for the application. This procedure is successful for the design of the piston, but gives no knowledge of the thermal interaction between the piston and its surrounding parts. The current trend in car engine development is to make smaller engines with higher specific power outputs to meet the demands for lower fuel consumption and emissions. This leads to higher thermal loads on the engine and an increasing need to understand the heat balance of the complete engine in order to optimize the different engine parts and systems. A substantial part of the heat generated by the combustion is transported to the coolant through the piston and to the surrounding structure. It is therefore important to get an accurate description of these interactions. The goal of Volvo Cars future combustion engine development is to increase power and efficiency and decrease fuel consumption while still maintaining reliability and durability of the highest possible level. As such, it is necessary to have a complete image of the thermal effect and how this affects the engine properties.

1.1 Purpose

The main purpose of this Master's thesis is to provide a richer understanding on the subject of how to model heat transfer in a diesel piston and between the piston and the surrounding cylinder liner by delivering an extensive report and a reliable and thorough modelling methodology. The modelling technique is then to be implemented in a Finite Element model of a complete engine, but may also in future research beyond scope the of this Master's thesis be applied to a Computational Fluid Dynamics engine model.

1.2 Limitations

The thermal analysis will be solely conducted through FE-analysis. The results of the FE-analysis will be validated through previous measured thermal test data the piston manufacturer Mahle. The software used for the thermal analysis will be MATLAB, Abaqus, ANSA and modeFrontier, since these are the software available at by Volvo Cars. The Master's thesis is limited to only the thermal interaction between the piston and the cylinder liner with regard to the combustion, the engine coolant flow and the oil cooling mechanism. No other engine components will be considered in this Master's thesis. The Master's thesis will not evaluate fatigue, fracture, deformation or stresses of the piston or the cylinder. The refinement of the results and simulations are limited to the computational capacity available at Chalmers University of Technology and at Volvo Cars Corporation. As this Master's thesis comprises of 30 HP the time frame is limited to the spring semester of 2015 for completion.

1.3 Prerequisites

Volvo Cars did not have a thermal analysis model of diesel pistons prior to this Master's thesis work. The relevant data available for this thesis were the combustion load data from CFD-simulations and diesel piston temperature measurements.

1.4 Approach

The temperature field of the diesel piston is solved iteratively according to the Inverse Heat Conduction method, presented in [11], combined with Finite Element analysis. The initial heat transfer coefficients of the diesel piston used in the iterative procedure of the Inverse Heat Conduction Method are calculated with analytical methods, empirical correlations, numerical methods and qualified assumptions. The Inverse Heat Conduction Method is used in two steps in order to calculate the temperature field of the piston such that certain node temperatures of the FE-model correlate with the corresponding measurement data points and such that the heat flux across the piston boundaries are of magnitudes determined by the piston manufacturer.

Firstly, the heat transfer coefficients of the convective boundary conditions in a 2D axisymmterical piston FE-model are calculated iteratively with an in-house developed MATLAB code that utilizes the Inverse Heat Conduction Method. Secondly, the determined heat transfer coefficients from the 2D axisymmetrical parameter calibration are used as initial heat transfer coefficients when applying the Inverse Heat Conduction Method on a complete 3D piston FE-model. The parameter calibration software used for the second step is modeFrontier and the FE-analysis is performed with Abaqus and ANSA as pre-processor. The two-step parameter calibration procedure is performed for three engine load cases, in which the engine speeds and, consequently, the engine power outputs are increased from 2000 RPM and 100 kW, to 3000 RPM and 135 kW and lastly 4000 RPM and 170 kW. Furthermore, the Inverse Heat Conduction Method is utilized with regard to only the boundary heat fluxes of the piston to calibrate the heat transfer coefficients for a ± 10 kW variation of the engine power output at each of the prior analysed engine speeds.

With nine modeFrontier parameter calibrations, nine sets of heat transfer coefficients for the piston boundaries are obtained. By linear interpolation of the heat transfer coefficients in MATLAB, a matrix of values for every piston boundary condition heat transfer coefficient is obtained which is valid for a large number of engine speeds and engine power outputs in between 2000 RPM to 4000 RPM and 90 kW to 180 kW.

A program for extracting the piston boundary heat flux at each element surface in contact with the cylinder liner is constructed. The element fluxes per unit area are coupled to their element surface centroids and are applied to the cylinder liner with respect to the piston movement. By doing so, the thermal interaction between the piston and the engine cylinder liner can be analysed.

2 Theory

An extensive literature study on thermal energy science was performed for the purpose of acquiring deeper knowledge in the field of diesel piston thermal analyses. General thermal energy- and specific theories for internal combustion engines and pistons were evaluated.

An in-depth investigation of how Finite Element analysis can be utilized for a thermal problem was also performed.

Analytical, empirical and numerical applicable approaches will be presented in this chapter giving an understanding of the physics and solution methodology of the piston thermal analysis.

2.1 Heat transfer

In thermal analysis the main goal is to analyse the transfer of heat flux between systems with different temperatures. These calculations are basically conducted through three main modes of heat transfer: thermal conductivity, thermal convection and thermal radiation. These heat transfer processes can occur separately or combined and differs from each other in how the heat is transferred. These differences will be clarified in subsections 2.1.1, 2.1.2 and 2.1.3.

Two important variables of the heat transfer calculations are the heat flux, $\boldsymbol{q}$, which defines the transferred energy per unit time, and the heat flux per unit area $\boldsymbol{q''}$. These variables are of units Watt, $[W]$, and Watt per square meter, W/m^2. A parameter of great significance for heat transfer calculations is the heat transfer coefficient, abbreviated to HTC in this report, of thermal convection, W/m^2K. This coefficient is denoted by h.

2.1.1 Thermal conduction

Thermal conduction is a heat transfer mode occurring in a continuous material with internal temperature gradients. The rate equation of thermal conduction stated in eq 2.1 is based on Fourier's Law [13]. The conductive heat flux is proportional to the negative temperature gradient $\boldsymbol{\nabla} T$ and the heat flux area, A. The proportionality constant is called thermal conductivity coefficient, k. The conductivity is a material parameter with the units $\frac{W}{mK}$.

$$\boldsymbol{q} = -kA\boldsymbol{\nabla} T \tag{2.1}$$

2.1.2 Thermal convection

Thermal convection occurs across a surface along which a fluid is flowing. The convective heat transfer can be considered as thermal conduction through a fluid film at the flow surface. Convection typically arises at the surface between a solid material and a fluid where no mixing occurs. The heat flux equation of thermal convection is stated in eq 2.2 and expresses the proportionality to the temperature difference between the surface temperature, T_s, and the fluid temperature, T_{amb}, and the heat flux area, A. The heat transfer coefficient, h, is dependent of fluid properties and is a function of several parameters such as the velocity and the viscosity of the fluid.

$$q \overset{def}{=} \boldsymbol{q} \cdot \boldsymbol{n} = hA(T_s - T_{amb}) \tag{2.2}$$

2.1.3 Thermal radiation

Thermal radiation is a heat transfer mode where radiant heat at certain wave lengths are emitted from surfaces of bodies. This heat transfer mode does not require a heat transfer medium and is independent of the ambient temperature. The rate equation of thermal radiation stated in eq 2.3 is expressed from Stefan Boltzmann's law of radiation [13]. F is the view factor from surface 1 to surface 2, A is the area from which the radiation is emitted, σ is the Stefan–Boltzmann constant, and T_1 and T_2 are the surface temperatures.

$$\boldsymbol{q} \cdot \boldsymbol{n} = F\sigma A(T_1^4 - T_2^4) \tag{2.3}$$

2.2 Heat sources in a diesel internal combustion engine

There are several processes within a diesel internal combustion engine which generates heat. The combustion of the fuel converts to work as the expansion of the gases causes the motion of the piston. This combustion can be divided into radiation and convection terms. The radiation is released in the moment of combustion while the convection is related to the gas flow. As the piston moves, the piston skirts and the piston rings slide along the cylinder liner lubricated by oil. This motion in turn creates friction between the faces. The piston skirts and piston rings are shown in Figure 2.1 and Figure 4.7

Based on the literature study conducted for this thesis, the friction of the piston ring assembly can be determined by tribology [20]. The oil film thickness between the liner and piston, the surface roughness, the dynamics of the piston ring and component material properties all are related to the friction. Friction models rely heavily on the Stribeck friction model, which is determined by utilizing measured data and forming a Stribeck curve [24]. According to [10], roughly 1.6% of the complete engine energy input is transformed to frictional mechanical losses in the piston and piston rings, some of which is then contributing to heat generation. This is an insignificant amount of energy compared the total thermal losses, which are 61.7% of the total energy input [10].

Based on gathered information, the heat generation through friction was assumed to be negligible compared the the combustion processes [10].

From the literature study of similar piston thermal analyses, modelling the radiation can be simplified by including its contribution through the convection term [11], [7], [27]. The gas convection from the combustion is the most important heat generation source in an internal combustion engine. The radiation occurs briefly during the combustion of the fuel. If one takes into account the whole cycle of a four stroke diesel engine, the radiation heat contribution is of less importance.

2.3 Heat transfer on the piston combustion side

The piston top is directly exposed to the combustion within the engine cylinder. However, the combustion does not occur uniformly across the diesel piston top. There are temperature variations along both the radial and circumferential direction of the piston top surface [10]. This is due to the way fuel and air is introduced to the cylinder for a diesel engine. As the air is compressed, fuel is sprayed in to the cylinder via the fuel injector. Some parts of the piston top are therefore more directly exposed to the combustion. As the combustion commences, the zones where the combustion propagates to will have a higher temperature than the rest of the piston [5]. A consequence is that the diesel piston will have different heat transfer coefficients, HTCs, along its top surface. As this thesis focus on a detailed thermal analysis, an averaged HTC of the surface is not suitable and a more sophisticated spatial HTC expression is necessary. The piston top surface is shown in Figure 2.1.

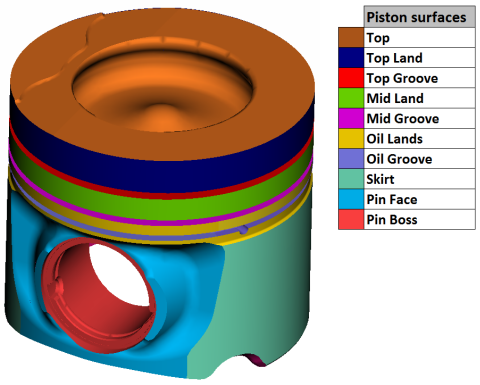

Figure 2.1: Diesel piston.

2.3.1 Empirical correlations

Empirical correlations are constructed by evaluating specific load cases and determining which factors can be utilized for constructing a formula that can express the observed results. While empirical models are usable for the investigated load cases for the specific experimental setup, they are not general in any sense. That is, they might not be versatile enough to be applicable for a broader range for possible load cases than those in which the formula was developed for. Depending on how comprehensive the empirical model is, is directly responsible for its suitability to be utilized for the analysis of interest.

Area-averaged heat transfer coefficient

Engine simulation software, for example GT-Power, is used to perform 1D energy analyses of internal combustion engines and the supporting components. In order to conduct such an analysis, the software needs to be able to determine an area-averaged heat transfer coefficient of the combustion chamber.

GT-Power uses a modified empirical heat transfer model developed initially by Woschni [26] and shown in eq 2.4.

$$h_a = \alpha d^{-0.2} p(t)^{0.8} T(t)^{-0.53} [C_1 c_m + C_2 * \frac{V_s T_1}{p_1 V_1}(p(t) - p_0)]^{0.8} \tag{2.4}$$

Here h_a is the instantaneous area-averaged heat transfer coefficient of the piston top surface, α is a constant dependent on the engine geometry, d is the cylinder bore, p is the cylinder pressure, T is the gas temperature, c_m is the mean piston velocity, p_1, T_1 and V_1 are known values for the gas pressure, temperature and the instantaneous cylinder volume at a known point of the work cycle of the engine, for example intake closure or combustion. p_0 is the motored pressure and V_s is the cylinder volume. The constants C_1 and C_2 take different values depending of which moment of the work cycle that is investigated. Based on this formula, the averaged HTC, h_c, can be determined by integrating the Woschni expression over the total work cycle.

$$h_c = \frac{1}{720} \int_0^{720} h_a d\varphi \tag{2.5}$$

Similarly to the Woschni correlation, Hohenberg constructed an empirical approach for determining the area-averaged heat transfer coefficient on the piston top surface [12]. The Hohenberg correlation is stated in eq 2.6, where C_1 and C_2 are geometry dependent constants, V_C is the cylinder volume, p is the cylinder pressure, T is the mean gas temperature and $\bar{v}_p$ is the mean piston speed.

$$h = C_1 V_C^{-0.06} p^{0.8} T^{-0.4} (\bar{v}_p + C_2)^{0.8} \tag{2.6}$$

According to [12], the Hohenberg correlation is an improvement of the Woschni correlation such that eq 2.6 gives better correlation over the entire set of engine cycles.

Annand and Ma developed an instantaneous heat transfer model [4] where the convection term states:

$$h = (k/D) Re^{0.7} (0.12 - 0.2 \frac{dT_g}{dt} \frac{1}{\omega} \frac{1}{T_g - T_w}) \tag{2.7}$$

Here D is the engine bore, k is the thermal conductivity of working fluid, Re is the Reynolds number, T_g is the bulk mean temperature of working fluid, ω is the angular rotation rate of engine crankshaft and T_w is the surface wall temperature. While there are newly developed heat transfer models for internal combustion engines, the presented ones are most commonly used for diesel engines [9].

Radial distribution of area-averaged HTC

With an area-averaged surface HTC, an empirical formula developed by Seale and Taylor [14] can be applied to derive the HTC along the radial direction of the top surface of a diesel piston.

Seale's formula states:

$$\begin{aligned} &\text{for} \quad r < N \qquad h(r) = \frac{2h_c}{1 + e^{0.1N^{1.5}}} e^{0.1r^{1.5}} \\ &\text{for} \quad r > N \qquad h(r) = \frac{2h_c}{1 + e^{0.1N^{1.5}}} e^{0.1(2N-r)^{1.5}} \end{aligned} \tag{2.8}$$

In eq 2.8, r is the distance from the centre line of the piston, N is the distance from centre line to position of maximum temperature and h_c is the cycle averaged HTC on the piston head. The N-point location is determined by using measured data, i.e where the highest measured temperature on the top surface of the piston is located.

See Figure 2.2 for an example of the distribution of the HTC along the radial direction on the piston head based on Seale and Taylor formula.

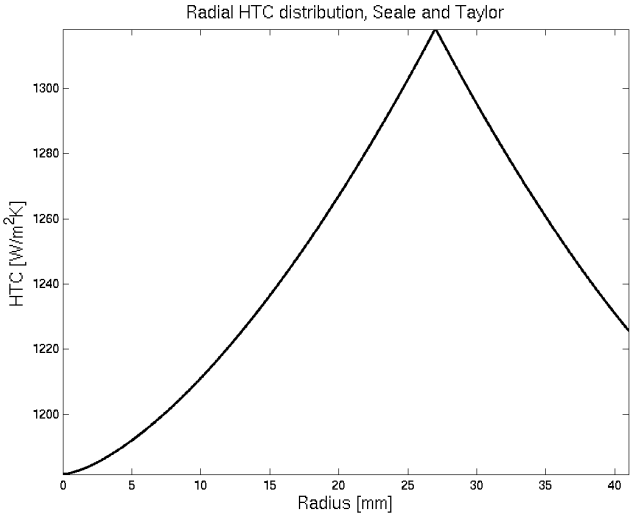

Figure 2.2: Radial HTC distribution, Seale and Taylor.

2.3.2 Numerical approach

The combustion in an internal combustion engine can be analysed through numerical analysis of Navier–Stokes equations with the Computational Fluid Dynamics method, CFD. For the CFD analyses it is necessary to properly define geometrical bounds, physical properties of motion, enthalpy and radiation etc. as well as the boundary conditions [5].

2.4 Heat transfer in piston cooling galleries

The piston is exposed to high temperatures during the combustion. It is therefore necessary to keep the piston cooled as the thermal stresses otherwise would be too high and failure of the piston would occur. Some pistons are designed with a cooling gallery in the structure to keep it within safe temperatures. An oil jet is sprayed underneath the piston and enters the cooling gallery inlet. The oil then flows within the gallery and exits from an outlet. This takes place continuously during the work cycle. As one can imagine, this oil flow is very complicated to model. Factors such as splashing and fill ratio heavily affect the cooling properties [10]. Previous studies derive the oil flow properties by CFD simulations and empirical correlations [6], [22], [28]. The piston cooling gallery is shown in Figure 2.3.

2.4.1 Empirical method

An empirical model for determining the heat transfer coefficient in the oil cooling gallery was developed by Bush [6]. The Bush formula shown in eq 2.9 takes into account the characteristics of the flow and calculates an area-averaged Nusselt number for the cooling gallery. Depending of the Prandlt number of the oil flow, the

equation has different expressions.

$$\begin{aligned} &\text{For} \quad P_r > 0.5 \qquad N_{Bush} = 0.495 Re^{0.57} (D_c)^{0.24} (P_r)^{0.29} \\ &\text{For} \quad P_r << 1 \qquad N_{Bush} = 0.638 (RePr)^{0.5} (D_c)^{0.24} \end{aligned} \tag{2.9}$$

Re is Reynolds number, P_r is Prandtl number, D_c is the characteristic diameter of the cooling gallery. The Reynolds number is defined as shown in eq 2.10, where V_s is the mean relative piston speed and ν is the kinetic viscosity of the oil fluid.

$$Re = \frac{V_s D_c}{\nu} \tag{2.10}$$

With the Nusselt number calculated, the heat transfer coefficient can be determined by eq 2.11

$$h_{CG} = k N_{Bush} \tag{2.11}$$

Here, h is the area-averaged heat transfer coefficient for the cooling gallery and k is the fluid conductivity.

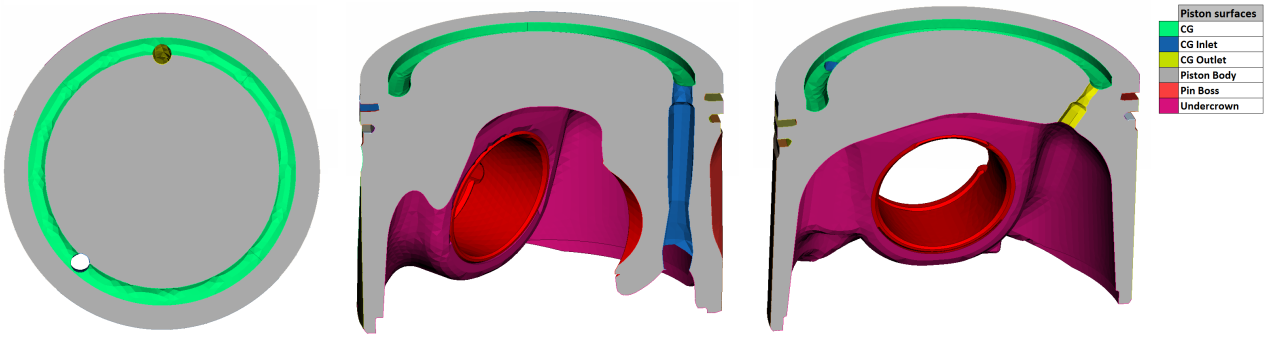

Figure 2.3: Cooling gallery sections.

Another empirical model to describe the heat transfer for cooling gallery was developed by French [8] and is presented in eq 2.12. In eq 2.12, μ_c and μ_w are the dynamic viscosities of the cooling oil at the inlet and outlet respectively of the cooling gallery, while Re is the Reynolds number, Pr is the Prandtl number, D is the cooling gallery cylindrical diameter and H is the piston cavity length.

$$N_{French} = Re^{0.54} Pr^{1/3} (D/H)^{1/3} (\mu_c/\mu_w)^{0.14} \tag{2.12}$$

2.4.2 Numerical approaches

As with the combustion, the cooling of the piston can be analysed with CFD. Compared to empirical methods, this gives a spatial resolution of the heat transfer properties of the cooling gallery and is not based on previous piston designs and specific load cases. Prior work in CFD heat transfer analyses of the oil cooling gallery, [22] and [28], has determined the spatial variation of the heat transfer coefficients in the oil cooling gallery.

2.5 Heat transfer of the piston undercrown

The heat transfer properties of a diesel piston undercrown are complex due to the piston geometry, fluid composition and varying flow characteristics. No analytical or empirical equation describing the undercrown heat transfer phenomena for a cooling gallery designed piston were found during the literature study. What should be noted is that correlations for area-averaged heat transfer coefficients for oil jet cooled pistons has recently been modelled [3]. However, due to the big difference in cooling method for a piston with a cooling gallery compared to an oil jet spray cooling mechanism, the correlation was determined as unsuitable for the diesel piston thermal analysis of this thesis. One might consider the piston undercrown as a turbulent flow in a circular tube in the most simplified case based on Nusselt number correlations [13]. The piston undercrown is shown in Figure 2.4.

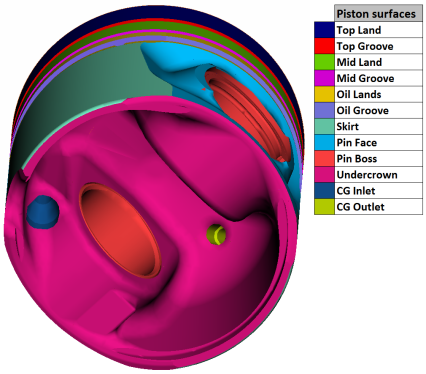

Figure 2.4: Diesel piston undercrown.

2.6 Heat transfer of the piston ring assembly

A substantial part of the heat flux from the piston to the cylinder liner is through the piston ring assembly [10]. The piston ring assembly can be seen in Figure 2.5 and consists of three ring grooves, where the piston rings are installed and the ring lands. A close up illustration of the piston ring and ring groove is shown in Figure 4.7. The space between the piston rings and the cylinder liner is supposed to be small enough to prevent blow-by of the combustion gases and large enough to ensure a smooth piston movement in the cylinder. Along with a smooth cylinder liner surface, engine oil is applied to the liner surface in order to reduce the friction between the piston rings and the liner.

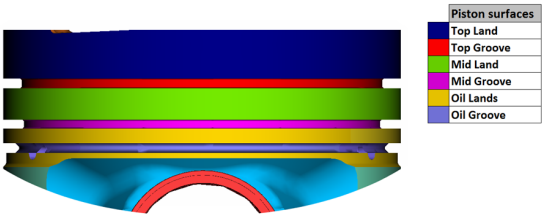

Figure 2.5: Diesel piston PRA.

The heat flow through the piston ring to the cylinder liner is complex to model analytically due to a large number of circumstances that occurs under a four-stroke cycle which all can affect the heat flow. A number of these circumstances are presented below.

- Varying oil film thickness affects the thermal conductivity of the oil and causes surface-to-surface contact between the piston rings and the cylinder liner.
- The rings may twist during a stroke and change the contact geometry.
- Piston ring manufacture tolerances can vary and affect the clearance between the ring and the liner.
- Surface-to-surface or hydrodynamic friction may arise in the ring-liner interaction and raise the oil and surface temperatures.
- Tilting of the piston varies the amount of contact between the piston rings circumferentially.
- Combustion gases may penetrate the top land crevice and locally increase the heat flux input to the piston top land.
- Thermal expansion of the piston and the piston rings changes the piston- and the piston ring geometry.
- Combustion gas blow-by will affect the heat transfer by adding convective heat transfer to both the piston and the cylinder liner.

The mentioned factors vary from each position of the engine cycle and load case.

Consequently, the heat transfer between the piston and the cylinder liner is brought about by both convection and conduction. However, a common assumption of the heat transfer in the piston ring assembly is that, due to the small clearances between the ingoing components, heat transfer occurs through conduction only [16]. This assumption reduces the number of variables needed for determining the energy flow. See eq 2.1 for a general expression of heat conduction.

The heat transfer through conduction is analytically modelled by the use of the thermal circuit method [13]. The thermal circuit method uses material properties and geometrical information to calculate the thermal resistance of the heat transfer medium.

2.6.1 Heat transfer of the piston top land

The piston top land is shown in Figure 2.5 and is the surface between the top ring groove and the piston top surface. This area is of large interest when performing a thermal analysis of the piston and the energy flow from the piston to the cylinder liner, as this area is subjected to large thermal and mechanical loads [10].

The piston top land is one of the piston sections that generally experiences high body temperature since it is close to the combustion. The high body temperatures cause the top land area to thermally expand. The thermal expansion may cause the piston to pinch between the cylinder walls if enough clearance is not given for the piston top land to the cylinder liner. This clearance will lower the conductive heat transfer from the top land to the cylinder liner, while letting combustion gases into the piston top land crevice will cause convective heat transfer. The heat transfer modelling in this area may therefore be assumed to consist of only heat convection for low loads while due to the thermal expansion the heat transfer for high loads can be assumed to be conductive. One must consider that combustion gases may intrude the top land crevice and supply thermal energy to the piston. However, conductive heat transfer is usually assumed for the top land [16].

2.7 Heat transfer in the piston skirt

The piston skirts are shown in Figure 2.5. Piston skirts appear at the thrust- and anti-thrust-side of the piston. Their main functionality is to prevent large tilting of the piston during the four-stroke cycle. Similarly to the piston ring assembly, the skirts may experience uncontrollable effects that changes the heat transfer. However, a common assumption is that only conductive heat transfer occurs at the piston skirts [16].

2.8 Piston heat balance

During the engine strokes, the piston is subjected to several thermal loads. The major heat flux input is generated by the combustion. The heat is then led by the piston to its oil cooling mechanism, the piston surfaces facing the cylinder liner and the piston undercrown ambient oil and air mist. Additional heat generation from friction is, as previously mentioned, disregarded in this thesis due to its insignificant contribution to the piston heat balance. Guidelines on the amount of heat flux distributed by the piston surfaces were found in the piston manufacturer Mahle technical book *Pistons and engine testing* [10]. Table 2.1 illustrates the percentual heat flux distribution of the piston surfaces. The percentual distribution of the heat flux is related to the total heat flux input from combustion.

Piston boundary	[%]
Oil cooling gallery	50-60
Piston ring assembly	10-30
Skirt	5-10
Undercrown	5-15
Pin Face	0-5
Pin Boss	0-10

Table 2.1: Distribution of heat flow from the piston surfaces.

2.9 Heat transfer analysis using the Finite Element Method

In order to perform a multidimensional heat transfer analysis the Finite Element Method can be utilized. This type of solution method is based on the use of elements which represents the body of the object. Each element expresses the physical, geometrical and material properties of the structure. The elements consists of nodes in which a shape function describes the node value changes along the elements. The number of nodes of an element can vary, but generally three- or four node elements are used in a 2D-analysis, while for 3D-analysis four- or eight node elements are commonly used. Depending on the type of analysis that is conducted, each node has a certain number of degrees of freedom.

2.9.1 General FE-formulation of heat transfer analysis

The strong form of the multidimensional heat flow problem was stated in [21] and shown in eq 2.13.

$$\begin{aligned} div(\boldsymbol{D}\boldsymbol{\nabla}T) + Q = 0 \quad & in \quad V \\ \boldsymbol{q}''^{T}\boldsymbol{n} = q'' \quad & on \quad S_q \\ T = g \quad & on \quad S_g \\ q'' = h(T - T_{amb}) \quad & on \quad S_c \end{aligned} \tag{2.13}$$

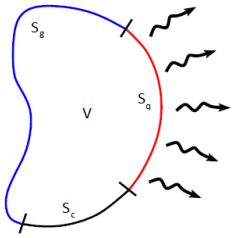

Figure 2.6: Body with defined boundaries.

Here $\boldsymbol{D}$ is the constitutive matrix, $\boldsymbol{\nabla}T$ is the temperature gradient, Q is the external heat supply, q_n'' is the heat flux per unit area, $\boldsymbol{n}$ is the normal vector, T is the temperature, h is the convective heat transfer coefficient, and T_{amb} is the ambient temperature. S_q, S_g and S_c are the boundaries of the body. By multiplication with a test function, v and integration over the volume, the weak form of the heat transfer problem can be expressed as stated in eq 2.14.

$$\begin{gathered} \int_V (\nabla v)^T \boldsymbol{D}\boldsymbol{\nabla}T \, dV = -\int_{s_q} vh \, dS - \int_{s_g} vq'' \, dS + \int_V vQ \, dV \\ T = g \quad on \quad S_g \end{gathered} \tag{2.14}$$

In a thermal analysis each node have one degree of freedom since the temperature in a node is a scalar entity.

After defining the weak form of the heat transfer problem, the problem is discretized into a finite number of elements as shown in eq 2.15.

$$T = \boldsymbol{N}\boldsymbol{a} \tag{2.15}$$

Here $\boldsymbol{N}$ is the shape function vector. The shape functions represents the variation of the temperature in an element. The shape functions can have different polynomial order to represent the interpolation of the nodal temperatures in the element. First order shape functions give a linear temperature distribution between the element nodes, while higher order shape functions will give higher resolution on the temperature distribution. However, the use of higher order shape functions increases the computational cost [1]. Further information about element types and usage is described in subsection 2.10

The stiffness (conductivity) matrix $\boldsymbol{K}$ describes the internal heat transfer by conduction in the body. Equation

2.16 from [21] defines the stiffness matrix. $\boldsymbol{B}$ is defined in eq 2.17 and $\boldsymbol{D}$ is the constitutive matrix.

$$\boldsymbol{K} = \int_V \boldsymbol{B}^T \boldsymbol{D}\boldsymbol{B}\, dV \tag{2.16}$$

$$\boldsymbol{B} = \boldsymbol{\nabla}\boldsymbol{N} \tag{2.17}$$

The constitutive matrix $\boldsymbol{D}$ was expressed as for isotropic materials in [21] and shown in eq 2.18

$$\boldsymbol{D} = \begin{bmatrix} k & 0 \\ 0 & k \end{bmatrix} \tag{2.18}$$

The load vector $\boldsymbol{f}$ consists of the nodal load. In a heat flow analysis the loads are applied as heat flux per unit area at a certain boundary or as a heat source in the body. Equation 2.19 shows the FE-formulation of the load vector which comprises both boundary load in terms of heat flux per unit area, convective heat flow and body load as a heat source.

$$\boldsymbol{f} = -\int_S \boldsymbol{N}^T q''\, dS - \int_S \boldsymbol{N}^T h T_{amb}\, dS + \int_V \boldsymbol{N}^T Q\, dV \tag{2.19}$$

The weak form can then be rewritten as eq 2.20, from which the unknown nodal values $\boldsymbol{a}$ are numerically solved.

$$\boldsymbol{K}\boldsymbol{a} = \boldsymbol{f} \tag{2.20}$$

As stated in eq 2.2 the heat flux from convection is a function of the temperature difference between the surface temperature and the ambient temperature of the surrounding fluid. Since the surface temperature is unknown at this certain boundary, the stiffness matrix at these certain boundary elements is modified to involve the influence of convection. According to [21], the convective stiffness matrix $\boldsymbol{K}_c$ is defined as shown in eq 2.21. The nodal values then are solved from eq 2.22 with the modified stiffness matrix.

$$\boldsymbol{K}_c = \int_S h \boldsymbol{N}^T \boldsymbol{N}\, dS \tag{2.21}$$

$$(\boldsymbol{K} + \boldsymbol{K}_c)\boldsymbol{a} = \boldsymbol{f} \tag{2.22}$$

Additionally, boundary conditions are applied as prescribed boundary temperatures stated in equation 2.13.

2.9.2 Axisymmetrical heat transfer analysis

A structure can in a simplified case be considered to be symmetric about its rotational axis. This gives an axisymmetric structure with symmetry in its circumference and no symmetry with its radius and height. While this axisymmetrical assumption might not completely resemble the actual structure, the assumption enables to perform simulations that are computationally cheap compared to a 3D simulation.
The Finite Element formulation differs in some senses for an axisymmteric analysis compared to a 2D- or 3D FE-analysis. In an axisymmetric analysis one can assume an infinitesimal piece of the structure circumference and perform what can be regarded as a 2D-analysis of the structure's cross section. However, by concerning the element radius, the volume of the infinitesimal slice of the structure is considered. The formulation of the stiffness matrix, the convective stiffness matrix and the load vector for an axisymmetric heat transfer analysis was given in [23] and shown in eq 2.23, 2.24 and 2.25.

$$\boldsymbol{K} = 2\pi \int_S \boldsymbol{B}^T \boldsymbol{D}\boldsymbol{B} r\, dS \tag{2.23}$$

$$\boldsymbol{K}_c = 2\pi \int_L h \boldsymbol{N}^T \boldsymbol{N} r\, dL \tag{2.24}$$

$$\boldsymbol{f} = -2\pi \int_L \boldsymbol{N}^T q'' r\, dL - 2\pi \int_L \boldsymbol{N}^T h T_{amb} r\, dL + 2\pi \int_S \boldsymbol{N}^T Q r\, dS \tag{2.25}$$

The element stiffness matrix, $\boldsymbol{K}^e$, can be constructed according to eq 2.26 and the integration of the element stiffness matrix are preferably performed using isoparametric mapping and Gauss point integration as described in [21].

$$\boldsymbol{K}^e = 2\pi \int_S \boldsymbol{B}^{T,e} \boldsymbol{D}\boldsymbol{B}^e r^e\, dS \tag{2.26}$$

2.10 Thermal element types

The elements used in FE-models can vary in number of nodes and shape functions that define the interpolation. The dimension of the problem, the level of accuracy of the analysis and the material behaviour define which element type should be used [1]. Since only thermal analysis is conducted throughout this Master's thesis no locking effects or incompressibility instabilities can occur and these effects are therefore not considered when choosing the element type for the thermal FE-analysis.

2.10.1 Degrees of freedom for thermal elements

The nodal variable of an uncoupled thermal FE-analysis is the nodal temperature. As the temperature is a scalar entity in a node, the nodes simply have one degree of freedom. In the Abaqus solver, the temperature degree of freedom is denoted the number "11" [1].

2.10.2 Element nodes

The element node number defines the number of nodes the continuous element consists of and the geometry of the element. A direct distinction is made between two-dimensional and three-dimensional elements.

2D-elements

A continuous 2D-element consists of a two-dimensional set of nodes and a defined element thickness. 2D-analysis are used when the through thickness response are disregarded and is beneficial from a computational point of view since the number of degrees of freedom is reduced compared to a 3D-analysis. The thermal 2D-elements provided by Abaqus are shown in Figures 2.7 to 2.10.

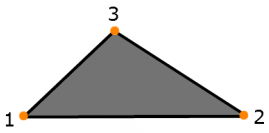

Figure 2.7: Three-node linear 2D-element.

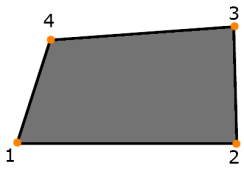

Figure 2.8: Four-node isoparametric bilinear 2D-element.

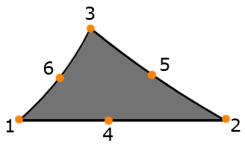

Figure 2.9: Six-node quadratic isoparametric 2D-element.

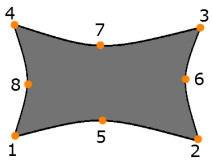

Figure 2.10: Eight-node quadratic isoparametric 2D-element.

As seen in Figure 2.9 and Figure 2.10 additional nodes are positioned between the edge nodes of the element. The use of second order elements consequently increases the numner of degrees of freedom of the FE-model and, therefore, increases the resolution and accuracy of the nodal and element variable output. On the other hand, a higher number of degrees of freedom increases the computational costs [1]. The higher order element also need more integration points in order to integrate the element functions accurately which further increases the computational effort.

The shape function which describes the nodal value interpolation between the element nodes is of first or second polynomial order if the element is linear or quadratic, respectively. The higher the polynomial order, the more accurate is the approximation. An example of element shape functions can be seen in eq 2.27 which describes the special case of rectangular four-node 2D-element with linear interpolation, which corresponds

to the isoparametric extension of the rectanglar element shown in Figure 2.8. a and b in eq 2.27 denote the element side lengths, while y and x are the coordinates in space and x_i and y_i are the nodal coordinates.

$$\begin{aligned} N_1^e &= \frac{1}{4ab}(x - x_2)(y - y_4) \\ N_2^e &= \frac{1}{4ab}(x - x_1)(y - y_3) \\ N_3^e &= \frac{1}{4ab}(x - x_4)(y - y_2) \\ N_4^e &= \frac{1}{4ab}(x - x_3)(y - y_1) \end{aligned} \tag{2.27}$$

3D-elements

Solid elements are used for 3D Finite Element analyses. Solid elements can take different shapes such as triangles, quadrilaterals, tetrahedrals, triangular prisms, hexahedrals and cylindrics. Depending of the geometry of the structure which the FE-analysis is to performed at, some element types are more suitable than others. Triangular and tetrahedral elements are geometrically more versatile than for example quadrilaterals and hexahedral elements [1]. These elements are therefore more suitable to be applied for complex shapes. Solid elements can be expressed as first or second-order elements. Second-order elements can capture the nodal value more accurately than first-order elements at the cost of being more computationally expensive [1].

The choice of element type depends on the analysis type, the computation capabilities available and the needed results preciseness. Commonly used solid elements are shown in Figures 2.11 to 2.17.

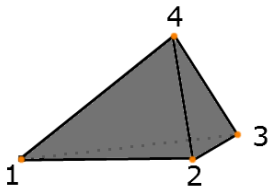

Figure 2.11: Solid four-node linear element.

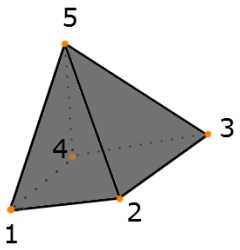

Figure 2.12: Solid five-node linear element.

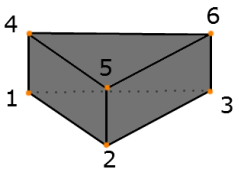

Figure 2.13: Solid six-node linear element.

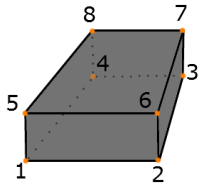

Figure 2.14: Solid eight-node linear element.

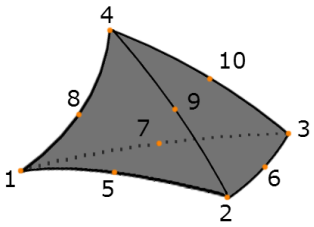

Figure 2.15: Solid ten-node quadratic element.

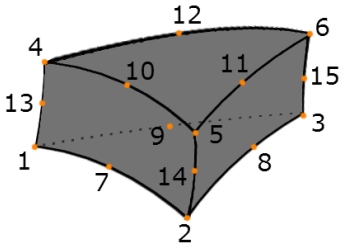

Figure 2.16: Solid 15-node quadratic element.

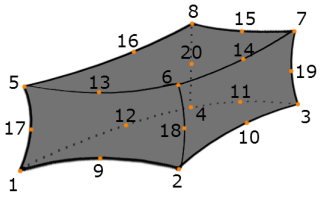

Figure 2.17: Solid 20-node quadratic element.

2.11 Inverse heat conduction method

The Inverse Heat Conduction Method, $IHCM$, is a method in which unknown boundary conditions can be determined through an iterative approach. IHCM calculates the temperature field of the body and compares the calculated values to a predetermined temperature field.

The principle for IHCM is described in [11]:

- One starts of with initial HTCs which are estimates of the actual HTCs.
- The HTCs are then applied in a simulation, such as a thermal FE-analysis of a structure.
- The calculated temperature field is then compared to experimental temperature measurements.
- If the difference between the calculated and the measured temperature is too great, the HTCs are adjusted and the simulation is redone.
- When the difference between the calculated and measured temperate field is acceptable, the iteration procedure is complete.

See Figure 2.18 for a visualisation of the method procedure.

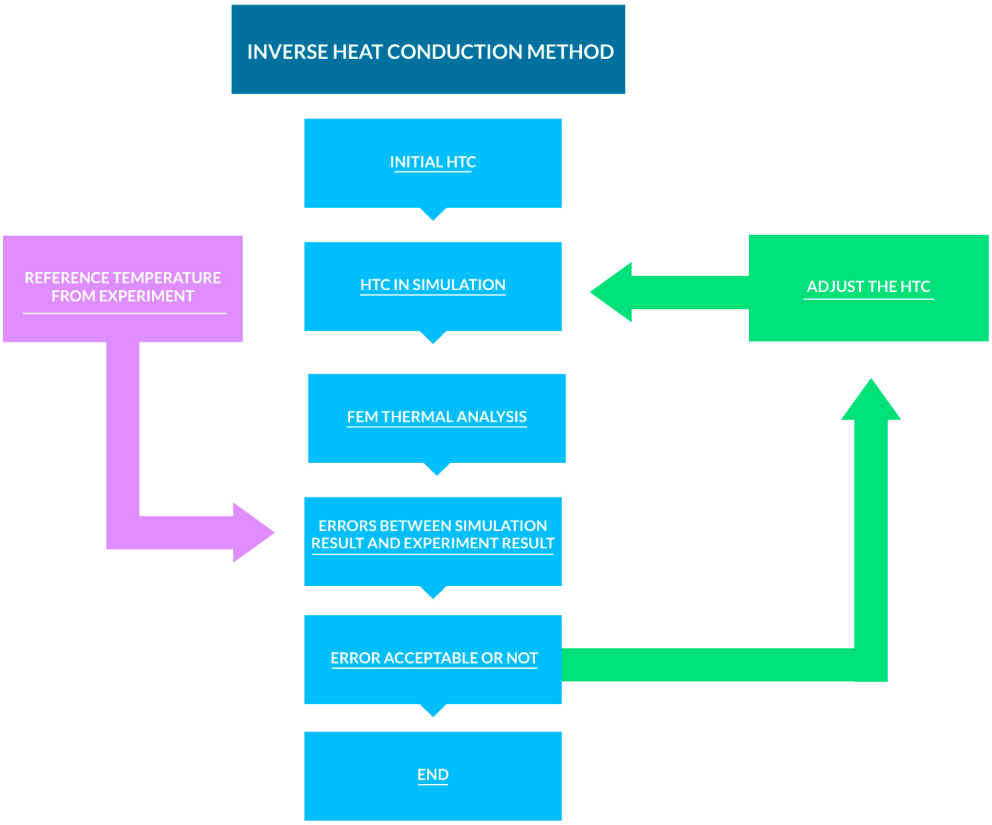

Figure 2.18: Flowchart of the inverse heat conduction method.

2.11.1 Optimization

When using optimization, the goal is to find the optimal value(s) of ingoing variable(s) in order to either minimize or maximize one or several objective functions, f_{obj}. For a thermal analysis, the Inverse Heat Conduction Method is suitable as explained in section 2.11 as it uses optimization in order to find optimal values of the piston boundary HTCs such that the temperature difference between the calculated and measured temperatures is minimized.

Optimization is conducted through mathematical algorithms such as the Nelder-Mead simplex algorithm and the Levenberg-Marquardt algorithm. Depending on which algorithm is utilized, the objective function can have different expressions, such as scalars or vectors. The temperature difference in the measurement/analysis points are preferably gathered in a temperature residual vector, $\mathbf{r}_T$, shown in eq 2.28, where $\mathbf{T}_m$ is a vector with the measurement data and $\mathbf{T}_a$ is the vector with the corresponding calculated temperatures. Examples of gathering the temperature residual response to scalar form can be seen in eq 2.29, which shows the sum of square of $\mathbf{r}_T$, while eq 2.30 show the root-mean-square of $\mathbf{r}_T$.

$$\mathbf{r}_T = \mathbf{T}_m - \mathbf{T}_a \tag{2.28}$$

$$f_{obj} = \sum_{i=1}^{n} \mathbf{r}_T^2 \tag{2.29}$$

$$f_{obj} = \sqrt{\frac{1}{n} \sum_{i=1}^{n} \mathbf{r}_T^2} \tag{2.30}$$

Nelder-Mead simplex algorithm

The Nelder-Mead simplex algorithm is an optimization algorithm that minimizes a scalar nonlinear function (such as the root-mean-square of the temperature residual) with multiple variables without the use of gradient-based search, i.e. it is classified as a direct search method as described in Lagarias et al [15]. It is widely used in engineering applications due to its efficiency and speed in minimizing the objective function, as well as that the direct search method enables minimization of functions without derivatives.

The Nelder-Mead simplex algorithm creates a simplex of dimension $n + 1$ with the n-number of variables as its vertices around the initial values of the variables. The simplex is then modified by reflecting, expanding, shrinking and contracting the simplex until the n-number of variables have optimal values in order to minimize the objective function. The Nelder-Mead simplex algorithm is an unconstrained optimization algorithm, hence no bounds or constraints on the variables are used. However, usages of the Nelder-Mead simplex algorithm exists that takes bounds and constraints into consideration by comparing points in the simplex and rejects points according to certain restrictions [25]:

- If two points both give feasible design, the one with lowest objective function is chosen.
- Always choose a feasible point over an unfeasible point.
- If both point are unfeasible, the point with the lowest objective function is chosen.

The Levenberg-Marquardt algorithm

A least-squares problem is generally defined as finding the minimizing variable vector of a sum-of-squares function, e.g. the sum-of-square of the temperature residual expressed in eq 2.29. An effective optimization algorithm used for solving nonlinear least-squares problems is the Levenberg-Marquardt algorithm [18]. The Levenberg-Marquardt algorithm successfully interpolates the Gauss-Newton and the steepest-descent methods for determining the search direction of each iteration step towards minimizing the objective function. The Gauss-Newton method utilizes second-order Taylor series expansion of the objective function and uses its Jacobian to determine the minimizing search direction. However, if the Jacobian is ill-conditioned, which often is the case in non-linear parameter calibration problems, convergence cannot be ascertained [2]. Thus, in order to ensure a decreasing objective function for each iteration step, Levenberg-Marquardt combines the Gauss-Newton search algorithm together with the steepest descent method. The steepest-descent method is an unconstrained gradient based search algorithm which determines the search direction according to the first derivative of the function it minimizes. If the derivatives of the objective function is either increasing or decreasing, a step is taken in either minimization or maximization of the objective function. Consequently, a regularization parameter is determined that modifies the influence of the respective search methods such that the objective function is decreasing for each iteration step.

A benefit of using the Levenberg-Marquardt algorithm for optimization problems with a large number of parameters is its ability to disregard parameters with small or none influence on the objective function. However, as the Levenberg-Marquardt algorithm utilizes gradient based search it cannot handle discontinuous functions and bound constraints.

3 Solution Strategy

This chapter will briefly give an explanation of the solution strategy.

As no analytical or empirical methods of calculating the thermal loads of the piston yielded precise results, the Inverse Heat Conduction Method was utilized for determining the HTCs on the piston boundaries. Since determining the piston boundary HTCs by optimization is complex, due to its large number of variables, the HTC parameter calibration was divided into two steps, 2D axisymmetrical- and 3D parameter calibration. Furthermore, interpolation of the HTCs was performed after the parameter calibration as an attempt to construct a complete thermal analysis piston model. As this solution strategy consists of several steps, following lists and Figure 3.1 clarifies the solution strategy work flow:

1. Calculated initial piston boundary HTCs according to analytical methods, empirical correlations or assumed a HTC values for the piston boundary condition.

2. Performed a HTC parameter calibration with the in-house developed MATLAB program on a 2D axisymmetrical piston FE-model. This was done for load cases at which temperature measurement data existed. The objective function was the root-mean-square of the temperature residual $\mathbf{r}_T$, as eq 2.30. The constraints were the heat fluxes over the piston boundaries according to the Mahle data presented in section 2.8.

3. Performed a HTC parameter calibration on a 3D diesel piston FE-model with modeFrontier. The calibrated HTCs obtained from the 2D axisymmetrical parameter calibration were in this step served as initial variables. The 3D parameter calibration was performed for:

   (a) Load cases at which measurement temperature data existed. The objective function was the root-mean-square of the temperature residual $\mathbf{r}_T$. The constraints were the heat fluxes over the piston boundaries.

   (b) Assumed loads of ± 10 kW from the rated engine loads at which temperature measurements existed. The objective function was the difference between the calculated heat flux across the piston top surface and the input heat flux according to GT-Power simulations. The constraints were the heat flux guidelines defined by Mahle over the piston boundaries. Depending on an increase or decrease of engine power output, additional constraints of increased or decreased temperature field were set.

4. The fourth step was to linearly interpolate the HTCs between the calibrated load cases to construct a complete thermal analysis piston model.

The steps above will be presented in depth in chapters 4 to 6.

When finalizing step three, parallel work with mapping the element heat flux per unit area from the piston surfaces facing the cylinder liner commenced. The piston heat flux mapping is explained in the following list and further described in chapter 7:

1. Extracted the total node heat flux (denoted RFLE in Abaqus [1]) from the FE-analysis results and summed the total node heat flux for each element surface face.

2. Calculated the element surface face area and its surface center coordinate and coupled the element ID and center coordinate to its corresponding sum of total node heat flux.

3. By dividing the total heat flux of the element with its surface face area, the heat flux per unit area of the element surface face was calculated.

4. By the use of a modified in-house mapping routine the element face heat flux per unit area was mapped onto the cylinder liner in a complete thermal analysis FE-model of the engine with respect to piston movement.

Figure 3.1 displays the order of the solution strategy steps and what software were used for each respective step.

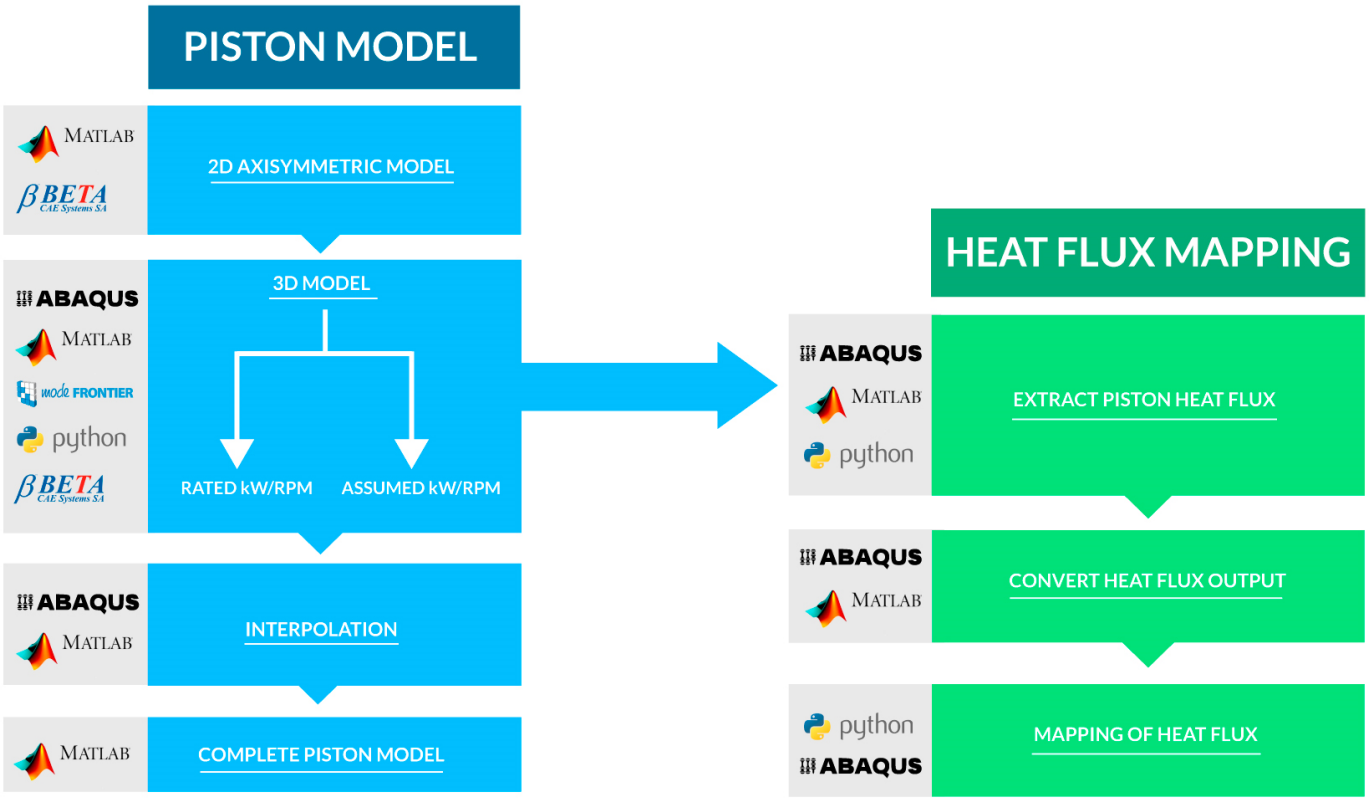

Figure 3.1: Solution strategy flowchart.

4 2D axisymmetrical thermal analysis

A 2D axisymmetric model was utilized in the initial stages of the thesis to give an overall understanding of how the different thermal loads affect the piston temperature field and as a base for the complete 3D thermal analysis, explained in section 5. Figure 4.1 shows the step in the solution strategy.

Figure 4.1: Solution strategy: 2D axisymmetrical model.

Since the actual diesel piston is not an axisymmetrical structure and the thermal boundary conditions varies with the circumference, this assumption was known to give errors in the parts not similar to the considered cross-section. The benefit of constructing a simplified 2D axisymmetrical model was to be able to perform many thermal FE-analyses quickly and time efficiently.

The piston cross-section used for the 2D axisymmetrical FE-model was the part of the piston with a covering skirt. This cross-section was meshed with four-node linear elements, see Figure 2.8 in section 2.10, and a coarse mesh was used to avoid computationally costly analysis. The meshed cross-section can be seen coloured blue in Figure 4.2.

The initial boundary HTCs for the piston were calculated by either analytical methods, empirical correlations, numerical methods or qualified assumptions. The model was then run through an in-house developed MATLAB thermal FE-analysis axisymmetrical solver with a built-in optimization routine based on the Inverse Heat Conduction Method. The objective function, eq 2.30, was in such a way that five temperature locations on the piston, see Figure 4, were compared to averaged temperatures given from a temperature measurement report of the piston. The measurement points across the top land for example were averaged as:

$$T_{Topland} = \frac{T_{D_1} + T_{D_2}}{2} \tag{4.1}$$

See Figure 5.2 for the locations of D_1 and D_2. The $T_{Topland}$ was considered as the average temperature across the top land of the piston and was one of the five variables in the objective function. The same procedure was done for the rest of the temperature measurement positions of the 2D axisymmetrical FE-model illustrated in Figure 4. The undercrown measurement points were not included in the 2D axisymmetrical FE-model due to the geometrical differences between the actual diesel piston and the axisymmetrical simplification.

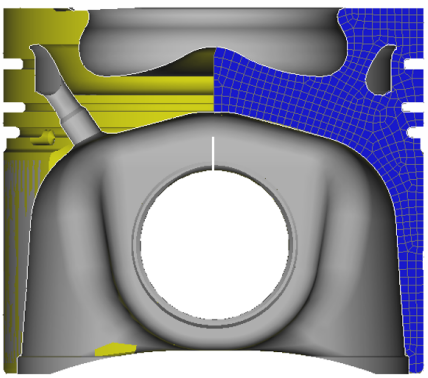

Figure 4.2: Four-node mesh of piston cross-section.

The optimizations routine did also take in to account the heat flux at each of the piston surfaces. The amount of heat flux at each surface was constrained according to the values found in [10] and shown in Table 2.1. The end result was a program that calibrated the initial boundary condition HTC until the objective function was minimized and the heat flux constrains were not violated. Three load cases were analyzed:

- 170 kW at 4000 RPM
- 135 kW at 3000 RPM
- 100 kW at 2000 RPM

The motivation for choosing these load cases is that they differ greatly in power output and engine speed. It was of interest to analyse how the thermal properties of the piston changes depending of the engine load in order to construct a complete thermal analysis piston model. Chapter 5 gives a detailed explanation of how this was done.

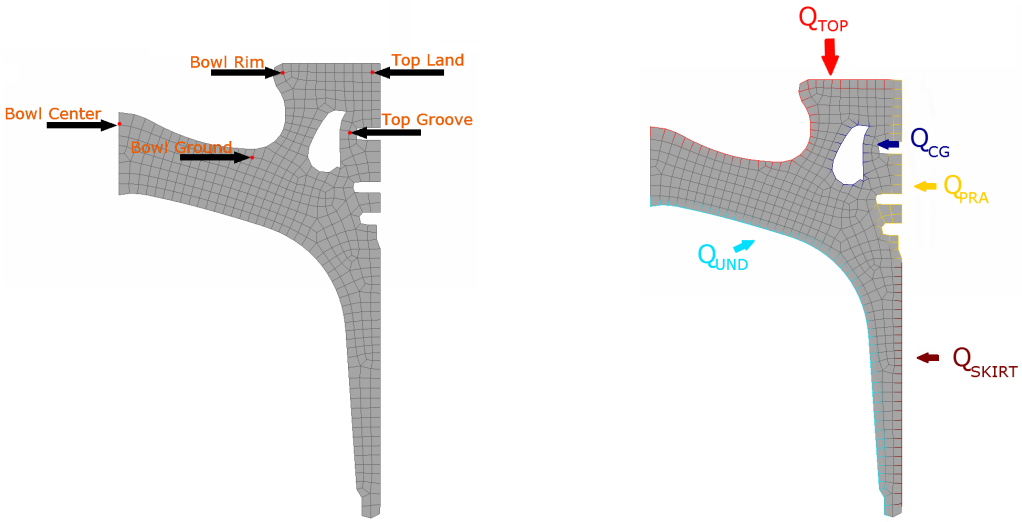

Figure 4.3: Temperature measurement positions & Heat transfer boundaries.

4.1 2D axisymmetrical piston FE-mesh

The 2D axisymmetrical FE-mesh was constructed in ANSA pre-processor software with first order quadratic shell elements. It was then exported to MATLAB for the in-house program to utilize the mesh information. A coarse mesh consisting of 430 elements was used in order to perform quick and time efficient FE-analyses with the HTCs parameter calibration routine. A 3D visualisation of the simplified 2D axisymmetrical FE-model can be seen in the Figure 4.4.

Figure 4.4: 3D illustration of the 2D axisymmetrical FE-mesh of the piston.

4.2 2D axisymmetrical initial boundary condition

The initial boundary condition HTCs for the 2D axisymmetrical diesel piston were determined with either analytical methods, empirical correlations, numerical analysis or assumptions based on the theory from the literature study explained in chapter 2. Each of the following sections will explain how the boundary conditions were calculated for the given load cases.

4.2.1 2D thermal load from gas combustion

As explained in section 2.3, heat transfer from the combustion can be determined by empirical methods or in numerical CFD analysis. Thermal analyses conducted with empirical calculations yielded imprecise result. Either the expression of the HTCs of the piston top had strange characteristics such that it was unphysical or the piston structure temperature field was diverging too much from the measured data. The cause of this can be explained by either that the empirical methods are not suitable for this type of piston and load case or that the developed optimization program was not robust enough. Another approach for modelling the HTCs at the piston top was conducted. CFD-data from a previous thermal analysis of the maximum load case, i.e. 170 kW at 4000 RPM, was available at Volvo Cars. The CFD-data contained high resolution spatial data for both the piston gas surface temperature and HTC of the piston top. The spatial HTC and piston surface gas temperature distributions for the piston top geometry from CFD-simulations are presented in Figure 4.5 and 4.6. This data was then manipulated with the use of the MATLAB surface fitting subroutine *fit.m* such that two cubic polynomial surface expressions for the HTC and piston surface gas temperature distribution, $h_{Top}(r,z)$ and $T_{gas}(r,z)$ respectively, were derived with respect to the piston radius, r, and the piston bowl height, z.

$$h_{Top}(r,z) = p_1 + p_2 r + p_3 z + p_4 r^2 + p_5 rz + p_6 z^2 + p_7 r^3 + p_8 r^2 z + p_9 r z^2 + p_{10} z^3 \tag{4.2}$$

$$T_{gas}(r,z) = p_{t1} + p_{t2} r + p_{t3} z + p_{t4} r^2 + p_{t5} rz + p_{t6} z^2 + p_{t7} r^3 + p_{t8} r^2 z + p_{t9} r z^2 + p_{t10} r^3 \tag{4.3}$$

The CFD-data was further adjusted with respect to results from GT-Power simulations. $T_{gas}(r,z)$ and h_{Top}(r,z) expressions were offset according to the time averaged HTC and gas temperature that the GT-power simulation calculated in such a way that:

$$mean(T_{gas}(r,z)) = T_{GT_{Power}} \tag{4.4}$$

$$mean(h_{Top}(r,z)) = h_{GT_{Power}} \tag{4.5}$$

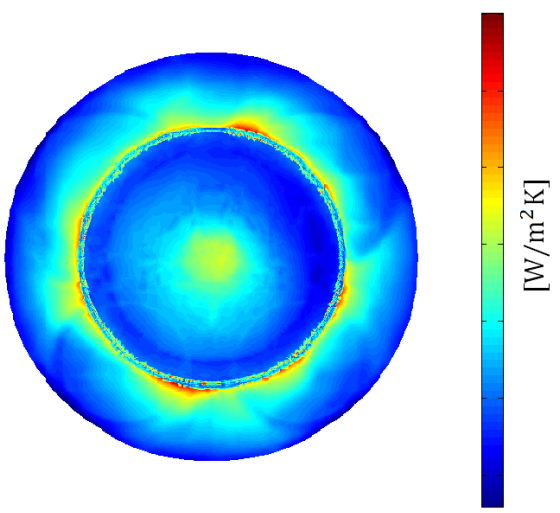

Figure 4.5: HTC distribution from CFD-simulations.

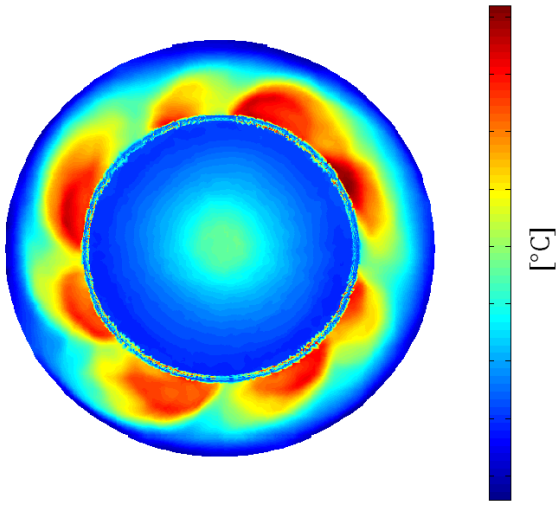

Figure 4.6: Temperature distribution from CFD-simulations.

4.2.2 2D heat transfer coefficients in the piston ring assembly and piston skirt

An important aspect of the thermal analysis of the diesel piston and cylinder liner interaction is the heat transfer modelling of the piston rings. The piston rings are the outermost part of the piston and have the closest contact with the cylinder liner.

A common heat transfer modelling technique of the piston ring assembly is the thermal circuit method [16]. The thermal circuit method is an analogy to the electrical circuit and uses thermal resistance for calculation of heat transfer through multiple instances. Heat flow passages are illustrated in Figure 4.7. Due to the small clearances, it is assumed in [16] that the convective heat transfer in negligible.

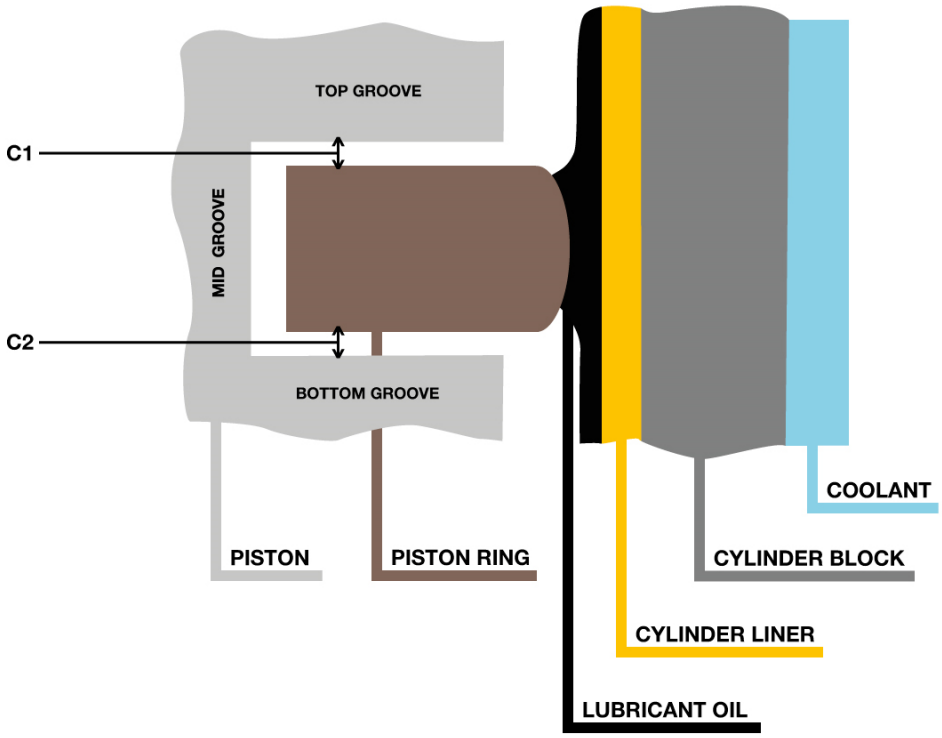

Figure 4.7: Illustration of piston ring Assembly and cylinder liner.

The thermal resistances, R, for the clearance between the piston and the piston rings were defined in [13] and are stated in eq 4.6.

$$R = \frac{L}{kA} \tag{4.6}$$

Here L is the heat transfer length, k is the thermal conductivity of the material, and A is the area of the heat transfer surface.

For the cylindrical shaped heat flow passages, i.e. the outer piston ring geometry, the lubricant oil film, the ring land and the cylinder wall, the resistance was calculated as shown in eq 4.7 [13]. Here the inner and outer radii of the heat flow passage are denoted r_1 and r_2 respectively.

$$R_c = \frac{ln(\frac{r2}{r1})}{2\pi Lk} \tag{4.7}$$

The coolant flow on the outside of the cylinder was a given thermal load with known heat transfer coefficient, h and a known coolant temperature. This resistance was calculated as stated in eq 4.8 [13].

$$R_h = \frac{1}{hA} \tag{4.8}$$

For calculating each of the thermal resistances with the thermal circuit method, the clearances between each of the components as well as the thermal conductivity for the lubricant oil, piston ring, cylinder liner and cylinder block materials were determined.

As a result of the clearance between the ring groove and the piston ring, the contact face of the piston ring and the piston will change during the four stroke engine cycle. In [16] it is assumed that three quarters of cycle time, the piston rings are in contact with the bottom groove surface while the remaining quarter the piston rings rest on the top surface. As such, an averaged resistance R-value for the top and bottom grooves were calculated as:

$$R_{TG} = 0.75R_{C_1} + 0.25R_{C_2} \tag{4.9}$$

$$R_{BG} = 0.25R_{C_1} + 0.75R_{C_2} \tag{4.10}$$

Where R_{C_1} and R_{C_2} are equal to the thermal resistance for each of the clearance distances C_1 and C_2 which can be seen in Figure 4.7.

$$\begin{aligned} R_{C_1} &= \frac{C_1}{kA} \\ R_{C_2} &= \frac{C_2}{kA} \end{aligned} \tag{4.11}$$

The total resistance of each piston ring groove surface is determined by adding each resistance of the heat transfer path as shown in eq 4.12. The overall heat transfer coefficient for each piston ring is in turn determined from eq 4.13. The procedure of eq 4.12 and eq 4.13 was conducted for each piston ring.

$$R_{tot} = R_{C_{TG/BG}} + R_{Ring} + R_{Oil\ film} + R_{Liner} + R_{Block} + R_{Coolant} \tag{4.12}$$

$$h_{ring} = \frac{1}{R_{tot} A_{ring,groove}} \tag{4.13}$$

The heat transfer coefficient was applied to the ring grooves as a convective heat transfer load with ambient temperature set to the coolant temperature. The thermal circuit method was applied for the ring lands and the piston skirt as well. For these heat paths, the total resistance consisted of the resistance though the lubricant oil film, the cylinder liner, the cylinder block and the coolant flow. The total resistance for the skirt and the ring lands where expressed as shown in eq 4.14.

$$R_{tot} = R_{Oil\ film} + R_{Liner} + R_{Block} + R_{Coolant} \tag{4.14}$$

Piston ring dynamics

As described in section 2.6, the ring dynamics are affected by many different phenomena occurring during the engine working cycle. This thesis will not investigate the ring dynamics in any way as the scope of this thesis is more focused on a thermal analysis of the whole piston. Given the assumption in [16] that the bottom part of the piston ring groove is more often in contact with the piston ring, a ratio between the bottom part of the ring groove and top part of the ring groove was assumed. This ratio was calculated as follows:

$$Ratio = \frac{R_{tot_{top}}}{R_{tot_{bottom}}} \tag{4.15}$$

This ratio was a set value describing the heat transfer ratio between the upper and bottom ring groove and was not adjusted during further parts of the thermal analysis of the piston and can be considered as a simplified ring dynamics assumption.

4.2.3 2D heat transfer coefficient of the cooling gallery

As the authors of this thesis did not have any previous experience with CFD simulations, the empirical correlation for determining the area-averaged heat transfer coefficient in the oil cooling gallery developed by Bush [6] was used to calculate the initial boundary condition HTC in the oil cooling gallery.

$$\begin{aligned} &\text{For} \quad P_r > 0.5 \qquad N_{Bush} = 0.495 R^{0.57} D_c^{0.24} P_r^{0.29} \\ &\text{For} \quad P_r << 1 \qquad N_{Bush} = 0.638 (RP_r)^{0.5} D_c^{0.24} \end{aligned} \tag{4.16}$$

$$h_{CG} = kN_{Bush} \tag{4.17}$$

The oil temperature in the cooling gallery for the HTC was based on measured oil temperature for the load cases.

4.2.4 2D heat transfer coefficient of the piston undercrown

An assumption of turbulent flow in tubes based on Gnielinski's correlation [13] was utilized for the piston undercrown:

$$N_{uD} = \frac{(f/8)(Re - 1000)P_r}{1 + 12.7(f/8)^{1/2}(P_r^{2/3} - 1)} \tag{4.18}$$

Here N_{uD} is the Nusselt number, Re is the Reynolds number, P_r is Prandtl number and f is is the Darcy friction factor.

$$f = (0.79ln(Re) - 1.64)^{-2} \tag{4.19}$$

The heat transfer coefficient h_{und} for the undercrown is thus:

$$h_{und} = kN_{uD} \tag{4.20}$$

This initial assumption is a rough estimate of the actual heat transfer properties of the undercrown.

4.2.5 Applying the convective boundary condition in 2D axisymmetrical FEA

The thermal boundary loads were mixed/convective boundary conditions. This type of load was described in subsection 2.9.2 and considers the convective heat flow from a ambient temperature through a film with a corresponding heat transfer coefficient to the piston surfaces. For example, the load assembly of the piston top surface elements can be seen in eq 4.21, where L^e denotes the element surface length and $\bar{r}^e$ is the element surface average location along the piston radius.

$$\begin{aligned} \boldsymbol{K}^e_{c,Top} &= h^e_{Top} \bar{r}^e L^e \begin{bmatrix} \frac{1}{3} & \frac{1}{6} \\ \frac{1}{6} & \frac{1}{3} \end{bmatrix} \\ \boldsymbol{f}^e_{c,Top} &= h^e_{Top} T_{gas} \bar{r}^e L^e \begin{bmatrix} \frac{1}{2} \\ \frac{1}{2} \end{bmatrix} \end{aligned} \tag{4.21}$$

The average radius of the elements in the 2D axisymmetrical FE-mesh were obtained by integration of the radius of the elements as shown in eq 4.22.

$$\bar{r}^e = \int_L r^e dL \approx \frac{r^e_{x,2} + r^e_{x,1}}{2} \tag{4.22}$$

Here $r^e_{x,2}$ and $r^e_{x,1}$ are the outer and inter radius of the elements nodes respectively.

The element stiffness (conductivity) matrix, $\boldsymbol{K}^e_c$ was constructed with respect to convective loads on the piston undercrown, oil cooling gallery, ring assembly and skirt. The convective boundary conditions were applied in the same way as shown in eq 4.21, but with different HTCs and different ambient temperatures. The ambient temperatures were obtained by GT-Power simulations and from measurements or qualified assumptions.

4.2.6 Calibration of heat transfer coefficients for the 2D axisymmetrical FE-model

With the initial boundary conditions HTCs determined, the in-house developed MATLAB thermal FE-analysis parameter calibration program was used for determining the HTCs of the 2D axisymmetrical model. For the HTCs of the piston ring assembly and the oil cooling gallery, the distribution was assumed to be even for the corresponding surfaces, hence these HTC-values were calibrated as scalars and no polynomial curve fitting or polynomial coefficient-calibration was necessary. The piston top load function $h_{Top}(r, z)$ in eq 4.2 was calibrated by changing the amplitude and offset of the function. The undercrown was calibrated by grouping several elements into having the same HTC and constructing a final function with respect to the undercrown radius $h_{und}(r)$ as a first degree exponential equation with curve fitting.

$$h_{und}(r) = Ae^{Br} \tag{4.23}$$

See Figure 4.8 for an illustration of the undercrown HTC curve fitting.

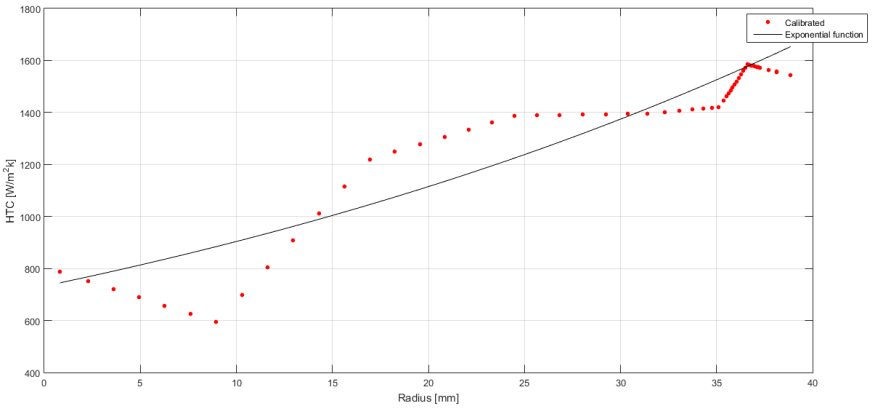

Figure 4.8: Undercrown HTC curve fitting.

Each of the HTCs were constrained by set boundaries in order to have physical properties. When the objective function was minimized and the heat flux constraints were achieved, the solution was determined as feasible.

For adjustment of the piston HTCs, an optimization algorithm was used according to the Inverse Heat Conduction Method. For the 2D axisymmetrical parameter calibration conducted in the in-house MATLAB code, the MATLAB subroutine *fminsearchbnd.m* was used. *fminsearchbnd.m* is a routine similar to *fminsearch.m* which uses the Nelder-Mead simplex algorithm to find minimum of the objective function [19], but it differs in the sense that *fminsearchbnd.m* allows variable bound constraints. The optimization algorithm changes the value of the piston boundary HTCs iteratively according the Nelder-Mead simplex algorithm until the value of the objective function converges to a set tolerance.

For the heat flux output of the piston to correlate to the numbers presented in Table 2.1, the optimization routine *fmincon.m* was used. *fmincon.m* is an optimization routine which takes boundary constraints into consideration while minimizing an objective function. This routine ensured minimized temperature difference between the measured and calculated piston temperatures while the heat flux input and output was regulated.

The calibration procedure for the piston HTCs was based on the work of Xiqun Lu et. al. [17], [11] and is schematically shown in Figure 2.18.

As shown Figure 2.18, initial HTC values were set and the Finite Element heat transfer analysis was conducted for this set of HTCs. An error residual was determined as the difference between the measured temperature and the calculated nodal temperature obtained from the FE-analysis as seen in eq 2.28. The root mean square of this residual is then defined as the objective function to be minimized by optimization of the piston HTCs, see eq 2.30. If the solution violated the heat flux constraints, the algorithm regarded that solution as unfeasible and chose the solution which had the lowest objective function while still satisfying the constraints.

4.3 Results from 2D axisymmetrical parameter calibration

Results from the 2D axisymmetrical parameter calibration with the developed MATLAB program are presented in this section. The results were extracted for the engine load case 170 kW at 4000 RPM. The remaining load cases, 135 kW at 3000 RPM and 100 kW at 2000 RPM, can be found in Appendix A.1.

The temperature field of the 2D axisymmetrical piston structure at the given load case is presented in Figure 4.9. The adjacent Figure 4.10 displays the reference temperature difference in the measurement points used in the 2D axisymmetrical parameter calibration.

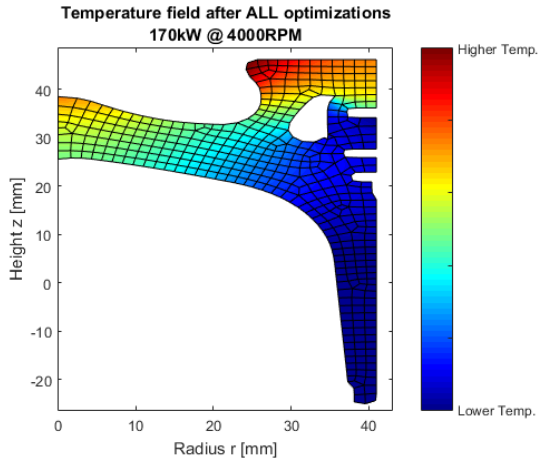

Figure 4.9: 2D axisymmetrical temperature field.

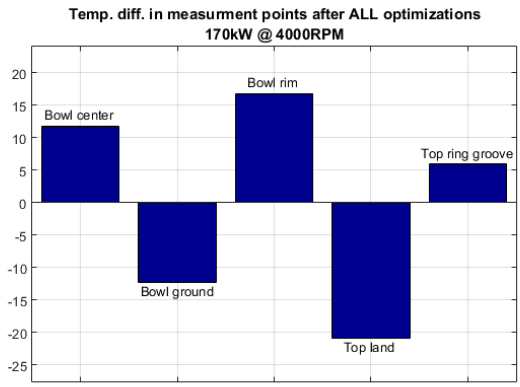

Figure 4.10: Temperature difference between calculated and measured temperatures.

The heat flux distribution over the piston surfaces can be seen in Figure 4.11. Each of the sections of the pie chart represent a piston boundary in the 2D axisymmetrical FE-model and its total and percentual boundary heat flux.

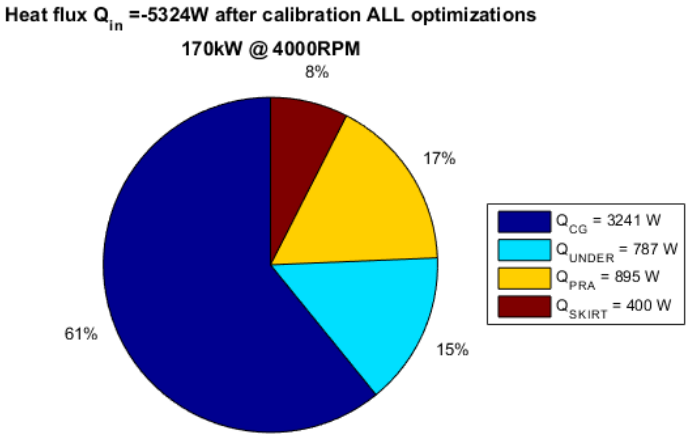

Figure 4.11: Boundary heat flux distribution.

As output of the 2D axisymmetrical parameter calibration, the calibrated piston boundary HTCs were obtained. Presented in Figure 4.12 are the the calibrated values of the piston ring assembly, skirt and cooling gallery HTC values can be found for the specified load case. The radial- and height wise HTC- and temperature distribution from combustion on the piston top surface is shown in Figure 4.13 and Figure 4.14, while the radial undercrown HTC distribution is presented in Figure 4.15.

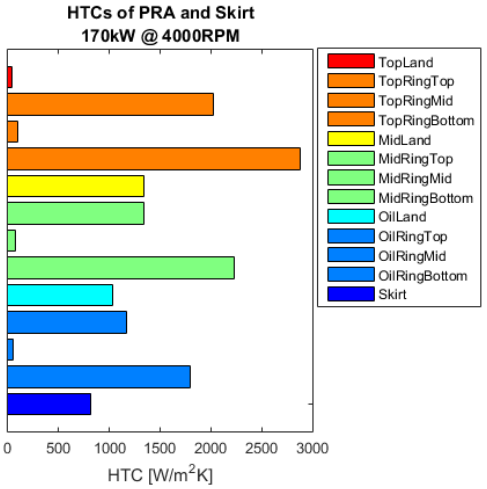

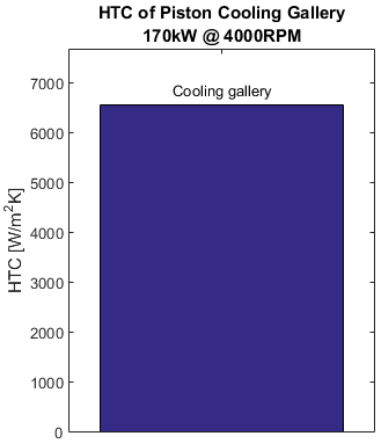

Figure 4.12: Calibrated values of the HTCs in the piston ring assembly, skirt and cooling gallery.

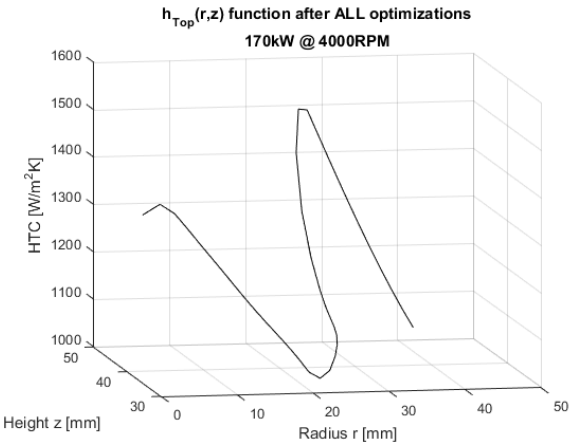

Figure 4.13: Piston top surface HTC distribution.

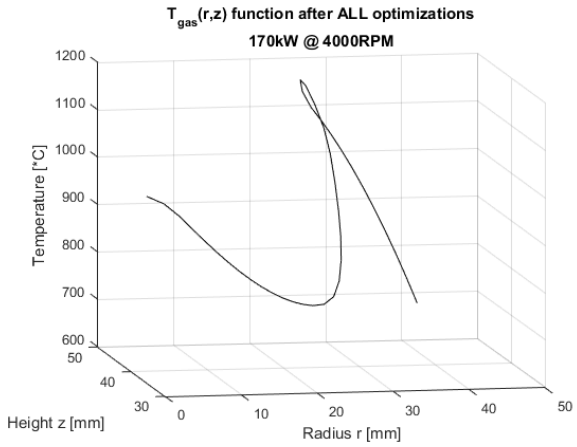

Figure 4.14: Piston top surface temperature distribution.

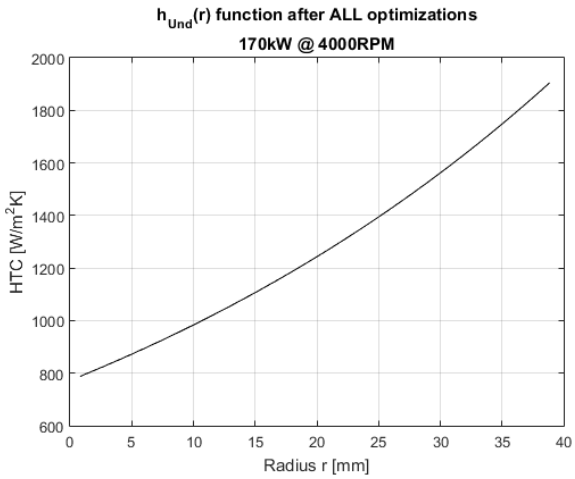

Figure 4.15: Piston undercrown HTC distribution.

5 3D thermal analysis

The next phase of the thermal piston analysis was to perform a thermal analysis for the complete 3D piston model. Figure 5.1 shows the step in the solution strategy.

With the same approach as with the 2D axisymmetrical model, a parameter calibration of the HTCs by optimization was necessary to be performed with respect to heat fluxes on the surfaces and measured temperature data. The temperature measurement points are shown in Figures 5.2 and 5.3.

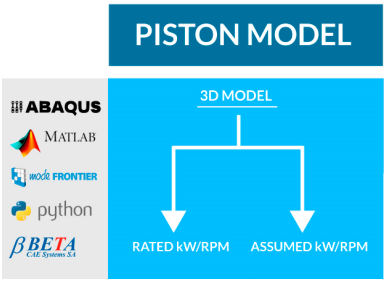

Figure 5.1: Solution strategy: 3D model.

The calibrated HTCs from the 2D axisymmetrical model were used as initial values for the surface boundaries of the 3D piston FE-model. The 3D piston FE-model is a true geometrical representation of the piston of interest, see Figure 5.4. Compared to the 2D axisymmetrical model, the geometry of the piston changes along the circumference of the piston. The 3D piston FE-model was therefore divided into sections for the analysis to be of higher spatial resolution in order to give a more accurate representation of the true thermal behaviour of the piston. This is explained in detail in subsection 5.3.

Two different 3D thermal analysis models were constructed. One of the models used the cubic polynomial expressions, $h_{Top}(r, z)$ and $T_{gas}(r, z)$, obtained from the 2D axisymmetrical parameter calibration while the second model used mapped CFD-data as the piston top load. The top load modelling approaches are further explained in subsection 5.2. This was done in order to analyse which method yielded better results in terms of temperature correspondence to measurement data. The remaining surfaces (PRA, CG, skirt etc.) were modelled equally for the two models.

With the 3D based parameter calibration through optimization done for different load cases, a linear HTC interpolation based piston model was constructed which in turn was regarded as a complete thermal analysis piston model. This is thoroughly explained in section 6.

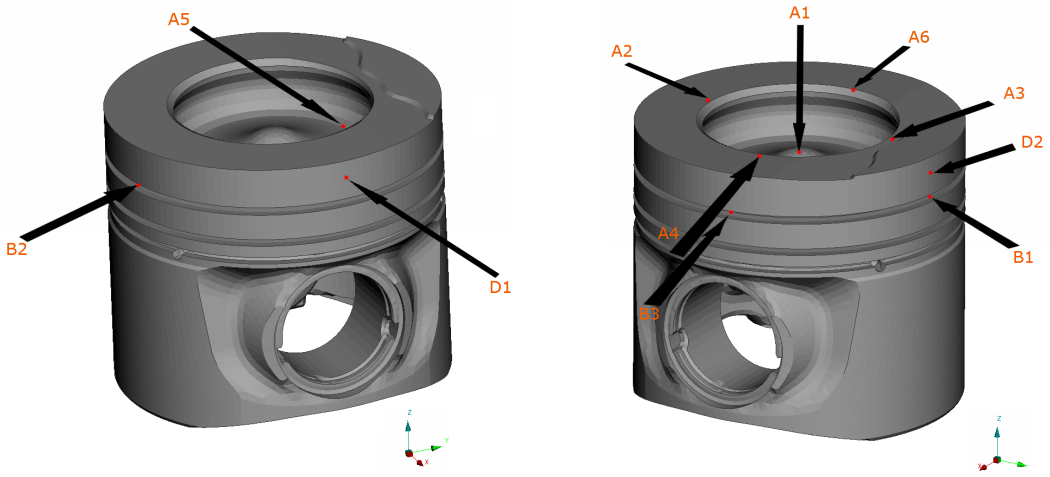

Figure 5.2: Measurement points.

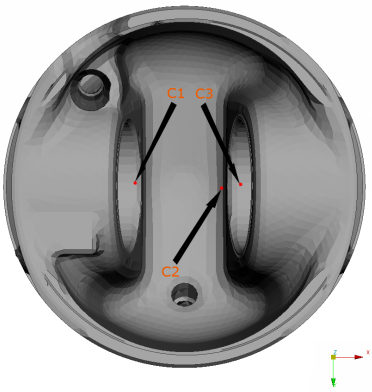

Figure 5.3: Measurement points.

5.1 3D piston FE-model

The 3D piston FE-model was constructed in the ANSA pre-processor software with second order tetrahedral heat transfer elements DC3D10. A fine mesh consisting of 148149 elements was used in order to obtain a high resolution of the temperature field in the piston. The 3D FE-model can be seen in the Figure 5.4.

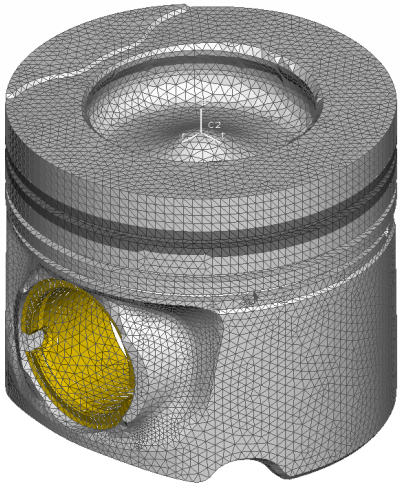

Figure 5.4: 3D FE-model of the piston.

5.2 3D thermal load from gas combustion

Two approaches of modelling the top thermal load on the piston were performed with the 3D model; polynomial expression and CFD-mapping. The two approaches will be explained in detail in the following subsections.

5.2.1 Polynomial expression

From the 2D axisymmetrical parameter calibrated model, two cubic polynomial curves describing the piston top HTC and temperature distribution, $h_{Top}(r, z)$ and $T_{gas}(r, z)$, were obtained. These curves do not change across the circumferential direction as the 2D axisymmetric model is incapable of having such a property. Further modification of the polynomial curves were done in which the magnitude of the HTC and temperature would vary in the circumferential direction. This is essential in order to properly capture how the combustion occurs on the piston top surface.

A sinusoidal variation of the HTC and temperature was assumed. The sinusoidal variation parameter was constructed in such a way that it would align with the combustion propagation. The final result was an expression for both the HTC and temperature as $h_{Top}(r, z, \phi)$ and $T_{gas}(r, z, \phi)$ seen in eq 5.1 and eq 5.2 respectively, with ϕ being the angle position on the piston top surface relative the anti-thrust side (see figure 5.5.

$$h_{Top}(r, z, \phi) = (p_1 + p_2 r + p_3 z + p_4 r^2 + p_5 rz + p_6 y^2 + p_7 r^3 + p_8 r^2 z + p_9 r z^2 + \\ + p_{10} z^3)(abs(sin(4\phi))0.16 + 1) \tag{5.1}$$

$$T_{gas}(r, z, \phi) = (p_{t1} + p_{t2} r + p_{t3} z + p_{t4} r^2 + p_{t5} rz + p_{t6} z^2 + p_{t7} r^3 + p_{t8} r^2 z + p_{t9} r z^2 + \\ + p_{t10} z^3)(abs(sin(4\phi))0.2748 + 1) \tag{5.2}$$

5.2.2 CFD-simulation mapping

Time-averaged CFD-data from a previous thermal analysis done by Volvo Cars was available for the maximum engine load case, i.e. 170 kW at 4000 RPM. The load data from a CFD-simulation was mapped onto the top surface of the piston as a convective thermal load. This gave a detailed spatial HTC and temperature distribution on the top surface capturing the injection points and variations across the top surface.

5.3 3D heat transfer coefficients in the PRA and remaining piston surfaces

The initial convection load terms for the 3D model piston ring assembly and outer surfaces where taken from the calibrated values of the 2D axisymmetrical model. As with the top load, no variation in the circumferential-direction was able to be captured with the 2D axisymmetrical model.

The 3D FE-model was split into three regions, anti-thrust-, thrust-, face/rear-side ($ATS, TS, FS/RS$), see Figure 5.5. This was done in order to capture the variation of the heat transfer properties across the piston. The top land, top groove, mid land and mid groove were split into these three regions. The two grooves were then divided into top, bottom and mid parts as in the 2D axisymmetrical model. The oil groove and oil land were kept as separate single entities, with no circumferetnial region splitting. However, the oil groove was modelled as the other ring grooves, i.e. in top-,mid- and bottom surfaces. See Figure 4.7 for clarification of the piston groove setup.

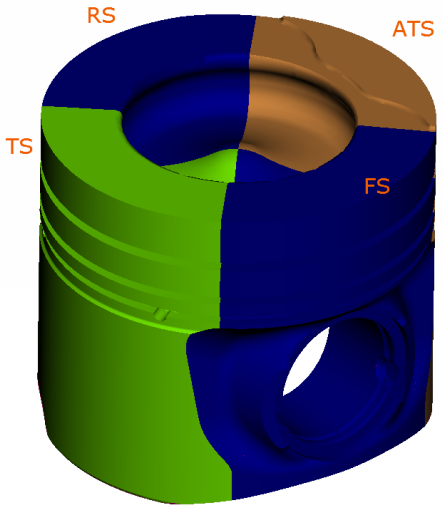

Figure 5.5: Piston region split.

As with the 2D axisymmetrical model, the ratio between the top and bottom groove HTCs were kept constant to represent the ring dynamics, as explained in subsection 4.2.2. The piston skirts were split into ATS and TS parts.

The complete 3D model of the piston has surfaces (Pin Face and Pin Boss) which were not able to be modelled in the 2D axisymmetrical model. The two pin face surfaces of the piston were therefore not calibrated by the 2D axisymmetrical model. For the 3D parameter calibration the pin faces were kept as a single surface with the same assumed initial HTC value of 1000 W/m^2K and an ambient temperature corresponding to the coolant. Similarly, the pin boss was assumed to have a initial value of 1000 W/m^2K and an assumed ambient temperature of 150$°C$.

5.4 3D heat transfer coefficient of the cooling gallery

The cooling gallery was split into inlet, outlet and channel sections in order to capture the behaviour of the flow of the cooling oil within the piston body. The cooling gallery sections are illustrated in Figure 2.3.

5.4.1 Inlet and outlet

As the oil enters the cooling gallery through the oil inlet, it absorbs the heat of the piston body generated by the engine work cycle. The oil is then ejected through the oil outlet. This in turn means that the cooling oil has a lower temperature at the inlet than at the outlet. The thermal loads for the inlet and outlet were therefore modelled to capture this phenomenon. The initial HTC values for the oil inlet and oil outlet were taken from the calibrated 2D axisymmetrical model and the temperatures were set to the measured inlet and outlet oil temperature respectively.

5.4.2 Channel

The cooling gallery channel is split in to two separate parts and exits at the same outlet. As explained above, the oil gradually heats up as it flows through the channel. An assumed linearly increasing temperature of the oil from the inlet to the outlet was modelled. As the two channels connects at the outlet, the mean temperature at the end of the channels corresponded to the measured oil outlet temperature. The HTC for the two channel parts was set to be equal and was based on the calibrated 2D axisymmetrical model. Figure 5.6 clarifies the described temperature modelling.

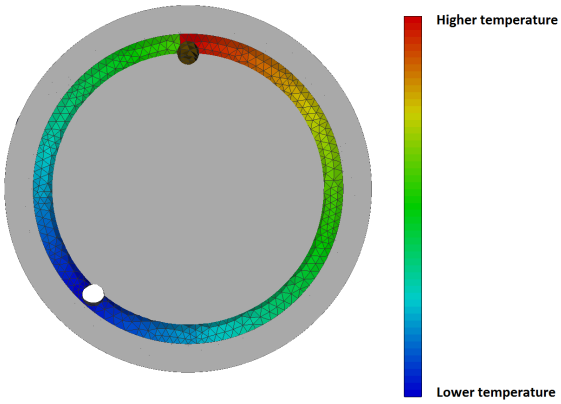

Figure 5.6: Oil temperature variation in the oil cooling gallery.

5.5 3D heat transfer coefficient of the piston undercrown

The thermal load on the undercrown of the piston is based on the first order exponential curve fitting function derived from the calibrated 2D axisymmetrical model. The load has a HTC function which varies across the radius of the undercrown as $h_{und}(r)$ and a temperature which represents the oil and air mist.

$$h_{und}(r) = Ae^{Br} \tag{5.3}$$

See Figure 4.8 for an illustration of the undercrown HTC curve fitting.

5.6 Calibration of heat transfer coefficients in 3D FE-model

Similarly to the 2D axisymmetrical model, a parameter calibration of the HTCs of the 3D model was performed with the principle of the Inverse Heat Conduction Method. The 3D parameter calibration was more complex compared to the 2D axisymmetrical model as it had a higher number of HTCs values to calibrate, an objective function which had greater number of variables and more heat flux constraints, all of which were needed to be taken into account for a feasible solution. The calibration was done through the use of the optimization software modeFrontier. The optimization routine was performed with the Nelder-Mead simplex algorithm. A root-mean-square objective function consisting of 14 different nodal temperature values was to be minimized with respect to the measurement data. See Figures 5.2 and 5.3 for an illustration of the nodal locations. A total number of 13 heat flux constraints were setup based on the heat flux proportion guidelines given by Mahle, see Table 2.1.

The 3D FE-model consisting of the sinusoidal cubic polynomial HTC expression for the piston top load could adjust its amplitude, offset, sinusoidal amplitude and sinusoidal offset. The mapped 3D-model with the mapped CFD-data could vary the amplitude and offset of the HTCs. The exponential function of the undercrown could vary the amplitude and offset of the HTCs. The remaining HTCs of the piston surfaces were treated as scalars and could vary in magnitude within a 30% span of the calibrated HTC values from the 2D axisymmetrical model.

The modeFrontier optimization work-scheme for the two 3D FE-models consisted of:

- 25/23 Adjustable input variables (Polynomial/CFD)
- 1 Objective function (RMS of $\mathbf{r}_T$)
- 13 Heat flux constraints (Based on Mahle guidelines)
- 21 Output variables (Nodal temperatures and surface heat fluxes)

Abaqus was used as the FEM-solver for the 3D FE-models. The nodal temperature field, defined as NT11 in Abaqus, and heat fluxes for each surface, defined as SOH in Abaqus, were solved with the applied thermal loads described in previous sections. The results were then read by modeFrontier and the input variables were adjusted according to the Nelder-Mead simplex algorithm. The input variables were then re-applied after the adjustment and sent to Abaqus for a new simulation. This was done until the objective function reached convergence and a final feasible solution of the load case with respect to the temperature measurement data and heat flux constraints was determined.

5.7 Continuation of piston thermal analysis for different engine load cases

After a stable, consistent, repeatable and feasible solution methodology for the maximum engine load case of 170 kW at 4000 RPM was modelled, it was saved as a template. The template was then applied for 100 kW at 2000 RPM and 135 kW at 3000 RPM engine loads. As with the maximum engine load, the measured temperature data, heat flux based on GT-Power simulations and Mahle heat flux proportions were used as goal values. Each of the load cases went through the same procedure:

- Deriving initial HTC values based on analytical methods, empirical correlations, numerical analyses and qualified assumptions.
- A 2D axisymmetrical parameter calibration with the in-house developed MATLAB program.
- A 3D parameter calibration through modeFrontier and Abaqus.

5.8 Modelling the piston thermal behaviour for assumed engine load cases

As only three engine loads were run through the calibration procedure explained in previous sections, this gave a very narrow understanding of how the heat transfer changes with respect to engine speed and power output.

Thus, a ±10 kW variation of the rated power output for each of the calibrated engine speeds was also modelled. This was done for the purpose of calibrating HTCs for engine loads that are not rated.

The ±10 kW power output variation for 100 kW at 2000 RPM, 135 kW at 3000 RPM and 170 kW at 4000 RPM was modelled based on the assumption that the heat flux input from the combustion is proportional to the increase or decrease in power output.

For 170 kW at 4000 RPM this meant the following:

- At 4000 RPM the engine is rated at power output of 170 kW.
- The combustion heat flux absorbed by the piston top was calculated by GT-Power to be 5588 W at this specific load case.
- For 180 kW at 4000 RPM the heat flux would increase proportionally to the rated engine power output.

$$q_{in,180kW} = \left(\frac{180\,kW}{170\,kW}\right)5588\,W = 5916\,W \tag{5.4}$$

- The same procedure was done for 160 kW at 4000 RPM, i.e. the heat flux would decrease proportionally to the rated engine power output.

$$q_{in,160kW} = \left(\frac{160\,kW}{170\,kW}\right)5588\,W = 5259\,W \tag{5.5}$$

With these assumed heat flux values, a new HTC calibration routine model was setup. This model was done with the previous 3D FE-model of the piston and through the use of modeFrontier and Abaqus. The objective function to be minimized for the assumed load cases could not be based on measured temperatures as such were not available. Instead, the authors of this thesis set the objective function to be the minimization of the difference between the calculated piston top heat flux, $q_{in,calc}$ and the assumed proportionally varying heat flux explained previously. As an example, the objective function for the engine load 180 kW at 4000 RPM calibration is shown in eq 5.6:

$$f_{obj} = |q_{in,180kW} - q_{in,calc}| \tag{5.6}$$

The constraints for this new calibration model were also reset. As with the previously parameter calibrations, the heat flux distribution across the piston surfaces was set according to guidelines given by Mahle. However, additional constraints were set. For the load case of a higher engine output, i.e. 180 kW compared to the actual 170 kW at 4000 RPM, the calculated temperature points from the rated calibration point were assumed to be higher at every location.

$$\text{Temp.field}_{180\text{kW}} > \text{Temp.field}_{170\text{kW}} \tag{5.7}$$

Respectively, for 160 kW:

$$\text{Temp.field}_{160\text{kW}} < \text{Temp.field}_{170\text{kW}} \tag{5.8}$$

This meant that 14 additional constraints were added based on calculated temperatures form the calibrated models.

The initial HTC values for the 160 kW and 180 kW at 4000 RPM were both based on the calibrated HTC values at 170 kW at 4000 RPM with a ±10% span to vary within. The same modelling procedure was done for 135 kW ±10 kW at 3000 RPM and 100 kW ±10 kW at 2000 RPM.

5.9 Piston model with mapped CFD-data

The 3D parameter calibration with a top load consisting of a mapped CFD-load resulted in a slightly higher temperature residual than the 3D parameter calibration with the piston top load expressed as a sinusoidal cubic polynomial expression. Therefore the parameter calibration model with the piston top load expressed as a sinusoidal cubic polynomial expression was further developed. The results of the 3D parameter calibration with a top load consisting of a mapped CFD-film can be seen in Appendix A.4.

5.10 Results from 3D parameter calibration with rated engine loads

The results displayed in this section are extracted from a 3D parameter calibration described in subsection 5.6. As in section 4.3, only results from the load case 170 kW and 4000 RPM are presented. The remaining results from the rated engine loads are to be found in Appendix A.2.

The results are presented as contour plots of the piston structure temperature field, seen in Figure 5.7 to 5.9 with an isometric view, a top view and a cut view of the piston.

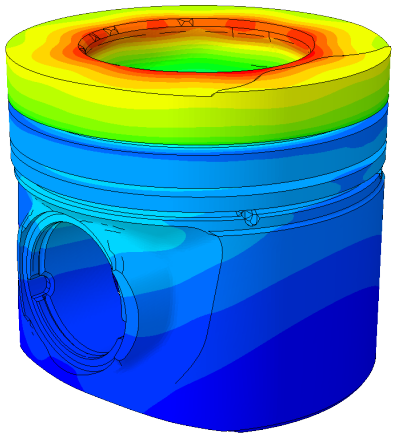

Figure 5.7: Isometric view of the piston temperature field for 170 kW at 4000 RPM.

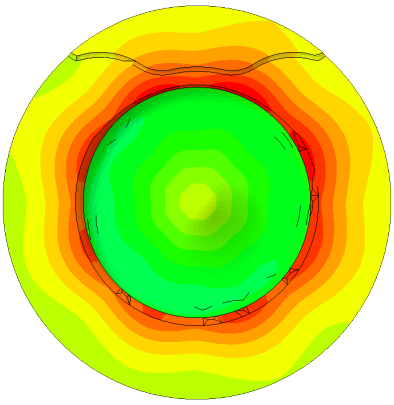

Figure 5.8: Top view of the piston temperature field for 170 kW at 4000 RPM.

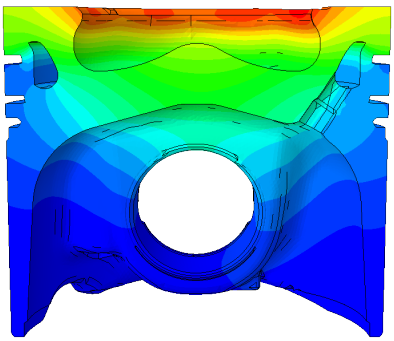

Figure 5.9: View of ATS-TS cut section of the piston temperature field for 170 kW at 4000 RPM.

Seen in Figure 5.10 are the reference temperature differences for the measurement points, as well as the RMS-error and the percentual heat flux distribution of the piston boundaries. These Figures are shown for all the rated load cases, i.e. 100 kW at 2000 RPM, 135 kW at 3000 RPM and 170 kW at 4000 RPM.

	100 kW | 2000 RPM	135 kW | 3000 RPM	170 kW | 4000 RPM
Reference temperature difference			
A1 Bowl Center :	2,8	3,9	8,7
A2 Bowl Rim TS :	4,1	-1,2	-0,5
A3 Bowl Rim ATS :	1,4	0,7	-1,3
A4 Bowl Rim FS :	8,4	12,6	19,0
A5 Bowl Ground ATS :	0,4	-3,3	-6,4
A6 Bowl Rim RS :	6,8	7,5	8,2
Piston Bowl mean error	3,98	3,4	4,6
B1 Groove 1 ATS :	7,8	9,2	10,8
B2 Groove 1 TS :	14,8	10,2	10,9
B3 Groove 1 FS :	-3,2	5,0	2,6
Piston Groove mean error	6,5	8,1	8,1
C1 Pin Boss RS :	0,5	0,9	-2,3
C2 Support FS :	-5,4	-2,2	-2,4
C3 Pin Boss FS :	2,4	-1,7	-0,7
Piston Pin Boss mean error	-0,8	-1,0	-1,8
D1 Top Land FS :	-19,8	-10,5	-9,2
D2 Top Land ATS :	-11,1	-11,5	-13,0
Piston Top Land mean error	-15,5	-11,0	-11,1
Reference temperature RMS error			
RMS error	8,4	7,11	9,78
Heat Flux			
Heat input [W]	3866	4891	5426
Cooling gallery output [%]	57,71%	59,93%	59,92%
PRA output [%]	22,01%	21,67%	21,54%
Undercrown output [%]	13,08%	7,95%	9,71%
Skirt output [%]	5,19%	7,27%	6,19%
Pin boss output [%]	1,04%	1,31%	0,27%
Pin face output [%]	0,86%	1,76%	2,28%

Figure 5.10: Reference temperature difference and piston boundary heat flux distribution.

5.11 Results from 3D parameter calibration with assumed engine loads

The results from the 3D parameter calibration for assumed engine loads, i.e. loads with no reference temperature data, are presented in this section. This calibration setup was described in subsection 5.8. Found below are the results from calibration for assumed load cases 160 kW at 4000 RPM and 180 kW at 4000 RPM. The remaining assumed load case result are presented in Appendix A.3.

Seen in Figures 5.11 to 5.13 are the contour plots of the piston structure temperature field shown after 3D parameter calibration for the assumed load case 160 kW at 4000 RPM. Similarly, the corresponding contour plots for the load case 180 kW at 4000 RPM are shown in Figures 5.14 to 5.16.

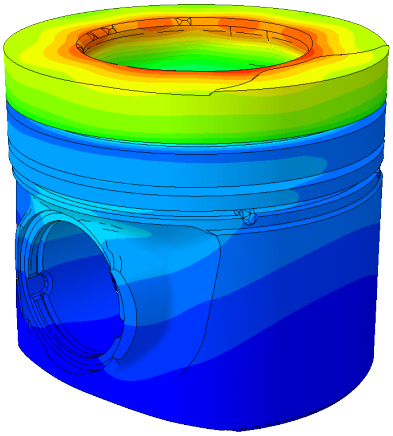

Figure 5.11: Isometric view of the piston temperature field for 160 kW at 4000 RPM.

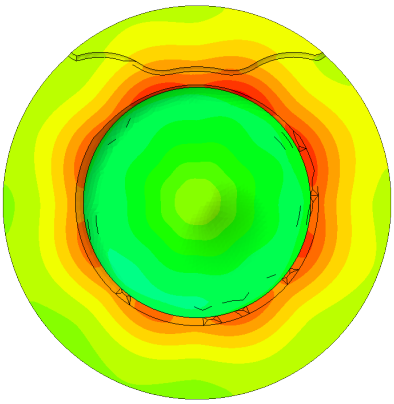

Figure 5.12: Top view of the piston temperature field for 160 kW at 4000 RPM.

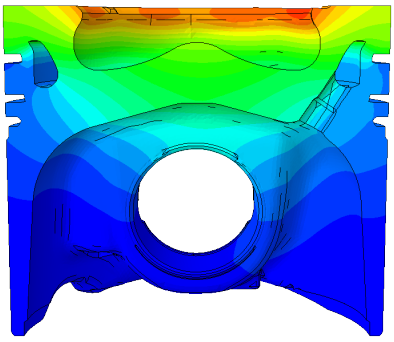

Figure 5.13: View of ATS-TS cut section of the piston temperature field for 160 kW at 4000 RPM.

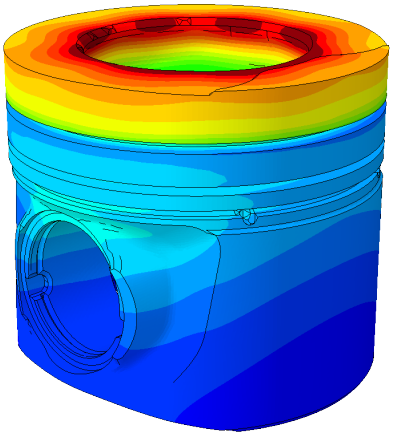

Figure 5.14: Isometric view of the piston temperature field for 180 kW at 4000 RPM.

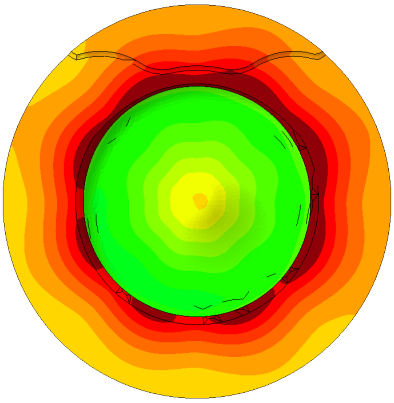

Figure 5.15: Top view of the piston temperature field for 180 kW at 4000 RPM.

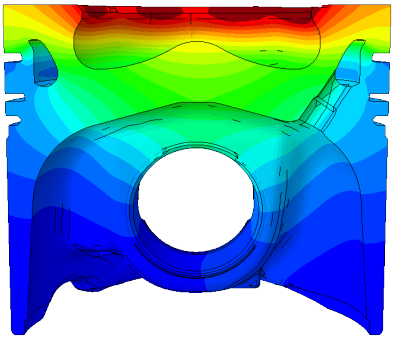

Figure 5.16: View of ATS-TS cut section of the piston temperature field for 180 kW at 4000 RPM.

The heat flux distribution over the piston boundaries for the respective load cases are presented in Figure 5.11

Heat Flux	160 kW | 4000 RPM
Heat input [W]	5237
Cooling gallery output [%]	59,14%
PRA output [%]	21,42%
Undercrown output [%]	10,81%
Skirt output [%]	6,07%
Pin boss output [%]	0,22%
Pin face output [%]	2,22%

Heat Flux	180 kW | 4000 RPM
Heat input [W]	5927
Cooling gallery output [%]	59,02%
PRA output [%]	22,07%
Undercrown output [%]	9,88%
Skirt output [%]	6,25%
Pin boss output [%]	0,37%
Pin face output [%]	2,35%

Figure 5.17: Piston surface heat flux distribution for load cases 160 kW at 4000 RPM and 180 kW at 4000 RPM.

5.12 Sensitivity analysis

A sensitivity analysis of the piston boundary load parameters was conducted in the sole purpose of getting an understanding of how the respective boundary load parameters affect the thermal analysis results and thus identifying the parameters with the highest sensitivity. The sensitivity analysis was performed by manually adjusting the calibrated parameter value by multiplying a factor and re-running the thermal FE-analysis with the new load parameter. The results in terms of the root-mean-square of the temperature differences and the piston surface heat flux distribution was then compared with the corresponding results of the original thermal analysis results.

5.13 Results from the sensitivity analysis

Figure 5.18 and Figure 5.19 display the results of the sensitivity analysis for the load case of 170 kW at 4000 RPM when varying certain parameter values. A comparison of the temperature difference RMS value and the piston surface heat flux distribution is shown respectively.

	170 kW | 4000 RPM		
Variable	factor	RMS	Diff
	1	9,78	
All grooves (HTC)	2	10,83	9,7%
Skirts (HTC)	2	9,70	-0,8%
Pin boss (HTC)	2	9,96	1,8%
Mid groove (HTC)	2	9,42	-3,8%
Oil groove (HTC)	2	9,69	-0,9%
Undercrown load (Amp)	1,5	10,15	3,6%
Top load (Amp)	1,5	32,54	69,9%
Cooling gallery (HTC)	2	25,38	61,5%
Top groove (HTC)	2	10,15	3,6%

Figure 5.18: RMS sensitivity analysis results for 170 kW at 4000 RPM.

170 kW | 4000 RPM		Q_IN		Q_CG		Q_UNDERCROWN		Q_PRA		Q_PIN_BOSS		Q_SKIRT		Q_PIN_FACE	
Variable	factor	Value	Diff	Value	Diff	Value	Diff	Value	Diff	Value	Diff	Value	Diff	Value	Diff
	1	-5426	-	3251	-	526,7	-	1169	-	14,7	-	335,9	-	123,6	-
All grooves (HTC)	2	-5551,2	2,3%	2988,5	-8,8%	472,5	-11,5%	1703,2	31,4%	10,5	-40,2%	309,2	-8,6%	113,081	-9,3%
Skirts (HTC)	2	-5439,1	0,2%	3209,6	-1,3%	440,1	-19,7%	1147,4	-1,9%	12,4	-18,1%	526,3	36,2%	119,287	-3,6%
Pin boss (HTC)	2	-5437,1	0,2%	3231,8	-0,6%	521,0	-1,1%	1158,2	-0,9%	25,7	42,8%	332,7	-1,0%	121,812	-1,5%
Mid groove (HTC)	2	-5455,3	0,5%	3159,1	-2,3%	498,2	-5,7%	1363,7	14,3%	12,4	-18,4%	322,1	-4,3%	118,025	-4,7%
Oil groove (HTC)	2	-5437,1	0,2%	3219,7	-1,0%	511,8	-2,9%	1249,0	6,4%	13,5	-8,5%	327,4	-2,6%	120,339	-2,7%
Undercrown load (Amp)	1,5	-5464,4	0,7%	3191,4	-1,9%	684,3	23,0%	1142,0	-2,4%	11,2	-31,5%	313,5	-7,1%	116,868	-5,8%
Top load (Amp)	1,5	-6414,8	15,4%	3886,1	16,3%	637,5	17,4%	1334,5	12,4%	22,4	34,5%	370,3	9,3%	138,011	10,4%
Cooling Gallery (HTC)	2	-6002,7	9,6%	4265,7	23,8%	417,0	-26,3%	920,7	-27,0%	6,2	-135,5%	294,1	-14,2%	106,138	-16,5%
Top groove (HTC)	2	-5514,9	1,6%	3095,5	-5,0%	511,3	-3,0%	1463,1	20,1%	13,6	-8,5%	329,2	-2,0%	121,075	-2,1%

Figure 5.19: Heat flux sensitivity analysis results for 170 kW at 4000 RPM.

6 Complete thermal analysis piston model

An in-house MATLAB program was developed which took into account the HTCs for each of the calibrated load cases (both rated and assumed engine loads) and interpolated linearly the HTCs between the calibrated loads for each piston boundary surface. By doing so, a linear variation of the HTCs with respect to engine speed and power output was assumed. Figure 6.1 shows the step in the solution strategy.

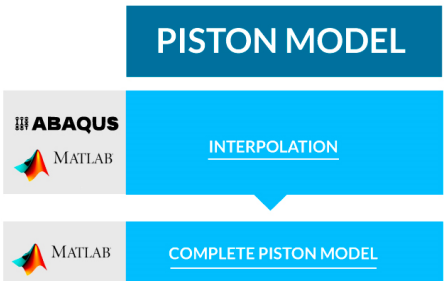

Figure 6.1: Solution strategy: Interpolation & Complete piston model.

With the variation of power output, engine speed and the assumed linear variation of the HTCs between the stated load cases it was possible to formulate matrices of kW and RPM, $\mathbf{h}(kW, RPM)$, for each boundary of the 3D FE-model. The MATLAB program would interpolate the HTCs based on all the calibrated load cases and extract the HTCs for a selected engine load with a range of 90 to 180 kW and 2000 to 4000 RPM. A total of 357 different engine power output and speed combinations were derived from the initial nine calibrated load cases. As such, a complete thermal analysis piston model was constructed.

6.1 Results from interpolation of heat transfer coefficients

Figure 6.2 displays the calculated $\boldsymbol{h}_{CG}(RPM, kW)$ matrix through the in-house developed MATLAB program based on the linear interpolated modelling technique for the cooling gallery. See Appendix A.5 for $\boldsymbol{h}(RPM, kW)$ illustrations for every surface of the piston.

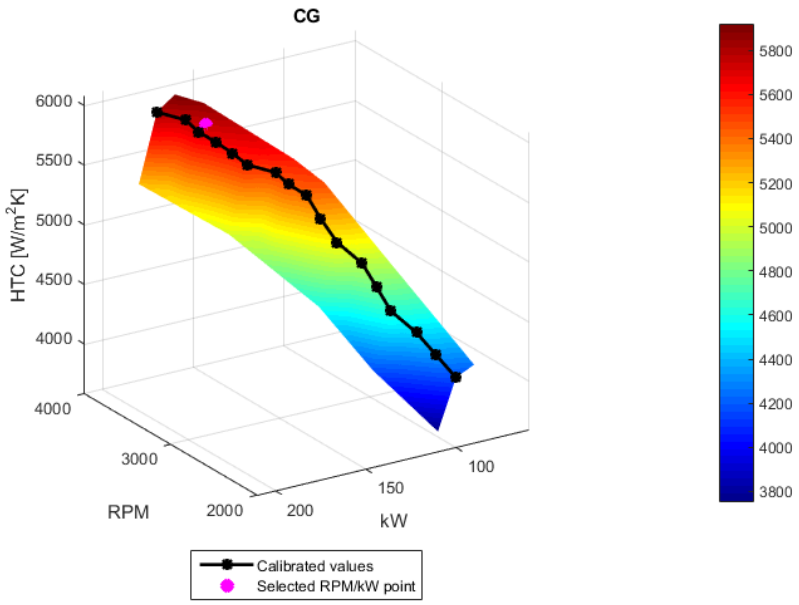

Figure 6.2: $\boldsymbol{h}_{CG}(RPM, kW)$

6.2 Validation of the complete thermal analysis piston model

The complete thermal analysis piston model was validated by extracting piston boundary HTCs from the interpolating MATLAB program for a set of engine power outputs and speeds combinations. The HTCs at engine speeds of 2500 RPM and 3500 RPM with corresponding engine power output of 122 kW and 152 kW were extracted and a thermal analysis of the piston was executed with the extracted set of boundary HTCs. These load cases were rated engine loads. As such, temperature measurement data existed for these validation loads. This enabled temperature comparisons of the thermal analysis simulations to the temperature measurement data. Additionally, the heat flux distribution over the piston boundaries was compared.

Validation of the assumed engine power outputs of the complete thermal analysis piston model was conducted. As measured temperature data did not exist for the assumed engine power outputs, temperature comparisons were not able to be performed. The validation methods of choice were the heat flux distribution over the piston boundaries based on Mahle guidelines and visual affirmation of the piston structure temperature field so that it resembled the known characteristics of a piston structure temperature field.

The complete thermal analysis piston model was validated for following engine load cases:

- Rated engine load cases:
  - 122 kW at 2500 RPM
  - 152 kW at 3500 RPM
- Assumed load cases:
  - 117 kW at 2250 RPM
  - 153 kW at 3375 RPM

6.3 Results from validation of the thermal analysis piston model

In this section the results from the thermal analysis piston model validation are presented. The validation methods are described in subsection 6.2. Subsection 6.3.1 treats the results of the thermal analysis piston model validation for rated loads, while subsection 6.3.2 displays the validation results for assumed engine load cases.

6.3.1 Validation results for rated load cases

The results are presented as contour plots of the piston structure temperature field, as the piston surface heat flux distribution and as temperature difference in measurement points. The validation was conducted at engine speeds of 2500 RPM and 3500 RPM with the engine power output 122 kW and 152 kW respectively.

The piston structure temperature field is shown as contour plots for the load case 122 kW at 2500 RPM in Figures 6.3 to 6.5, while the corresponding contour plots for the load case 152 kW at 3500 RPM are shown in Figures 6.6 to 6.8.

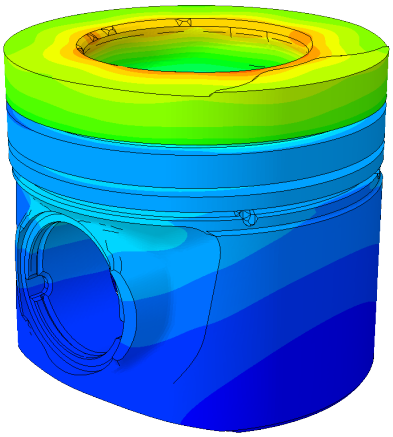

Figure 6.3: Isometric view of the piston temperature field for 122 kW at 2500 RPM.

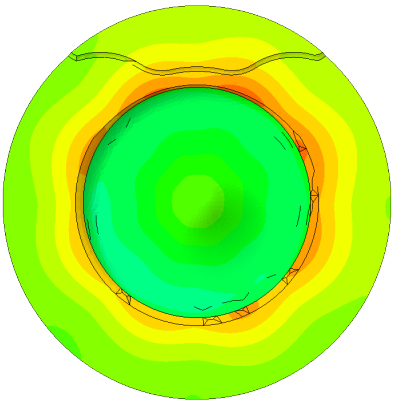

Figure 6.4: Top view of the piston temperature field for 122 kW at 2500 RPM.

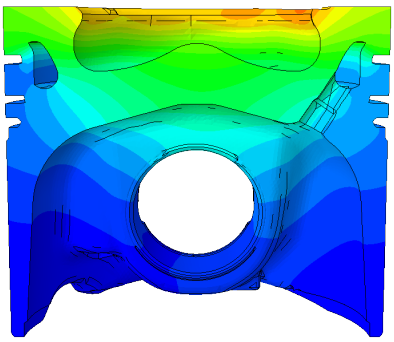

Figure 6.5: View of ATS-TS cut section of the piston temperature field for 122 kW at 2500 RPM.

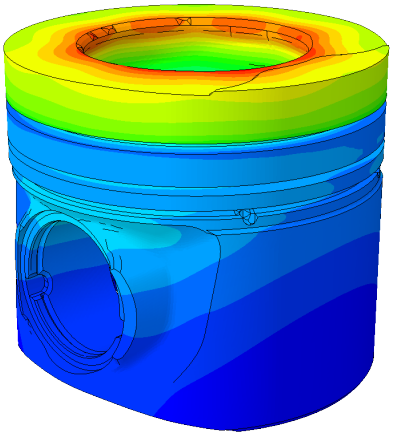

Figure 6.6: Isometric view of the piston temperature field for 152 kW at 3500 RPM.

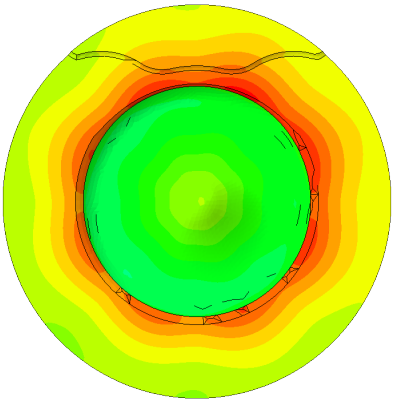

Figure 6.7: Top view of the piston temperature field for 152 kW at 3500 RPM.

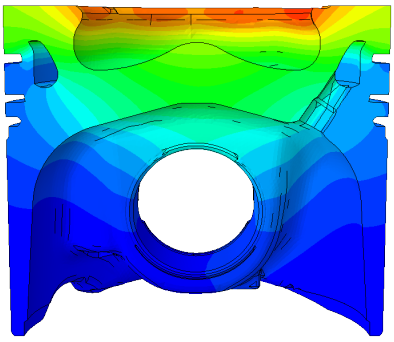

Figure 6.8: View of ATS-TS cut section of the piston temperature field for 152 kW at 3500 RPM.

Figure 6.9 presents the reference temperature differences in measurement points as well as the RMS-error and the percentual heat flux distribution of the piston boundaries.

	122 kW | 2500 RPM	152 kW | 3500 RPM
Reference temperature difference		
A1 Bowl Center :	1,7	4,5
A2 Bowl Rim TS :	-1,6	8,3
A3 Bowl Rim ATS :	-4,1	-3,0
A4 Bowl Rim FS :	8,1	11,9
A5 Bowl Ground ATS :	-5,6	-1,4
A6 Bowl Rim RS :	6,3	6,3
Piston Bowl mean error	0,8	4,4
B1 Groove 1 ATS :	9,5	9,7
B2 Groove 1 TS :	11,4	9,1
B3 Groove 1 FS :	0,1	-1,2
Piston Groove mean error	7,0	5,9
C1 Pin Boss RS :	0,5	-1,6
C2 Support FS :	-5,0	-3,7
C3 Pin Boss FS :	-3,9	-4,2
Piston Pin Boss mean error	-2,8	-3,2
D1 Top Land FS :	-19,6	-14,4
D2 Top Land ATS :	-16,6	-16,5
Piston Top Land mean error	-18,1	-15,5
Reference temperature RMS error		
RMS error	8,79	8,33
Heat Flux		
Heat input [W]	4382	5180
Cooling gallery output [%]	59,24%	59,92%
PRA output [%]	21,31%	21,60%
Undercrown output [%]	10,19%	8,86%
Skirt output [%]	6,56%	6,69%
Pin boss output [%]	1,23%	0,78%
Pin face output [%]	1,39%	2,03%

Figure 6.9: Reference temperature difference and piston boundary heat flux distribution.

6.3.2 Validation results for assumed engine load cases

Similarly to subsection 6.3.1, the validation results are presented as piston structure temperature fields for the assumed engine load cases of 117 kW at 2250 RPM and 153 kW at 3375 RPM in Figures 6.10 to 6.12 and in Figures 6.13 to 6.15 respectively.

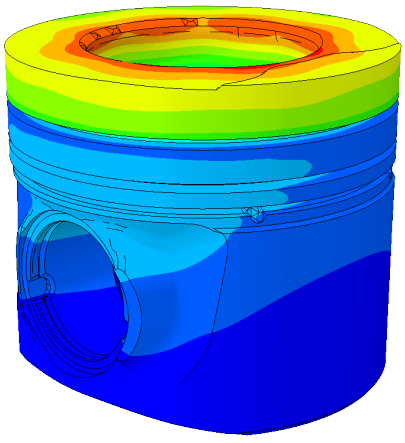

Figure 6.13: Isometric view of the piston temperature field for 153 kW at 3375 RPM.

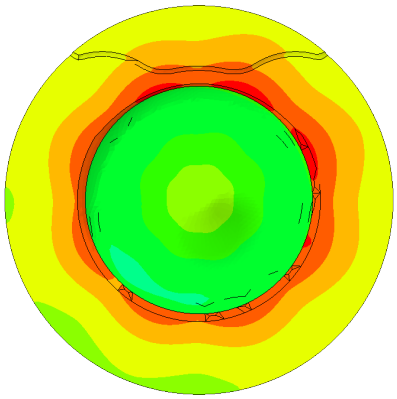

Figure 6.14: Top view of the piston temperature field for 153 kW at 3375 RPM.

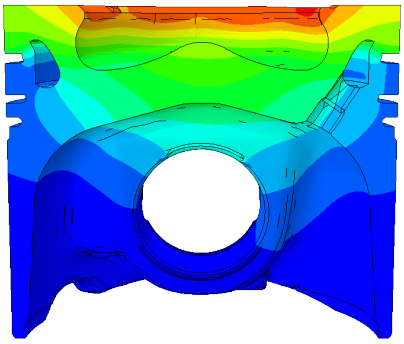

Figure 6.15: View of ATS-TS cut section of the piston temperature field for 153 kW at 3375 RPM.

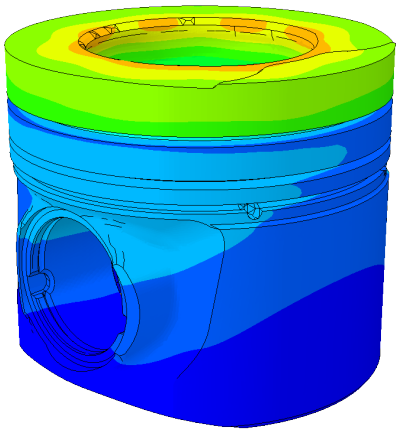

Figure 6.10: Isometric view of the piston temperature field for 117 kW at 2250 RPM.

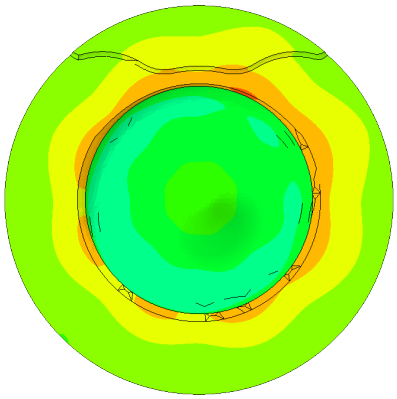

Figure 6.11: Top view of the piston temperature field for 117 kW at 2250 RPM.

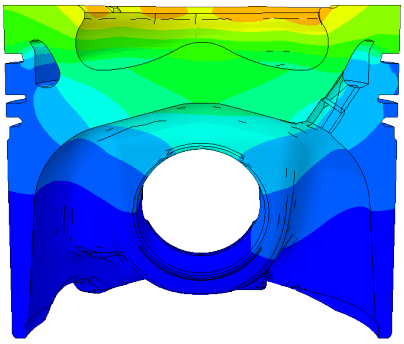

Figure 6.12: View of ATS-TS cut section of the piston temperature field for 117 kW at 2250 RPM.

In Figure 6.16 the heat flux distribution over the piston boundaries for the assumed validation load cases can be seen.

	117 kW | 2250 RPM
Heat Flux	
Heat input [W]	3440
Cooling gallery output [%]	55,93%
PRA output [%]	23,62%
Undercrown output [%]	11,63%
Skirt output [%]	6,63%
Pin boss output [%]	0,85%
Pin face output [%]	1,28%

	153 kW | 3375 RPM
Heat Flux	
Heat input [W]	4329
Cooling gallery output [%]	54,03%
PRA output [%]	18,77%
Undercrown output [%]	9,61%
Skirt output [%]	5,27%
Pin boss output [%]	0,67%
Pin face output [%]	1,02%

Figure 6.16: Piston surface heat flux distribution for load cases 117 kW at 2250 RPM and 153 kW at 3375 RPM.

7 Engine heat balance with respect to piston heat flux

With a calibrated 3D thermal piston model according to the constraints and measurement data it was possible to determine how much of the heat flux entering the piston top from the combustion that would be transferred through the piston rings and outer piston surfaces. This in turn meant that the heat flux at the piston grooves and outer surfaces would be absorbed by the cylinder liner which then is further propagated through the whole engine, contributing to the complete heat balance of the engine. A method of transferring the heat flux from the piston outer surfaces to the cylinder liner was developed. The heat flux data was needed to be converted to heat flux per unit area for it to be applicable in the Abaqus solver. Figure 7.1 shows the step in the solution strategy.

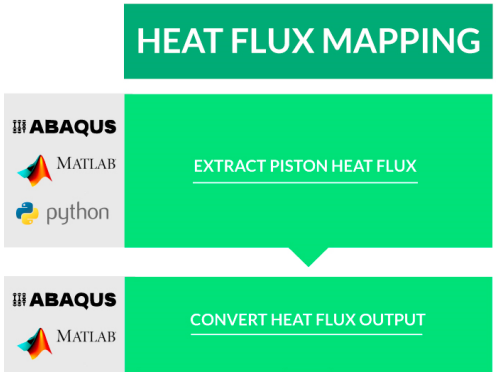

Figure 7.1: Solution strategy: Heat flux extracting & converting.

Due to the geometry of the piston grooves, a method of converting the piston grooves fluxes to mimic piston ring heat fluxes was performed. The heat flux extraction and conversion is explained in subsection 7.1.

The feasibility of the heat flux per unit area conversion was validated by applying the converted heat flux on to the piston outer surfaces and performing a thermal analysis with the heat flux per unit area loads. This is explained in subsection 7.2.

For the piston-to-cylinder thermal interaction, it was necessary to take into account the reciprocating motion of the piston within the cylinder with respect to the emitted heat flux. The heat flux per unit area load was mapped with respect to the piston motion on to the cylinder liner with an in-house developed mapping routine. See subsection 7.3 for a detailed explanation.

7.1 Extracting and converting the piston heat flux

Abaqus does not support an element output which would give a heat flux per unit area, $[W/m^2K]$. The heat flux load supported in Abaqus is denoted DFLUX [1], which is applied as a heat flux per element area. Therefore it is necessary to have such a format for the mapping routine to be applicable on the cylinder liner. However, Abaqus does support the output of total nodal heat flux $[W]$, denoted RFLE [1]. As such, the authors of this thesis developed a Python script run within Abaqus and a MATLAB program to convert the RFLE values to a mappable DFLUX load. Figure 7.2 graphically clarifies the conversion procedure.

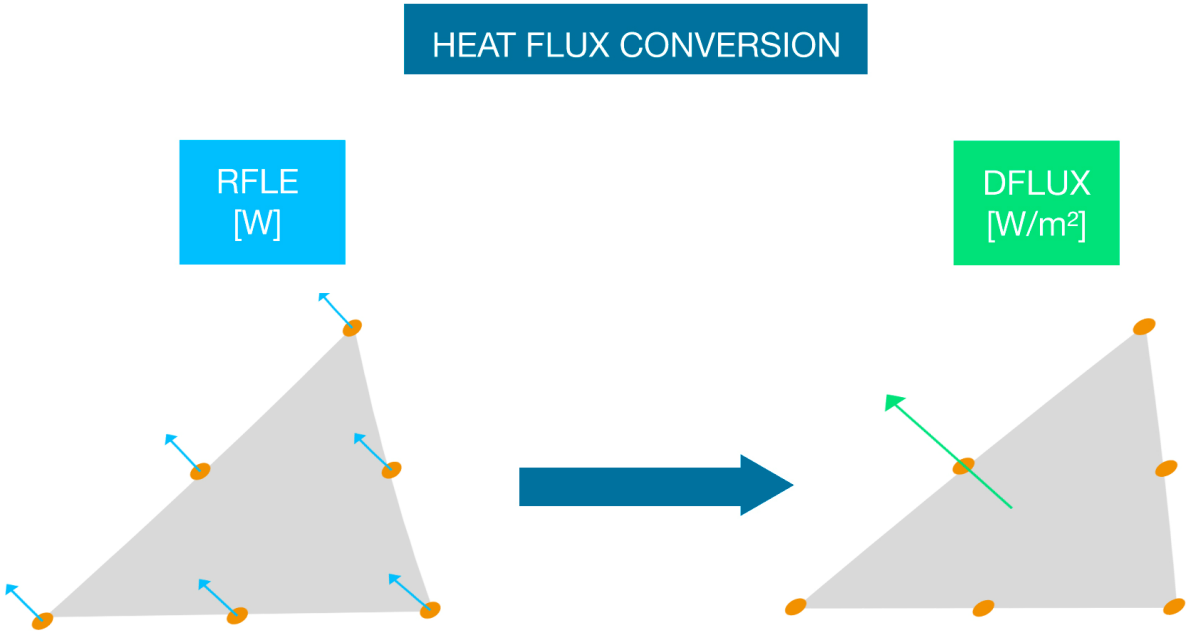

Figure 7.2: Heat flux conversion

The Python script performed the following tasks:

- Extracted the total nodal heat flux, RFLE, for the piston outer element surface facets.
- Extracted the element information consisting of element ID, surface facets ID, connected nodes ID and node coordinates.

With the extracted data, a MATLAB program was developed to convert the RFLE to DFLUX.

The MATLAB program performed the following tasks:

- Determined which nodes were connected to respective element surface facet.
- Determined how many elements were coupled to the nodes.
- Divided the RFLE-value of the nodes with the number of coupled elements.
- Calculated the sum of the RFLE for surface facet of the element.
- Approximated the area of the second order element facet based on the node coordinates.
- Calculated the element facet center position.
- Moved the center position to a radius equal to the cylinder liner inner radius.
- Converted the element RFLE summation and element facet approximated area to a DFLUX load of unit $[W/m^2]$.
- Moved the converted DFLUX to the center position of the element facet.

The division procedure of the RFLE-values was necessary to be performed. As RFLE is the total nodal heat flux one must take in to account how much each element contribute to the total nodal heat flux [1].

While this method worked perfectly for flat surfaces, the piston grooves needed to have several more steps in the conversion from RFLE to DFLUX load.

Another MATLAB program specified for the piston grooves was developed with the previous code as base. Additional steps to the groove conversion were added:

- Summed the converted DFLUX loads for the ring groove elements within a 2.5° circumferential range.
- Moved the summed DFLUX load to the center height position of the groove, which in turn was meant to represent the piston ring at this groove.

The end result was a CSV-file consisting of information such that it was mappable as a DFLUX load with the in-house mapping routine.

7.2 Validation of the mappable heat flux data

The mappable DFLUX load's accuracy was validated by removing the convective thermal loads on the piston outer surfaces and re-running the thermal analysis in Abaqus with the mapped DFLUX load. The temperature field and the piston boundary heat fluxes of the piston were compared to the original calibrated piston results.

7.3 Mapping the piston heat flux on the cylinder liner

With the piston heat flux converted from RFLE into the DFLUX file, it should be mapped onto the cylinder liner. An in-house Python mapping program was available at Volvo Cars. However, the mapping program could not handle moving objects nor was it able to map the heat flux load DFLUX. Using the source code as a starting point, the necessary modifications for the initial Python program to be able to perform the described tasks was implemented. Figure 7.3 shows the step in the solution strategy.

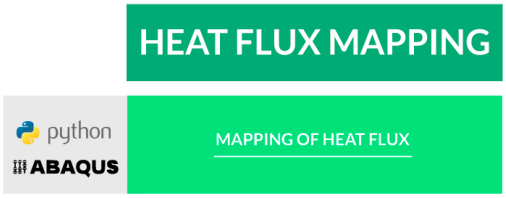

Figure 7.3: Solution strategy: Heat flux mapping.

An equation describing the piston motion based on the crank radius and crank arm for each crank angle degree was implement to the code and is shown eq 7.1.

$$x = rcos(\phi) + \sqrt{l^2 - r^2 sin(\phi)^2} \tag{7.1}$$

In eq 7.1, r is the crank radius, l is the crank arm length, ϕ is the crank angle and x is the piston stroke position.

The modified Python script did the following:

- Extracted the surface information of the cylinder liner consisting of element ID, facet ID, nodes ID, and node coordinates.
- Calculated the stroke position of the piston.
- Mapped the heat flux at the stroke position on to the cylinder liner elements within a prescribed search radius.
- Repeated the mapping for every crank angle degree of a complete four-stroke cycle.
- Calculated the cycle averaged exposure of the heat flux per unit area for every mapped cylinder liner element.

The final results were then saved to a DFLUX load file which could be included in a thermal analysis of the complete engine.

7.4 Results from element surface heat flux extraction and mapping

The following sections presents:

- The heat flux extraction and conversion results from the piston outer surfaces and grooves.
- The cylinder heat flux mapping results.
- The validation results of the heat flux mapping method.
- A demonstration of a thermal analysis with the applied piston heat flux to the cylinder liner.

An explanation of the heat flux mapping method was given in subsections 7.1 and 7.3.

7.5 Results from extracted heat flux from piston

Figures 7.4 to 7.7 shows the extracted and converted piston surface heat flux per unit area from four angles of the piston. The heat flux per unit area results are plotted at corresponding piston elements. The colour plot intensity represents the magnitude of the heat flux.

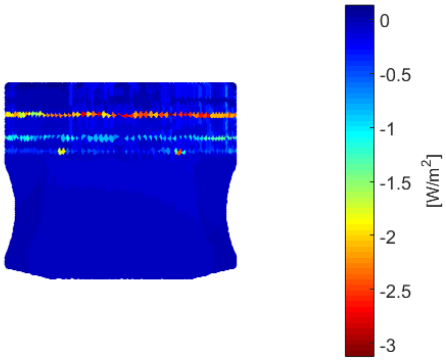

Figure 7.4: TS-view.

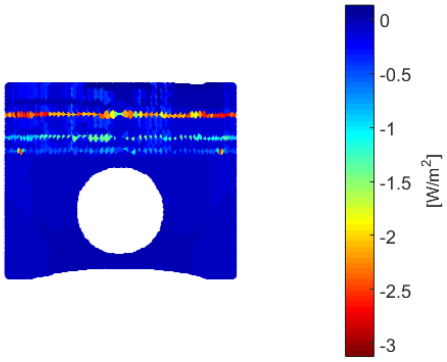

Figure 7.5: FS-view.

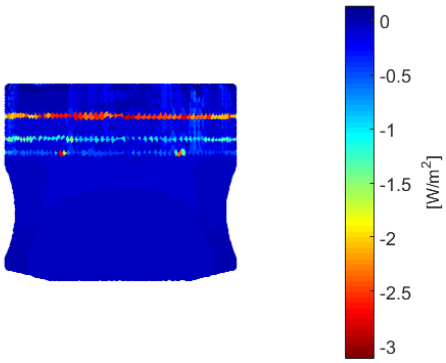

Figure 7.6: ATS-view.

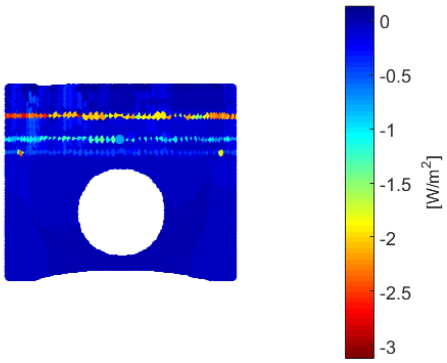

Figure 7.7: RS-view.

7.6 Heat flux mapping on cylinder liner

Figures 7.8 to 7.11 show the results of applying the piston heat flux on to the cylinder liner with respect to the piston motion. Each figure shows the cylinder liner from a different angle.

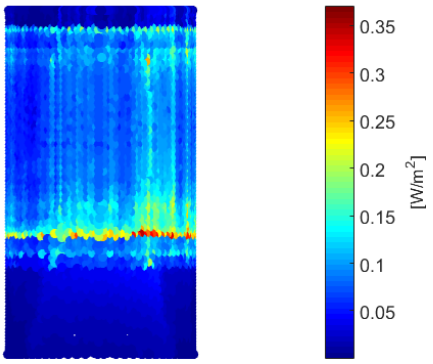

Figure 7.8: 0° rotation.

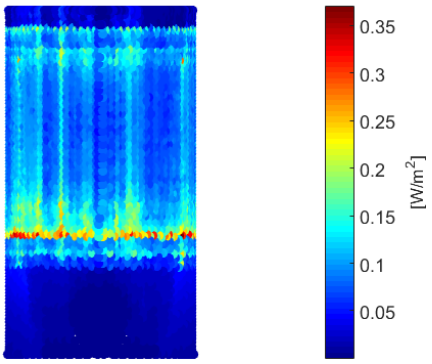

Figure 7.9: 90° rotation.

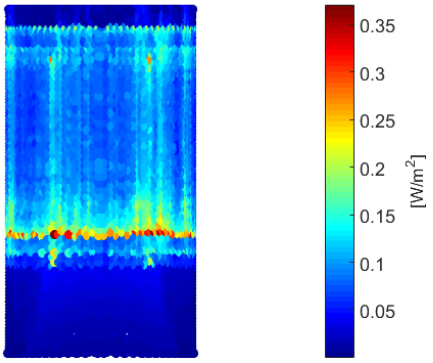

Figure 7.10: 180° rotation.

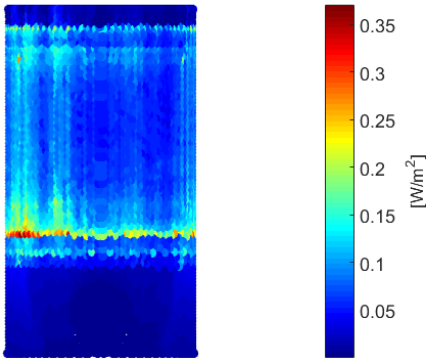

Figure 7.11: 270° rotation.

7.7 Validation of heat flux mapping results

Validation of the heat mapping results was conducted according to subsection 7.2. The validation was conducted for the engine load case 170 kW at 4000 RPM. The results of the validation are presented as follows:

- The temperature field of the piston structure from the FE-analysis of the piston with surface load mapped as DFLUX load.
- Reference temperature differences in measurement points.
- Piston surface heat flux distribution.

For comparison, the temperature difference and heat flux distribution FE-analysis results from the original convection load case 170 kW at 4000 RPM are presented next to the validation results in Figure 7.15.

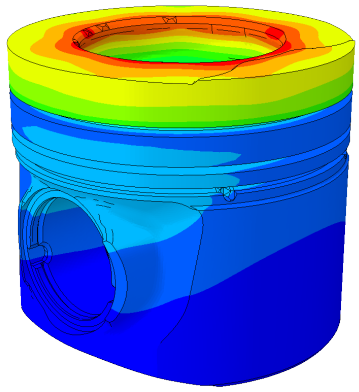

Figure 7.12: Isometric view.

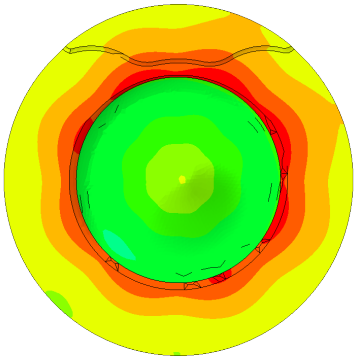

Figure 7.13: Top view.

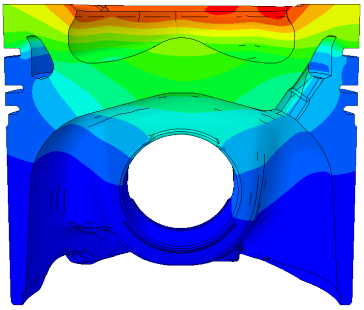

Figure 7.14: View of ATS-TS cut section.

170 kW | 4000 RPM	Original	Validation
Reference temperature difference		
A1 Bowl Center :	8,7	8,3
A2 Bowl Rim TS :	-0,5	-0,6
A3 Bowl Rim ATS :	-1,3	-1,4
A4 Bowl Rim FS :	19,0	18,8
A5 Bowl Ground ATS :	-6,4	-6,9
A6 Bowl Rim RS :	8,2	8,2
Piston Bowl mean error	4,6	4,4
B1 Groove 1 ATS :	10,8	9,9
B2 Groove 1 TS :	10,9	10,2
B3 Groove 1 FS :	2,6	1,7
Piston Groove mean error	8,1	7,3
C1 Pin Boss RS :	-2,3	-2,8
C2 Support FS :	-2,4	-3,0
C3 Pin Boss FS :	-0,7	-1,4
Piston Pin Boss mean error	-1,8	-2,4
D1 Top Land FS :	-9,2	-8,8
D2 Top Land ATS :	-13,0	-12,7
Piston Top Land mean error	-11,1	-10,8
Reference temperature RMS error		
RMS error	9,78	9,52
Heat Flux		
Heat input [W]	5426	5435
Cooling gallery output [%]	59,92%	59,50%
PRA output [%]	21,54%	22,04%
Undercrown output [%]	9,71%	9,59%
Skirt output [%]	6,19%	6,10%
Pin boss output [%]	0,27%	0,26%
Pin face output [%]	2,28%	2,24%

Figure 7.15: Comparison of original load case and heat flux validation mapping results.

7.8 Applying the piston heat flux on to the cylinder liner

The converted piston heat flux load was applied to the cylinder liner of an engine thermal FE-analysis model. The FE-analysis did not include the thermal load from the fuel combustion. However, the engine coolant- and the crankcase oil thermal loads were setup. The results in Figure 7.16 thus shows a temperature field cross section contour plot of two cylinders of the engine with the applied piston heat flux load. Due to confidentiality, only a small portion of the engine block is presented.

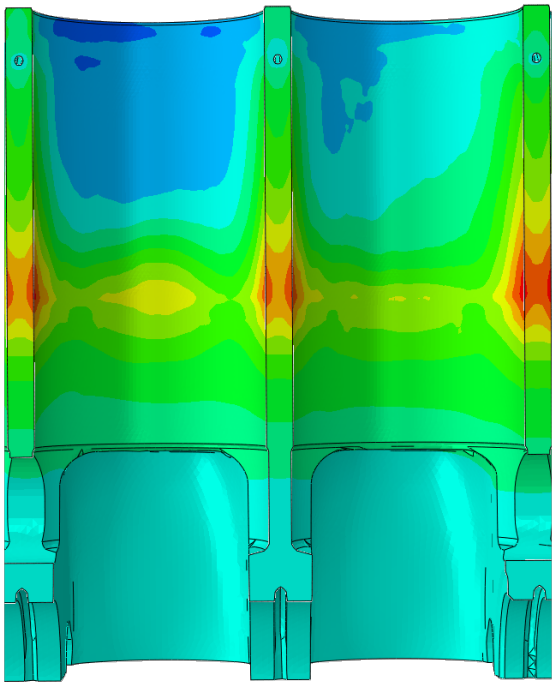

Figure 7.16: Temperature field in the engine block cross section.

8 Discussion and conclusions

The following chapter will evaluate the methodology applied for the thermal analysis of the piston by discussing the reference measurement data, the results of the 2D and 3D parameter calibrations, the constructed complete thermal analysis piston model, the piston heat flux mapping method. Recommendations for future work and investigations within the field will also be proposed.

8.1 Measurement data

The authors of this thesis observed that the temperature measurement data supplied by the piston manufacturer Mahle had strange characteristics for one of the top land measurement points. The measurement data at the top land point in mind, "D2 Top Land FS" in Figure 5.2, did not behave characteristically with increasing engine speed and assumed a constant temperature early in the engine speed range. The measurement point value was manually adjusted based on how the rest of the temperature measurement points behaved with respect to engine speed. It is necessary to have this in mind when discussing the results as this affects the optimization algorithm's objective function. Another measurement point, Bowl ground FS, was deemed by the measurement report to be false. As such, the authors did not take this point into account for the parameter calibration.

8.2 2D axisymmetrical thermal analysis piston model

The advantages, flaws and the feasibility of the results for the 2D axisymmetrical modelling technique will be evaluated in this section.

Based on the results of the 2D parameter calibration from Figures 4.9, 4.10 and 4.11, the in-house developed MATLAB program was able to calculate the unknown boundary HTCs for each surface of the piston with respect to the temperature field which corresponds well to the temperature measurement data and heat flux guideline proportions.

With this being a simplified model with a 2D axisymmetrical geometry, the averaged temperature calibration point values explained in section 4 were concluded to be a valid method to use. The goal of this method was for the 2D parameter calibration to result in HTCs which should be considered as averaged for the diesel piston. If one was to base their parameter calibration for certain measurement points, in the TS region for example, the 2D parameter calibration would not represent the average piston temperature field and rather the specific region.

In Figure 4.12, the top groove of the piston has a higher HTC compared to the other piston surfaces. From the performed literature study about the thermal properties of diesel pistons with a ring carrier design, this is true [10]. A conclusion is thus that the parameter calibration was able to capture a true occurring physical phenomena. The feasibility of the remaining PRA and skirt HTCs could therefore be assumed to be within a reasonable accuracy of the actual HTC value. Based on the results, the assumed piston ring ratio factor, explained in subsection 4.2.2, proved to be a suitable method for constructing a time-averaged simplified ring dynamics model.

The temperature difference shown in Figure 4.10 can be explained by taking into account the following uncertainties:

- The accuracy of the CFD-data which the piston top HTC and temperature is based on.
- The high uncertainty of the undercrown thermal behaviour.
- An area-averaged expression of the cooling gallery HTC.
- The 2D axisymmetrical model does not contain all the geometrical information of the actual piston.

The authors of this thesis were able to manipulate the developed MATLAB optimization program in such a way that the temperature difference would be equal to zero. A consequence of this was that the characteristics of the calibrated HTCs were highly unphysical. With a more constrained and boundary set optimization routine,

the resulting temperature difference can be considered as valid for the 2D axisymmetrical model given the geometrical differences between the 2D axisymmetrical and 3D models and the uncertainly factors.

The heat flux distribution of the piston structure is a fundamental constraint for the parameter calibration through optimization to be a viable solution method. Without the set heat flux constraints, the heat transfer could reach levels which were out of bounds of a ring carrier designed diesel piston, while still being able to solve the temperature field with respect to the temperature measurement data. The HTCs were interpreted as unphysical for these parameter calibrations as the boundary heat flux distributions were violated. As the boundary heat flux is of such high importance for the reliability of the solution, it is necessary to have accurate heat flux data from the combustion. The values given by GT-Power simulations are therefore crucial to be within a feasible range for this parameter calibration method to be a viable solution strategy. A consequence of this is that improvements to the GT-Power simulations should therefore directly increase the accuracy of the developed parameter calibration method.

The 2D axisymmetrical simplification of the piston geometry resulted in an incorrect heat flux analysis since some surfaces of the piston, i.e. the pin boss, pin face and the varying undercrown geometry, were not correctly represented. As such, the distribution of the heat flux could not be spread to these piston surfaces. The missing surfaces were properly modelled and taken into account for the 3D thermal analysis piston model.

Therefore, the 2D axisymmetrical model is simply not suitable as a final solution and a more sophisticated 3D thermal analysis must be performed. However, The HTC values of the 2D axisymmetrical parameter calibration are very suitable as initial HTCs for a 3D parameter calibration as the 2D parameter calibration can be considered as averaged across the actual diesel piston.

The empirical correlations by Woschni, Hohenberg, Annand and Ma and Seale and Taylor, see subsection 2.3.1, gave results which were difficult to interpret as physical as mentioned in section 4.2.1. A recurring problem was a strange behaviour near the top land region. A possible explanation of this can be that an occurrence related to friction near the top land was the reason for this behaviour. Since friction was not modelled in this thermal analysis piston model, the optimization routine would compensate the lack of friction by manipulating the HTC values to obtain lower objective functions. After discussions with CFD-engineers at Volvo Cars made it was concluded that the parameter calibrated HTC function based on the empirical correlations was unlikely to be true. Therefore, the authors of this thesis choose to base their piston top load on numerical CFD-analysis of the combustion as it was a better physical representation of the piston top thermal behaviour.

Figure 4.10 shows that the largest temperature difference can be observed for the top land measure point with the CFD-data as piston top thermal load.

Five possible explanations for this has been considered:

- There is a significant heat generation by friction on the piston top land.
- Parts of the piston top load should include the piston top land.
- The CFD analysis may be inaccurate.
- The modelling technique of conductive thermal circuit for the top land needs improvements.
- As stated in section 8.1, the top land temperature adjustment due to the concluded error in the measurement data report might be wrong.

Each of the stated explanations contribute to why the biggest temperature difference occurs at the piston top land. Further investigation of the thermal properties around this area should be performed for a better understanding.

The cooling gallery actual HTC depends of many factors [10] such as:

- Oil fill ratio.
- Splashing effect.

- Flow in the channel.
- Temperature difference of the cooling oil.
- Piston motion.

These factors can be considered to be included in the optimization routine and thereby changing the initial HTC value to a more feasible one. Based on the studies of cooling galleries [28], the HTC varies on the channel surfaces. The calibrated HTC value should therefore be considered as a mean HTC based for all the surfaces in the cooling gallery. For a spatial expression, the authors recommend further thermal analysis with numerical methods for the cooling gallery.

The undercrown area was the most difficult boundary condition to model. The only studies for the thermal properties of the undercrown of a piston either assumed a certain type of values [[16], [26]] or were investigated for piston with oil jet spray cooling mechanism [3]. The authors choose the Gnielinski correlation as it varies with piston speed, due to the Reynold number, and would therefore scale depending on the load case due to engine speed. As one can see from Figure 4.8, the exponential curve fitting approximation fits well with the optimized values. The $h_{und}(r)$ function increases in value as it reaches the end of the piston skirt. Due to the temperature measurement points in Figure 4, the undercrown thermal load mostly affected the Bowl center and Bowl ground temperatures and did not have a reference temperature further down the boundary, see Figure 4. From a purely optimization point of view, this could explain why the curve increases with the radius as it does not affect the objective function after a certain radius point. From a physical point of view, this type of thermal behaviour can be interpreted as reasonable. The pin boss obscures the middle area of the undercrown and could possibly have worse heat transfer properties than the piston skirt which is directly exposed to the oil mist in the engine cylinder. An observation to be made is that the derived undercrown function $h_{und}(r)$ follows the same pattern as the one Woschni and Fieger estimated [27], i.e. it increases with radius. Further investigation of the actual HTC for the undercrown is recommended for a better understanding.

As one can understand by the evaluation of the 2D axisymmetrical parameter calibration model, the results of the 2D axisymmetrical parameter calibration has certain built-in uncertainties. However, the 2D axisymmetrical parameter calibration model results in Figures 4.9, 4.10 and 4.11 give a good understanding of the actual thermal behaviour of the piston. The calibrated parameters would therefore be well suited as initial HTC values for a more advanced 3D parameter calibration.

8.3 3D parameter calibration model: Rated engine load

By observing the result in section 5.10, particularly in Figure 5.10, one can see that the methodology of calculating the piston boundary HTCs used throughout this thesis work gives satisfyingly accurate results in terms of solving the temperature field of the piston. One must take into account that 25 variables were able to be adjusted and 13 constraints where set for the 3D parameter calibration to take into account. For this problem to be solvable, the initial input values need to be well estimated and given a rather narrow range of adjustment. A conclusion that can be drawn is that the 2D parameter calibration model gave well estimated values as the 3D parameter calibration was solvable and reached convergence after about 1000 iterations, which translated to computational time with a 16 core cluster is about 5000 minutes.

The temperature differences that although occurs can be explained by:

- Possible limitations of the mathematical optimization algorithm.
- Thermal effects that are not modelled, such as radiation and friction.
- The piston region division, ATS, TS and FS/RS, was not great enough.
- The assumption of a sinusoidal cubic polynomial expression of HTC top load and temperature based on CFD and GT-Power data was slightly inaccurate.
- The derived $h_{und}(r)$ from the 2D parameter calibration did not fully represent the thermal properties of the undercrown.

- The area-averaged method used to model the cooling gallery, as explained in subsection 5.4, was a to grave estimation.

Regarding the limitations of the optimization algorithm used, the authors of this thesis chose the Nelder-Mead simplex algorithm for the 3D parameter calibration as it yielded good results for the 2D parameter calibration. A correspondence with Esteco, the software developer of modeFrontier, was done in which the 3D parameter calibration problem was discussed. A recommendation of using the Levenberg-Marquardt algorithm was given by Esteco. However, the authors of the thesis were not able to properly setup the optimization routine with this gradient based algorithm, even with direct support from Esteco. Given that the authors had a basic understanding of optimization before attempting to solve the thermal analysis problem through optimization, a better knowledge of the mathematical algorithms and optimization could possibly improve the thermal analysis parameter calibration even further.

As with the 2D axisymmetrical model, the radiation and friction were not included as variables in the 3D parameter calibration. This in turn causes the HTCs of the 3D parameter calibration to include the effect of the radiation and friction in the convection variables. While the radiation and friction are of smaller significance [10], it is important to understand that the thermal properties were simplified by neglecting the radiation and friction.

Compared to the 2D axisymmetrical piston model, the 3D piston model is an actual geometrical representation of the diesel piston. As such, a more accurate thermal behaviour is able to be analyzed. With this in mind, one must understand that the thermal properties varies greatly across the piston body due to the piston motion within the engine, the nonuniform combustion, the cooling gallery shape, and the non-axisymmetrical construction of the piston. It is therefore crucial to create a more spatial variation of the HTCs across the piston body as otherwise it would be a too great simplification, which would result in imprecise results. Given the complexity of the piston thermal properties, i.e. variation on the piston top, undercrown, cooling gallery, each piston groove, land, skirt, pin face and the pin boss, the piston was necessary to have a finite number of regions to be divided into. If one were to setup a varying HTC for every point on the piston, the attempted optimization method would most certainly be unsolvable due to the shear number of adjustable variables.

The number of regions chosen to divide the diesel piston into was motivated by where the measurement temperature points where located in temperature measurement report and which parts were deemed to be more important to analyze. The 14 calibration points are shown in Figures 5.2 to 5.3. As one of the objectives of this thesis was to understand the piston-to-liner thermal interaction, the PRA, skirt and pin faces were of higher importance than the pin boss and the undercrown. With this in mind (the location of the measurement points and the understanding of piston-to-liner thermal interaction) the piston was divided into the ATS, TS and FS/RS sections for a spatial variation. While this was a limitation of the constructed thermal analysis model, based on the results, it was a proper way to divide the diesel piston. The temperature field and the heat flux proportions were able to be solved and corresponded well to the temperature measurement data and heat flux guidelines.

The sinusoidal cubic polynomial functions $h_{Top}(r, z, \phi)$ and $T_{gas}(r, z, \phi)$, seen in equations 5.1 and 5.2, for the piston top load were explained in subsection 5.2.1. The assumption of a sinusoidal variation to resemble the combustion propagation can be concluded to be valid based on the piston top temperature results, A1 to A5 in Figure 5.10, where the temperature differences are in single digit range with mean errors of 4.0, 3.4 and 4.6. However, a larger temperature deviation is observed for temperature measurement point A4. The reasons for this temperature deviation can be plenty.

- The assumed linear increase of the cooling oil temperature could be improper.
- The combustion may be inaccurately resembled.
- The temperature measurement from Mahle may have errors.

Since the other bowl rim and bowl ground temperature measurements points showed good correlation with temperature measurement data, it is an indication that the thermal top- and cooling gallery loads were properly applied. Consequently, one can assume that the location of the A4 temperature measurement point was different from where the nodal temperature value was extracted in the FE-analysis. This is a common mistake when dealing with experimental measurement data since the exact measurement point location can be difficult to resemble in a FE-structure. Another possibility is that the measurement point may have displaced during the

measurements.

A reoccurring result for all the parameter calibration setups were higher temperature differences at the piston groove points B1, B2 and B3 in Figures 5.10 and 6.9. An investigation of why this happened was performed.

Three explanations were concluded:

- Uncertainties in material data.
- Incorrect placements of the reference points (B1, B2 and B3).
- Coarse mesh resolution.

The top groove consists of a cast iron material compared to the majority of the piston structure, which is made of an aluminium alloy. The cast iron material has a much lower thermal conductivity than the aluminium alloy material. This defines the structure of the diesel piston as a ring carrier type. The purpose of the ring carrier design is for the top piston ring to attain lower thermal stresses. The authors did not have access to the exact material data of the piston and therefore some uncertainties of the material thermal conductivity exists.

When modelling the 3D piston FE-model, the placement of the reference points (B1, B2 and B3) had a considerable impact on the calculated temperatures. If one was to place the reference point a couple millimeters off, the calculated temperatures would be significantly higher than the measured ones. As such, the sensitivity of these points is of high level.

Given the explained sensitivity, a higher resolution mesh around the top groove would possibly reduce the sensitivity of the point placement. Consequently, further refinement of the mesh within this area is recommended.

The explanation of the undercrown complexity was described in section 8.2. The assumed exponential function corresponds well to temperature measurements C1 to C3 in Figure 5.10, and is well within the boundary heat flux proportions. Hence, this type of thermal load modelling the undercrown can be concluded to be a valid estimation. To increase the understanding of the actual physics of the undercrown, a more sophisticated analysis is highly recommended.

A fundamental part of understanding the diesel piston thermal properties is based on how the cooling gallery HTC is modelled. A spatial expression of high resolution would be ideal as it would properly capture the many factors, explained in section 8.2, which occur in the cooling gallery. However, given that no analytical methods or empirical correlations were found during the literature study which were able to perform this, and no CFD-data was available to be utilized, the authors of this thesis tried to model the cooling gallery as detailed as possible with the information available at hand.

The cooling gallery inlet, outlet and channel were modelled separately. Each of the cooling gallery sections would have its own HTC and temperature. The channel was divided into two parts, each with a varying temperature which should replicate the cooling oil gradual temperature increase. A more detailed explanation of this is given in subsection 5.4. While this method might not be feasible for an actual analysis of the physics in the cooling gallery, it can be concluded to be practical for mean HTCs of the cooling gallery. To further improve the results, a more in-depth analysis of the cooling gallery is recommended to be performed.

As with the 2D axisymmetrical parameter calibration model, the 3D parameter calibration model has its flaws. However, the results presented in section 5.10 are well within an acceptable RMS error of under 10 and all of the heat flux constraints are satisfied. The majority of the temperature differences are within a sub $10°C$ margin error. As explained previously in section 8.1, one must consider that the D1 point was manually adjusted, which does effect the results in one way or the other. A conclusion by the authors is thus that this type of parameter calibration for a 3D thermal analysis piston model is suitable. A better understanding of the physics of the cooling gallery, undercrown, friction, radiation, ring dynamics and top load would further improve the results.

8.3.1 3D CFD thermal analysis piston model

The thermal analysis piston model with the mapped CFD combustion data as piston top load was not further developed, as mentioned in section 5.9 The CFD model resulted in slightly higher reference temperature differences in the temperature measurement points of the piston compared to the sinusoidal cubic polynomial function model.

The reason for these minor temperature differences are considered to be due to the following factors:

- The 3D CFD parameter calibration model had fewer parameters for the piston top surface load.
- The CFD-data at hand was calculated for a specific load case, namely for max load arising at 170 kW and 4000 RPM.

The fact that fewer parameters could manipulate the mapped CFD-data than in the case of a piston top load expressed as a sinusoidal cubic polynomial function may have resulted in that the optimization algorithm was unable to minimize the objective function as efficiently.

The CFD-load was calculated for maximum engine load, which is more likely to affect the results of the parameter calibration greatly. As the thermodynamics of the combustion will behave differently for different engine loads, consequently the CFD-data will vary accordingly. The spatial temperature and heat transfer coefficient distribution will most likely differ compared to the used max load CFD-data. Since the parameter calibration only was able to manipulate the amplitude and offset for the HTCs of the CFD-data, the diesel piston gas surface temperature remained unchanged. This is a likely explanation for the less precise results yielded by the 3D CFD thermal analysis piston model. As for the sinusoidal cubic polynomial top surface load, the mean gas temperature was taken into account according to the results of the GT-Power simulations, hence the actual engine load case could more precisely be resembled.

8.4 3D parameter calibration model: Assumed engine load

An attempt to calculate how the diesel piston thermal behaviour changes with an increase or decrease in power output was performed. The initial HTC values for these calculations were the results of the 3D parameter calibration for the rated engine loads.

The assumed proportional increase or decrease of the heat flux from combustion with respect to the power output was decided to be the method of choice for determining the heat flux input for varying loads, see explanation in subsection 5.8. The assumption was done as the attempted GT-Power simulations with a power output variation resulted in unfeasible piston top heat fluxes.

Two explanation for this were concluded:

- The diesel piston and cylinder wall surface temperatures were not adjusted.
- The ignition timing was not adjusted.

This was discovered at the end of the thesis and simulations were not able to be re-run given the set time limit. As the authors wanted to construct a thermal analysis piston model which was dependent on both engine power output and speed and not solely on engine speed, the stated input heat flux change assumption was made.

The authors want to be clear, that for a more accurate thermal analysis piston model the 3D parameter calibrations for the assumed engine loads should be redone with adjusted GT-Power heat flux data.

With the stated heat flux assumption, the choice of optimization with no temperature measurement data meant that the parameter calibration took another approach as it was only based on heat flux, see subsection 5.8 for a more in-depth explanation. As one can see in Figures 6.10 to 6.16, not only were the parameter calibrations successful, they also resulted in feasible results, i.e. higher or lower constrained temperature fields and heat fluxes within the set guideline proportions.

To model the true thermal properties for varying power output, actual measured temperatures to calibrate against would be necessary. As none were available, one can consider the 3D parameter calibration method with assumed engine loads to be valid and the results as feasible, but with an uncertain truthfulness to the temperature field.

8.4.1 Sensitivity of the thermal load

Section 5.13 shows the results of the sensitivity analysis that was performed. As explained in section 5.12, the purpose of the sensitivity analysis was to determine how the parameters affect the thermal analysis piston model's results.

Based on Figure 5.18, the temperature field does not change in any significant way for most of the thermal loads. The biggest thermal loads, i.e. the top load, cooling gallery and the complete ring belt setup, are the ones which affect the temperature field the most. One can draw a connection between the amount of heat flux conducted through the surface and the effect it has on the temperature field. This comes as no surprise and therefore one can validate that the sensitivity analysis was performed correctly and results are true.

A conclusion from the sensitivity analysis is that the HTCs for the majority of the thermal loads have a wide range of possible magnitudes while still being able to calculate a feasible temperature field. As such, one cannot simply focus the results of the HTCs solely on the temperature field.

Figure 5.19 shows how the boundary heat fluxes change with a variation of the HTCs. The figure clearly shows that the heat fluxes are more sensitive to a variation of the HTCs than the temperature field. An interpretation of the results is thus that while one might be able to calibrate the temperature field, the HTCs might result in unphysical values if one does not take the heat fluxes into consideration. A possibility to minimize the unfeasibility of the HTCs while ignoring the heat fluxes is by having a significant more number of calibration points from experimental temperature measurements, which might be troublesome and expensive. Parameter calibrations without heat flux constrains were performed by authors and the results of this were explained in section 8.2. The results were as expected, i.e. the HTCs after calibration were unphysical while still solving the temperature field.

As the authors of this thesis performed the calibration with respect to the heat fluxes, the feasibility of the results should therefore be of higher degree than if no consideration to the heat fluxes were taken.

8.5 Complete thermal analysis piston model

A total of nine 3D parameter calibrated models were constructed.

- Three rated engine loads based on temperature measurement data and heat fluxes.
  - 170 kW at 4000 RPM.
  - 135 kW at 3000 RPM.
  - 100 kW at 2000 RPM.
- Six assumed engine loads strictly heat flux based.
  - 180 kW at 4000 RPM.
  - 160 kW at 4000 RPM.
  - 145 kW at 3000 RPM.
  - 125 kW at 3000 RPM.
  - 110 kW at 2000 RPM.
  - 90 kW at 2000 RPM.

It was concluded that a complete thermal analysis piston model would be able to be constructed with the calibrated data. The authors chose to apply linear interpolation as it was the simplest one to evaluate. The developed MATLAB program requests the user to input a power engine output and a range of feasible engine

speeds are able to be selected. The program then calculates the HTCs for each surface of the diesel piston based on the region division explained in subsection 5.3 and illustrated in Figure 5.5.

In total, 387 different engine load cases are able to be analyzed ranging from 2000 to 4000 RPM and 90 to 180 kW. Figure 6.2 shows an example of how the HTC varies for the cooling gallery across the whole engine load case range. See Appendix A.5 for all the $\boldsymbol{h}(RPM, kW)$ matrices.

The linear interpolation model was needed to be verified. This was done in several steps. First, the authors decided to validate the model by comparing the calculated temperatures to the measurement data.

Two rated engine load cases were used for this:

- 122 kW at 2500 RPM.
- 152 kW at 3500 RPM.

The piston top, undercrown, ring assembly, skirt, cooling gallery, pin face and pin boss HTCs and the gas surface temperature were all taken form the constructed interpolation program. A thermal analysis of the 3D model with the extracted HTC was then performed with Abaqus. The temperature field of the simulations and boundary heat flux results were then compared to the measurement data and the heat flux constraints. Figure 6.9 presents the results of this comparison. As one can see, the simulations were feasible, i.e. within the heat flux constraints, and the temperature difference is in a well acceptable error margin. One can then conclude that linear interpolation is a suitable method for the rated power curve of the engine.

The next part of the validation was to analyze an increase and decrease of power output to the engine speed rated ones.

Two assumed engine load cases were used for this purpose:

- 117 kW at 2250 RPM.
- 153 kW at 3375 RPM.

The load cases were chosen to differ greatly from each other as the feasibility of the liner interpolation method would then be easier to verify. Figure 6.16 presents the heat flux distribution of the load cases as this is the only way to verify if the simulations are feasible as no measurement data for these load cases are available. The figure shows that the heat fluxes are within the set constrained heat flux guidelines. A conclusion is thus that the interpolated model does seem feasible for assumed load cases, however, as stated previously, the temperature field is unable to be verified and therefore has an uncertainty to it.

To discuss further improvements of the model, the authors of this thesis want to make clear, that the stated simplifications, assumptions and uncertainties are necessary to be improved in order to increase the accuracy of the model. The neglected loads as friction and radiation needs to be implemented. The property changes of the materials due to thermal load needs to be included. The cooling gallery, undercrown and top load need to have further improved CFD analyses. The GT-Power simulations are directly responsible for the accuracy of this model and as such, further improvements of the GT-Power simulations will improve this model. Finally, the simplification of the ring dynamics needs to be properly modelled.

To summarize the constructed complete thermal analysis piston model:

- The solved temperature fields of the calibrated load cases are well in agreement to the measurement data.
- The heat flux proportions for the calibrated load cases follow the piston manufacturer guidelines.
- The interpolated based simulations, both for the rated engine output and the assumed ones, are feasible from a heat flux perspective and the rated engine load cases are also in agreement with the temperature measurement data.

A conclusion is therefore that this constructed thermal analysis model of the piston is well suitable to perform analyses with. The performed steps of constructing a simplified 2D axisymmetrical model, calibration of the

3D models, the linear interpolation for rated and assumed loads and finally verifying the data were all essential parts for the sucess of this thesis. The result in subsection 6.3.2 clearly shows that the constructed model corresponds well to the actual temperature field based on the measurement data and at the same time fulfills the heat flux input with respect to the GT-Power simulations and follows the piston manufacturer heat flux distribution guidelines.

8.6 Heat flux extraction and conversion

A combination of Python and MATLAB programs performs the heat flux extraction and the needed data conversion. A summary of how the programs performed the extraction and conversion was given in subsection 7.1. The following section will discuss and evaluate the developed method.

With the complete piston model constructed, the thermal interaction of the piston and the cylinder liner were to be analyzed. Given that Volvo Cars had applied the thermal load from the combustion in the cylinder chamber as a convective thermal load, another method of applying the piston thermal load was needed. The idea of using heat flux was attempted. After a discussion about extracting the element heat flux from the piston surfaces, converting it to element heat flux per unit area and mapping the element heat flux per unit area to the elements of the cylinder liner, it was concluded to be a suitable method.

The problem with this method was that Abaqus does not handle an element output which is based on heat flux per unit area. It does however support total node heat flux (RFLE) and element integration point heat flux per area (HFL). The authors of this thesis contacted Dassault Systèmes, the software developers of Abaqus, for insight of the stated problem. A recommendation of using HFL was given by Dassault Systèmes together with a HFL-extraction script. However, the results were imprecise to such an extent that the authors determined it to be an unsuitable method. This was due to the way the in-house mapping routine handled the HFL-extraction. The HFL-extraction was nodal based, while the mapping routine was element based. As such, improper DFLUX-mapping occurred since the information was incompatible.

The use of RFLE was attempted by the authors. The biggest problem was how to calculate the element area. Given the time limit of the thesis, the authors constructed a program which would calculate an approximation of the surface area of the second order element DC3D10. The approximation yielded excellent results for the vast majority of elements with a margin of error $< 1\%$, while some had a greater error of $< 10\%$.

With the approximated area of every element, the RFLE needed to be paired to the corresponding element nodes. The nodal RFLE values related to the element would then be summarized and divided by the approximated area. The result would thus be in the desired load format, i.e. heat flux per element area. However, as explained previously, the nodal RFLE value is the total nodal heat flux. As such simple summation of the nodal RFLE for the element would be false. What one must take into account is how many elements are connected to the node. The RFLE value must then be divided by the number of related elements.

While this method works fine for flat surfaces, the groove heat fluxes of the piston where needed to be converted to represent the actual piston rings heat fluxes. As the grooves where split into top, mid and bottom sections for the thermal analysis, the authors developed a method which would be equal to the piston ring heat flux.

The initial stage was done in the same manner as for the flat surfaces. The element heat flux per unit area was calculated for each section of the grooves. These heat fluxes were then manipulated in such a way that every 2.5° of the piston groove circumference, a summation of the top, mid and bottom groove heat fluxes per unit area was to describe the piston ring heat flux per unit area. This was performed for all piston ring grooves. The piston ring heat flux per unit area was then moved to a radial position which was equal to inner cylinder liner radius.

Figures 7.4, 7.5, 7.6 and 7.7 shows the results of the discussed methods.

The most obvious weakness of this method is the approximation of the area. This directly effects mag-

nitude of the calculated element heat flux per unit area. Another problem that could possibly arise is the division of the RFLE. If one has a fine mesh, an equal division is suitable to use. For a rougher mesh, one must determine the proportions of how much each element contribute to the connected nodal heat flux. As the authors used a fine element mesh, an equal split was feasible to use.

To make the groove heat flux mappable to the cylinder surface, it was necessary to somehow express it as a single value which represents the top, mid and bottom ring groove surfaces heat fluxes per unit area. One can imagine that the explained method in subsection 7.1 constructs a imaginary piston ring element and calculates the averaged heat flux per unit area for this element by taking into account the groove surfaces.

In Figure 7.4 to 7.7, one can observe that near the oil groove cavity there is a higher element heat flux per unit area than the rest of the oil groove. The section of the groove had a complex element setup compared to the rest of the piston grooves due to its geometry. Thus, a number of reasons contributed the increased element heat flux per unit at these points.

- The element face area approximation method.
- The summation of the element heat flux per unit area to represent the oil ring resulted in high values.
- The cavities are not modelled separately, i.e. they have the same HTC as the rest of the oil groove.

As explained previously, the element area is approximated. A comparison between the approximated element area and actual element area was performed. The approximation had a certain error to it, but it was deemed as not the biggest contributing factor to the high heat flux.

The summation of the heat flux per unit area was explained in subsection 7.1. This method, coupled with the complex geometry of the cavity, results in that many elements were summed together. Therefore a high heat flux per unit area occurs at this point, as many elements are summed and condensed to a single point, which is supposed to represent the oil ring. This is an obvious flaw in the method. However, one must take into account that the cavities were not modelled separately, i.e. they were modelled to have the same thermal properties as the rest of the oil groove surfaces. In reality, this is not true. Not only do they not have any direct contact with the oil ring, they have a far different geometry compared to the rest of the groove. If one were to handle the cavities as separate thermal loads, a hypothesis concluded by the authors is that a significantly lower heat flux at these points seems to be of very high possibility. As such, the element heat flux per unit area of the cavities would have been of significantly lower magnitude.

The fact that the cavities are such a small portion of the total outer piston surface area, the results in Figures 7.4 to 7.7 can be considered as an acceptable error in the developed method. An investigation of the possible stated error factors is recommended for future work.

8.7 Mapping of heat flux onto the cylinder liner

Unfortunately, the mapping procedure described in subsection 7.3 was unable to be properly evaluated as performing a thermal analysis of the complete engine with the piston thermal load was out of scope of this Master's thesis work. The validation of the element heat flux extraction and mapping was therefore simplified in its extent by, as stated in subsection 7.1, by removing the convective loads on the piston surfaces facing the cylinder liner and applying the extracted and converted element heat flux load on the same piston surfaces. This procedure would validate if the convected element heat fluxes truly represented the corresponding piston surfaces heat flux by analyzing the piston temperature field.

The results from the validations were presented in subsection 7.7 and most significantly in Figure 7.15 where the reference temperature difference and the piston boundary heat flux distribution was compared for the validation results to the original calibration results. As seen in Figure 7.15, the correspondence between the two analysis results is nearly identical for both the reference temperature difference and the energy distribution. The lower reference temperature difference and RMS-value obtained for the validation analysis result is simply a lucky coincidence and the results presented in Figure 7.15 should be considered as a sign of good correspondence with the original thermal analysis model rather than a method of obtaining better results in terms of lower RMS-value.

The issue with the increased element heat flux per unit at oil cavities can be observed in the mapped cylinder liner Figures 7.8 to 7.11. Possible improvements of the cavities modelling were explained in section 8.6 which in turn would improve the mapped cylinder liner thermal load.

What should be noted is that piston tilting has not been taken into consideration, which ultimately affect the rate of heat flux transferred from the piston to the cylinder liner as the contact between the piston and the cylinder liner may not be as uniform as assumed.

As the method of extracting the piston element heat flux per area unit and utilizing mapping shows such good results, the time averaged heat flux mapped to the cylinder liner can be considered to be of reasonable magnitude and a suitable method to use for a complete engine thermal analysis.

8.7.1 Thermal analysis of cylinder liner

The objective of this Master's thesis was not to preform a thermal analysis of a complete engine. As such, the purpose of the result in subsection 7.8 is purely a demonstration of how the piston heat flux affects the cylinder liner. However, a conclusion based on Figure 7.16 and Figures 7.8 to 7.11 is that the mapped piston heat flux load was properly applied.

References

[1] *Abaqus 6.14 Theory Guide*. Version 6.14. Dassault Systèmes, 2014.

[2] T. Abrahamsson. *Calibration and Validation of Structural Dynamics Models*. Göteborg: Chalmers University of Technology, 2012.

[3] A. C. Alkidas et al. Laboratory Experiments on Oil-Jet Cooling of Internal Combustion Engine Pistons: Area-Average Correlation of Oil-Jet Impingement Heat Transfer. English. *Journal of Energy Engineering* **141**.2 (2015; 2014), C4014003.

[4] W. J. D. Annand and T. H. Ma. Instantaneous heat transfer rates to the cylinder head surface of a small compression ignition engine. English. *ARCHIVE: Proceedings of the Institution of Mechanical Engineers 1847-1982 (vols 1-196)* **185**.1970 (1970), 976–988.

[5] M. Bovo. *Principles of Heat Transfer in Internal Combustion Engines from a Modeling Standpoint*. Chalmers University of Technology, 2014. ISBN: 978-91-7385-992-9.

[6] J. E. Bush and A. L. London. "Design Data for "Cocktail Shaker" Cooled Pistons and Valves". *SAE Technical Paper*. SAE International, Feb. 1965.

[7] V. Esfahanian, A. Javaheri, and M. Ghaffarpour. Thermal analysis of an SI engine piston using different combustion boundary condition treatments. *Applied Thermal Engineering* **26**.2-3 (2006), 277 –287. ISSN: 1359-4311.

[8] C. C. J. French. "Piston Cooling". *SAE Technical Paper*. SAE International, Feb. 1972.

[9] H. Fridriksson et al. "CFD Investigation of Heat Transfer in a Diesel Engine with Diesel and PPC Combustion Modes". *SAE Technical Paper*. SAE International, Aug. 2011. DOI: 10.4271/2011-01-1838.

[10] M. GmbH(Ed). *Pistons and engine testing*. Wiesbaden: Vieweg+Teubner, 2011. ISBN: 978-3-8348-1982-6.

[11] T. He, X. Lu, and Y. Guo. Analysis of the heat transfer coefficients on the top of a marine diesel piston using the inverse heat conduction method. **291-294** (2011), 1657–1661.

[12] G. F. Hohenberg. "Advanced Approaches for Heat Transfer Calculations". *SAE Technical Paper*. SAE International, Feb. 1979.

[13] F. P. Incropera. *Principles of heat and mass transfer*. Hoboken, NJ: Wiley, 2012. ISBN: 9780470646151; 0470646152.

[14] S. W. J. and T. D. C. "Spatial Variation of Heat Transfer to Pistons and Liners of Some Medium Speed Diesel Engines". *Proceedings of the Institution of Mechanical Engineers*. Vol. 185. Sage Journals, 1970, pp. 203–218.

[15] J. C. Lagarias et al. Convergence Properties of the Nelder–Mead Simplex Method in Low Dimensions. *SIAM Journal on Optimization* **9**.1 (1998), 112–36.

[16] C.-H. Li. "Piston Thermal Deformation and Friction Considerations". *SAE Technical Paper*. SAE International, Feb. 1982.

[17] X. Lu et al. Thermal analysis on piston of marine diesel engine. *Applied Thermal Engineering* **50**.1 (2013), 168–176. ISSN: 1359-4311.

[18] D. W. Marquardt. An Algorithm for Least-Squares Estimation of Nonlinear Parameters. *Journal of the Society for Industrial and Applied Mathematics* **11**.2 (1963), pp. 431–441. ISSN: 03684245.

[19] *MATLAB manual. Fminearch*. Version R2015a. Mathworks, 2015. URL: `http://se.mathworks.com/help/matlab/ref/fminsearch.html`.

[20] N. Morris et al. Tribology of piston compression ring conjunction under transient thermal mixed regime of lubrication. *Tribology International* **59**.0 (2013), 248 –258. ISSN: 0301-679X.

[21] N. S. Ottosen and H. Petersson. *Introduction to the finite element method*. New York: Prentice Hall, 1992. ISBN: 0134738772; 9780134738772.

[22] J. Pan, R. Nigro, and E. Matsuo. "3-D Modeling of Heat Transfer in Diesel Engine Piston Cooling Galleries". *SAE Technical Paper*. SAE International, Apr. 2005.

[23] K. Runesson, F. Larsson, and K. Carlsson. *FEM basics chap 4, pp-slides*. Chalmers, 2014.

[24] R. E. Stanley. *Piston ring assembly friction: A simplified model*. English. 1998.

[25] A. Turco. *New Constraints Handling in Simplex*. Tech. rep. 2011-002. Padriciano 99, Trieste, ITALY: Esteco, May 2011.

[26] G. Woschni. "A Universally Applicable Equation for the Instantaneous Heat Transfer Coefficient in the Internal Combustion Engine". *SAE Technical Paper*. SAE International, Feb. 1967.

[27] G. Woschni and J. Fieger. "DETERMINATION OF LOCAL HEAT TRANSFER COEFFICIENTS AT THE PISTON OF A HIGH SPEED DIESEL ENGINE BY EVALUATION OF MEASURED TEMPERATURE DISTRIBUTION". *SAE Technical Paper*. SAE International, Feb. 1979. DOI: `10.4271/790834`.

[28] Y. Yi et al. "CFD Modeling of the Multiphase Flow and Heat Transfer for Piston Gallery Cooling System". *SAE Technical Paper*. SAE International, Oct. 2007.

A Results from parameter calibrations

This appendix section is devoted for the results from the parameter calibrations performed throughout this Master's thesis and that are not presented in the results section.

A.1 Results from 2D axisymmetrical parameter calibrations

The results from the 2D axisymmetrical parameter calibrations performed in MATLAB are shown in this section. The results represents the engine load cases that were not included in the results section 4.3.

A.1.1 Engine load case: 100 kW at 2000 RPM

The 2D axisymmetrical piston structure temperature field is illustrated in Figure A.1 and the reference temperature differences are presented in Figure A.2. Figure A.3 shows the heat flux distribution over the piston boundaries as well as the corresponding total heat flux quantity. The calibrated heat transfer coefficients of the piston ring assembly and the oil cooling gallery are presented in Figure A.4. Figures A.5, A.6 and A.7 shows the HTC- and temperature distribution on the piston top surface as well as the piston undercrown HTC distribution.

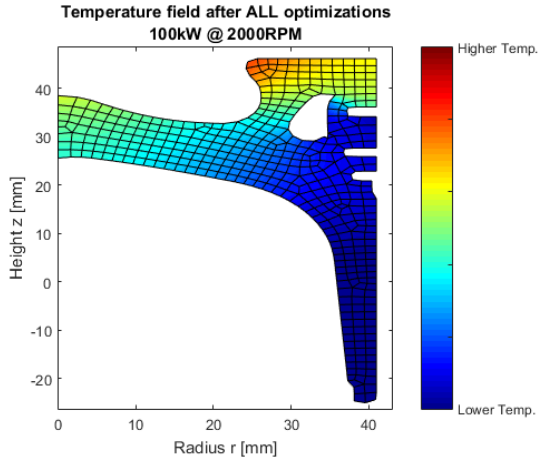

Figure A.1: 2D axisymmetrical temperature field.

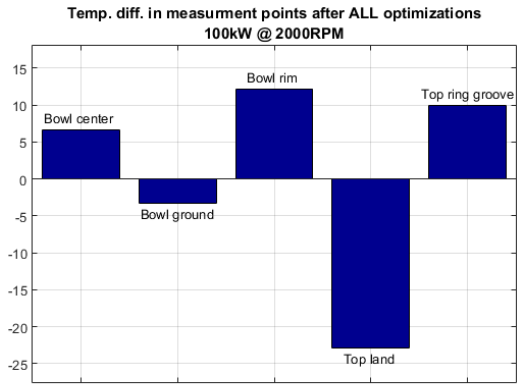

Figure A.2: Temperature difference in measurement points.

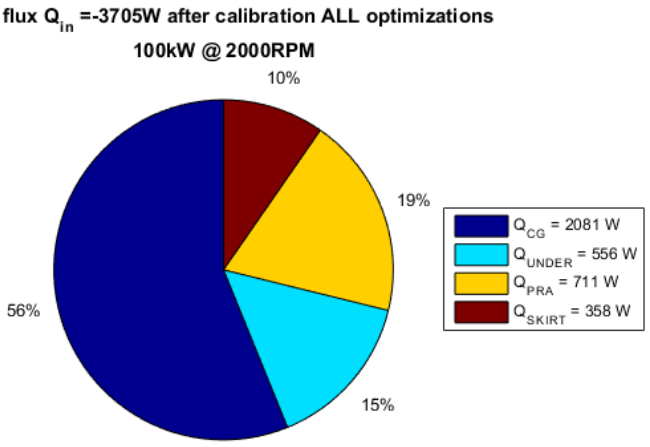

Figure A.3: Boundary heat flux distribution.

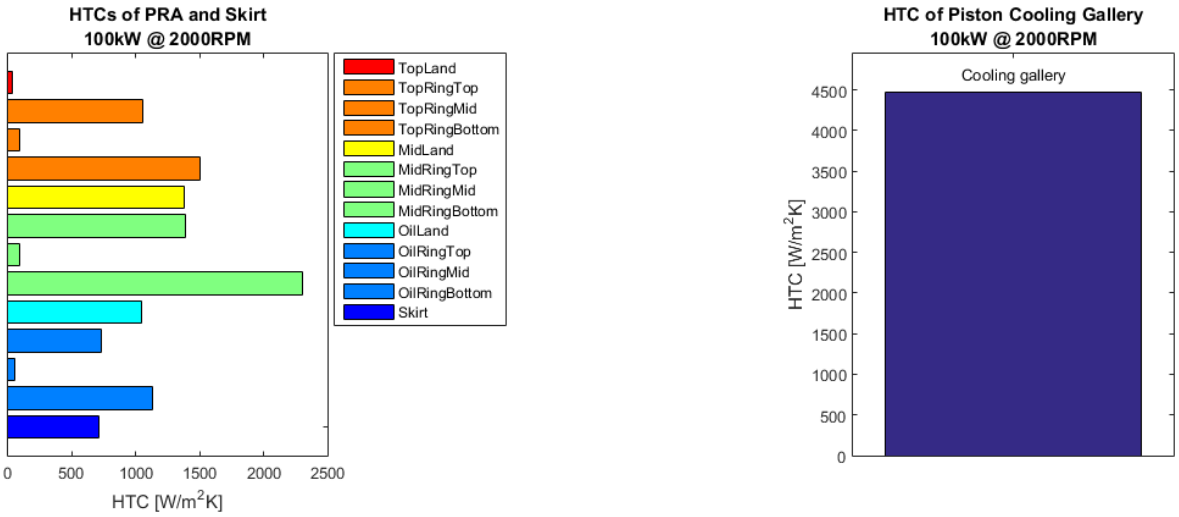

Figure A.4: Calibrated values of the HTCs in the piston ring assembly, skirt and cooling channel.

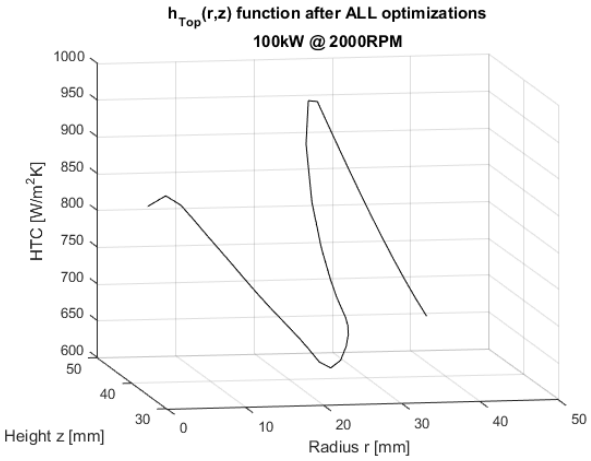

Figure A.5: Piston top surface HTC distribution.

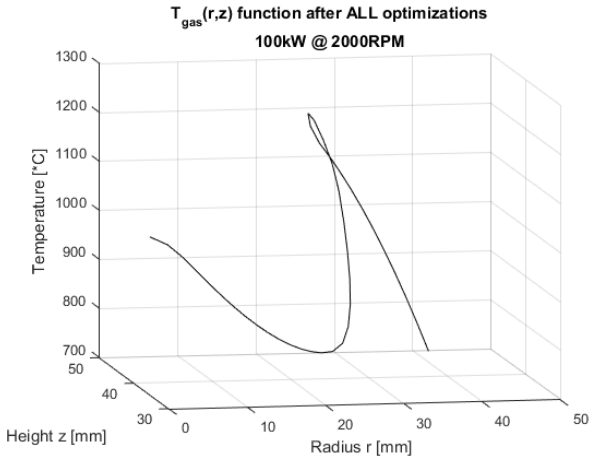

Figure A.6: Piston top surface temperature distribution.

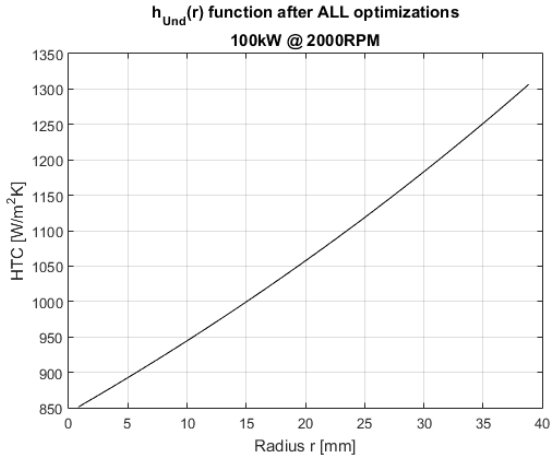

Figure A.7: Piston undercrown HTC distribution.

A.1.2 Engine load case: 135 kW at 3000 RPM

The 2D axisymmetrical piston structure temperature field is illustrated in Figure A.8 and the reference temperature differences are presented in Figure A.9. Figure A.10 shows the heat flux distribution over the piston boundaries as well as the corresponding total heat flux quantity. The calibrated heat transfer coefficients of the piston ring assembly and the oil cooling gallery are presented in Figure A.11. Figures A.12, A.13 and A.14 shows the HTC- and temperature distribution on the piston top surface as well as the piston undercrown HTC distribution.

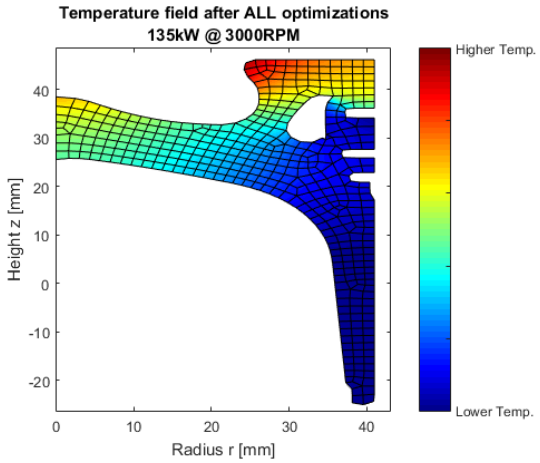

Figure A.8: 2D axisymmetrical temperature field.

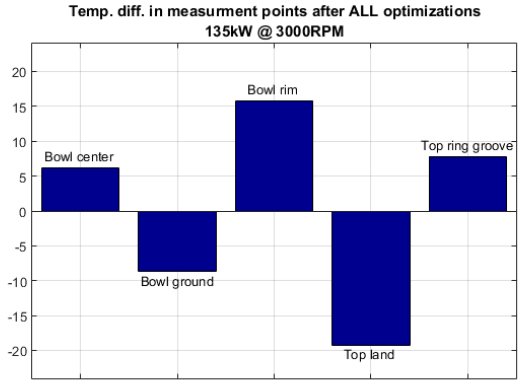

Figure A.9: Temperature difference in measurement points.

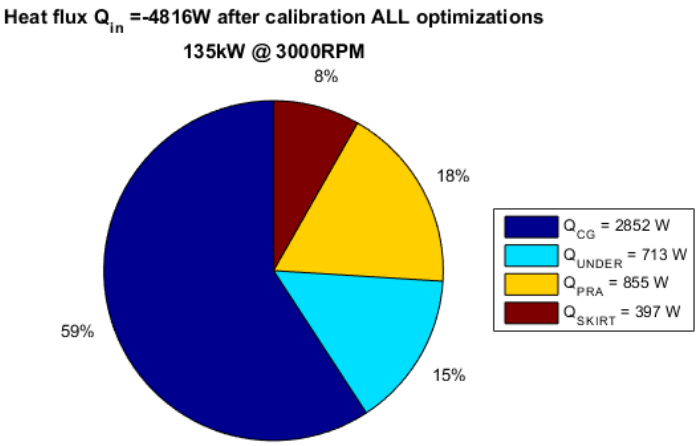

Figure A.10: Boundary heat flux distribution.

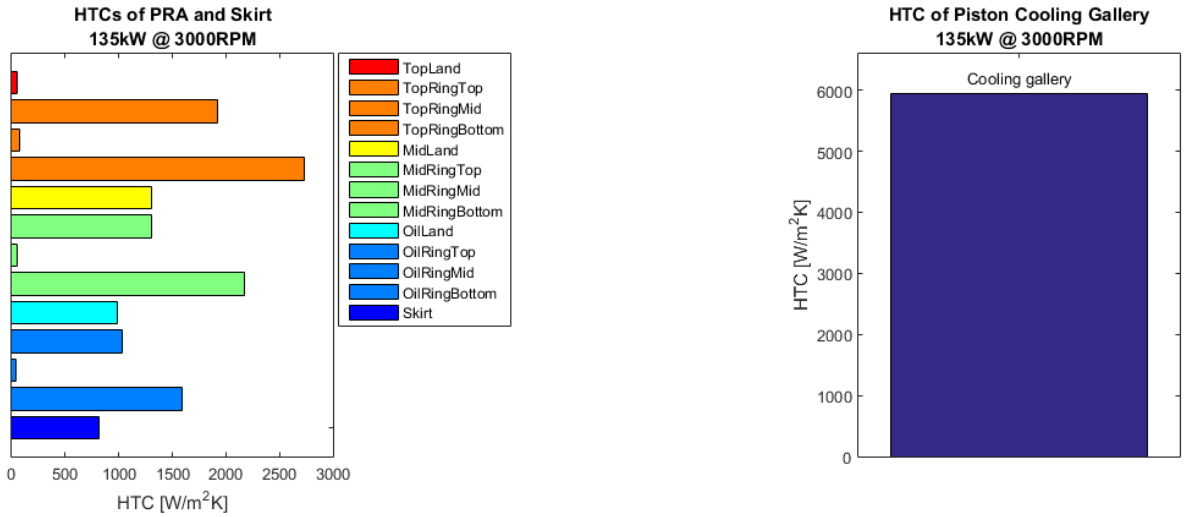

Figure A.11: Calibrated values of the HTCs in the piston ring assembly, skirt and cooling channel.

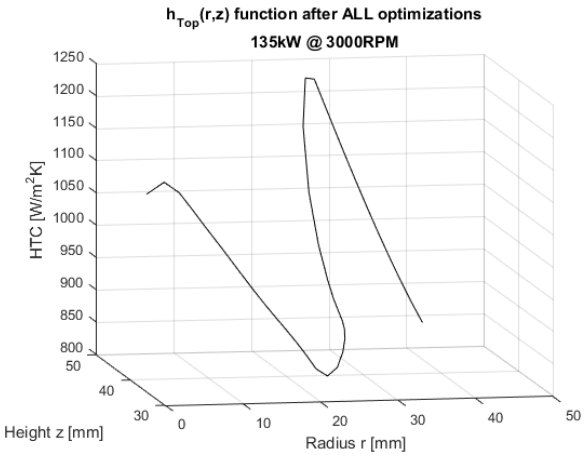

Figure A.12: Piston top surface HTC distribution.

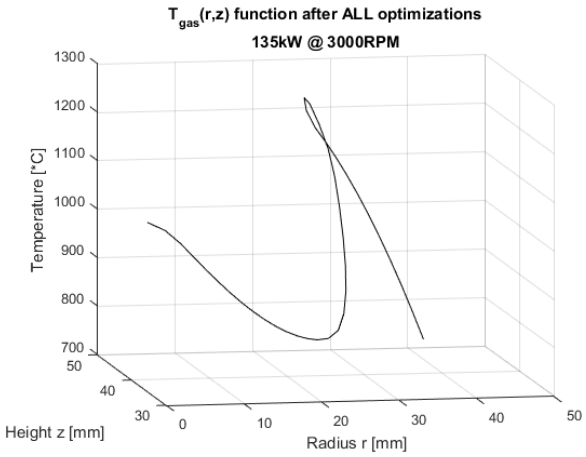

Figure A.13: Piston top surface temperature distribution.

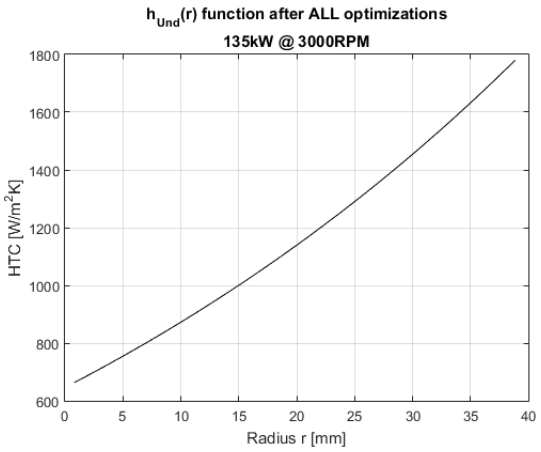

Figure A.14: Piston undercrown HTC distribution.

A.2 Results from 3D parameter calibration with rated engine loads

Presented in the following sections are the results from the 3D parameter calibrations for the engine load cases not shown in section 5.10. As the table consisting on the reference temperature differences and heat flux distribution are shown in section 5.10, only the piston structure temperature field will be presented here.

A.2.1 Engine load case: 100 kW at 2000 RPM

The temperature distribution in the piston structure after calibration for 100 kW at 2000 RPM is shown in Figures A.15 to A.17 with an isometric view, a top view and a cut view of the piston.

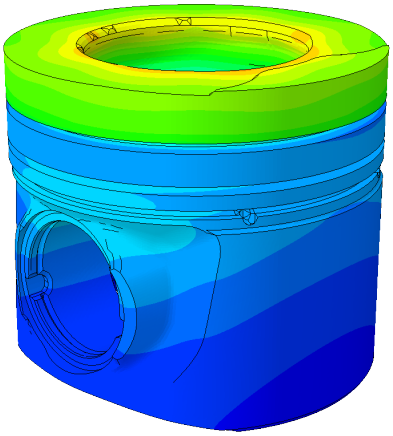

Figure A.15: Isometric view.

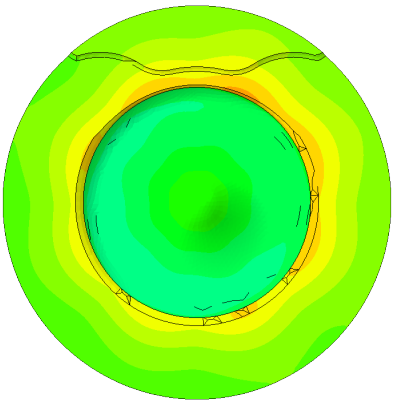

Figure A.16: Top view.

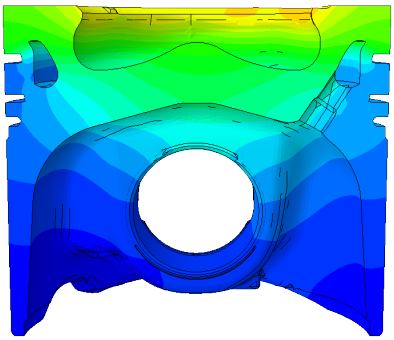

Figure A.17: View of ATS-TS cut section.

A.2.2 Engine load case: 135 kW at 3000 RPM

The temperature distribution in the piston structure after calibration for 135 kW at 3000 RPM is shown in Figures A.18 to A.20 with an isometric view, a top view and a cut view of the piston.

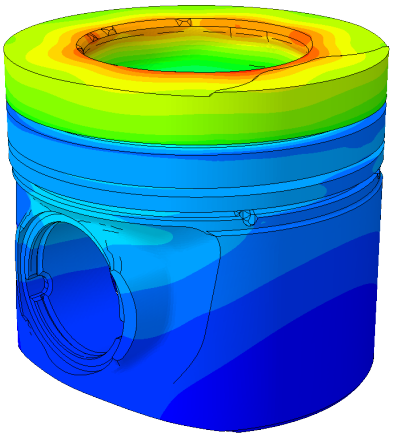

Figure A.18: Isometric view.

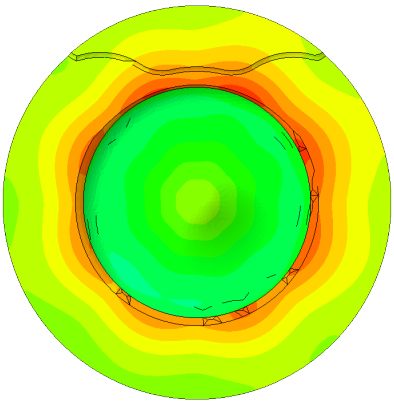

Figure A.19: Top view.

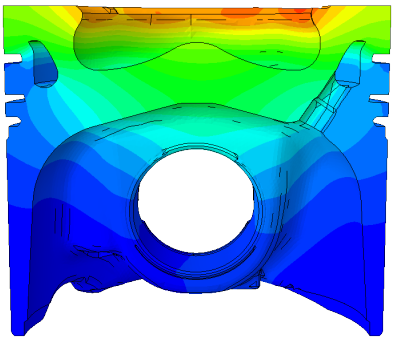

Figure A.20: View of ATS-TS cut section.

A.3 Results from 3D parameter calibrations with assumed engine loads

Presented in the following sections are the results from the 3D parameter calibrations for the engine load cases not shown in section 5.11. The results presented consists of contour plots of the piston structure temperature field and the heat flux distribution over the piston boundaries.

A.3.1 Engine load case: 90 kW at 2000 RPM

The temperature distribution in the piston structure after calibration for 90 kW at 2000 RPM is shown in Figures A.21 to A.23 with an isometric view, a top view and a cut view of the piston.

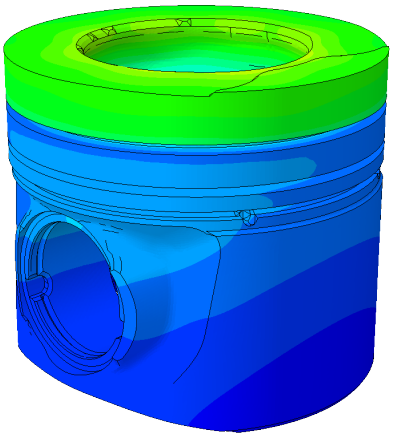

Figure A.21: Isometric view.

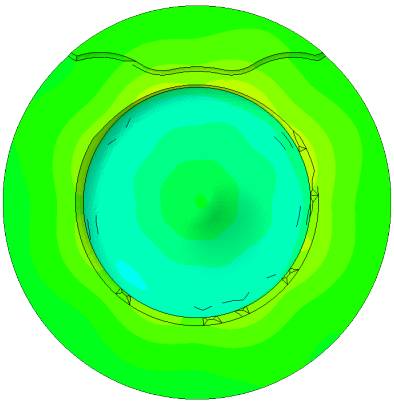

Figure A.22: Top view.

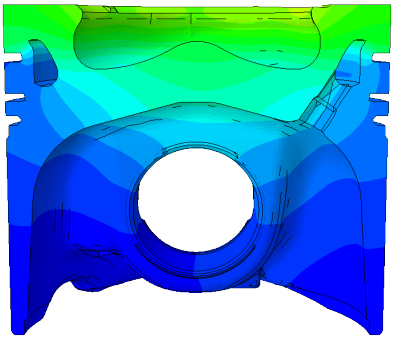

Figure A.23: View of ATS-TS cut section.

The heat flux distribution over the piston boundaries for the engine load case is presented in Figure A.24.

	90 kW | 2000 RPM
Heat Flux	
Heat input [W]	3234
Cooling gallery output [%]	56,86%
PRA output [%]	23,19%
Undercrown output [%]	12,57%
Skirt output [%]	5,66%
Pin boss output [%]	0,69%
Pin face output [%]	0,90%

Figure A.24: Heat flux distribution.

A.3.2 Engine load case: 110 kW at 2000 RPM

The temperature distribution in the piston structure after calibration for 110 kW at 2000 RPM is shown in Figures A.25 to A.27 with an isometric view, a top view and a cut view of the piston.

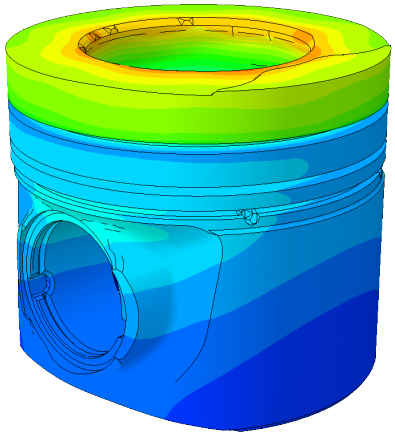

Figure A.25: Isometric view.

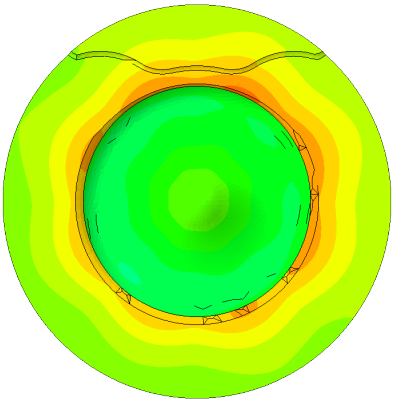

Figure A.26: Top view.

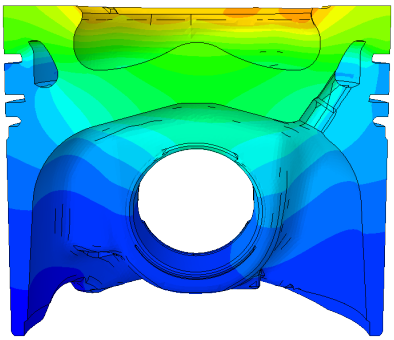

Figure A.27: View of ATS-TS cut section.

The heat flux distribution over the piston boundaries for the engine load case is presented in Figure A.28.

	110 kW | 2000 RPM
Heat Flux	
Heat input [W]	3945
Cooling gallery output [%]	58,10%
PRA output [%]	24,11%
Undercrown output [%]	8,90%
Skirt output [%]	6,11%
Pin boss output [%]	1,71%
Pin face output [%]	1,00%

Figure A.28: Heat flux distribution.

A.3.3 Engine load case: 125 kW at 3000 RPM

The temperature distribution in the piston structure after calibration for 125 kW at 3000 RPM is shown in Figures A.29 to A.31 with an isometric view, a top view and a cut view of the piston.

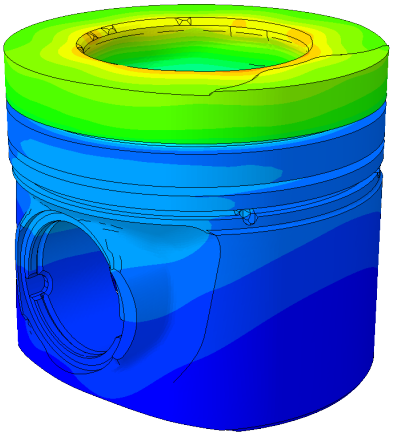

Figure A.29: Isometric view.

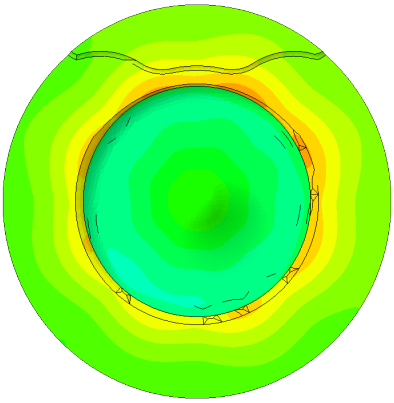

Figure A.30: Top view.

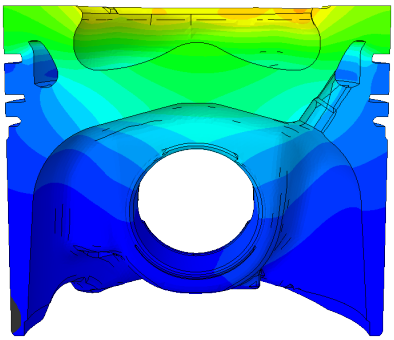

Figure A.31: View of ATS-TS cut section.

The heat flux distribution over the piston boundaries for the engine load case is presented in Figure A.32.

	125 kW | 3000 RPM
Heat Flux	
Heat input [W]	4343
Cooling gallery output [%]	58,83%
PRA output [%]	21,89%
Undercrown output [%]	9,24%
Skirt output [%]	7,40%
Pin boss output [%]	0,76%
Pin face output [%]	1,77%

Figure A.32: Heat flux distribution.

A.3.4 Engine load case: 145 kW at 3000 RPM

The temperature distribution in the piston structure after calibration for 145 kW at 3000 RPM is shown in Figures A.33 to A.35 with an isometric view, a top view and a cut view of the piston.

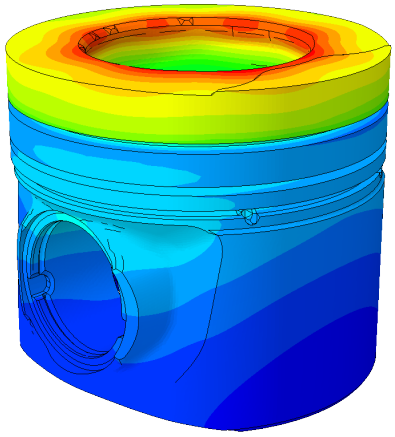

Figure A.33: Isometric view.

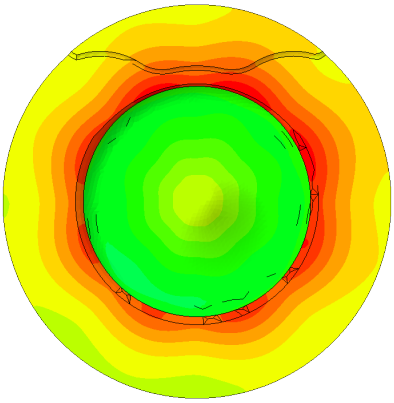

Figure A.34: Top view.

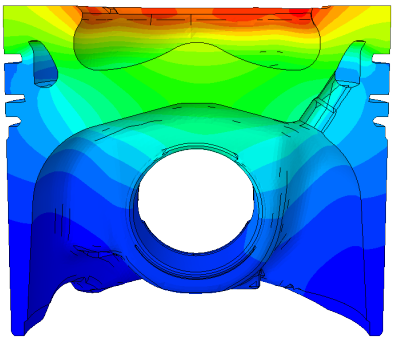

Figure A.35: View of ATS-TS cut section.

The heat flux distribution over the piston boundaries for the engine load case is presented in Figure A.36.

	145 kW | 3000 RPM
Heat Flux	
Heat input [W]	5060
Cooling gallery output [%]	59,96%
PRA output [%]	22,71%
Undercrown output [%]	5,02%
Skirt output [%]	8,28%
Pin boss output [%]	1,90%
Pin face output [%]	2,04%

Figure A.36: Heat flux distribution.

A.4 Results from 3D CFD parameter calibrations

As stated in section 5.9, the 3D parameter calibration on the thermal model with mapped CFD top load yielded slightly higher RMS-value than in the case of the thermal model with the top load expressed as a sinusoidal cubic polynomial function. Consequently, the authors decided to further evaluate the results from the latter thermal analysis model. This section presents the result of the 3D parameter calibration for the thermal analysis model with the piston top load as mapped CFD-data.

The temperature distribution in the piston structure after calibration for 100 kW at 2000 RPM is shown in Figures A.37 to A.39 with an isometric view, a top view and a cut view of the piston.

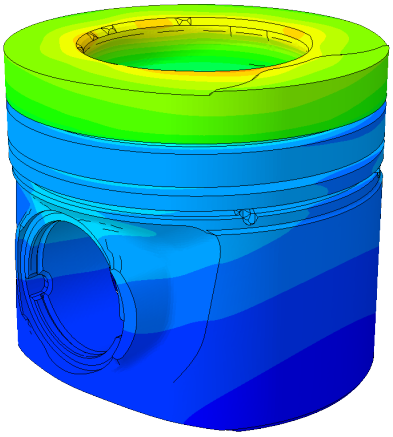

Figure A.37: Isometric view.

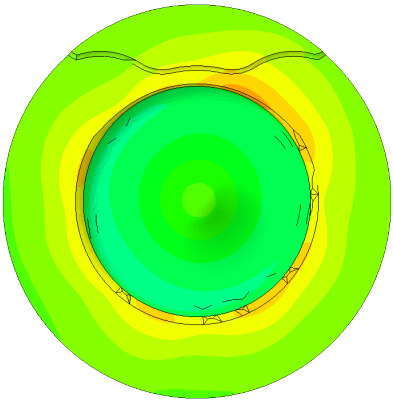

Figure A.38: Top view.

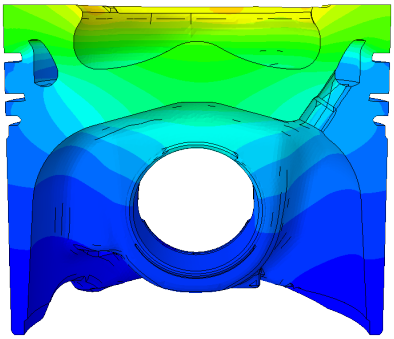

Figure A.39: View of ATS-TS cut section.

The temperature distribution in the piston structure after calibration for 135 kW at 3000 RPM is shown in Figures A.40 to A.42 with an isometric view, a top view and a cut view of the piston.

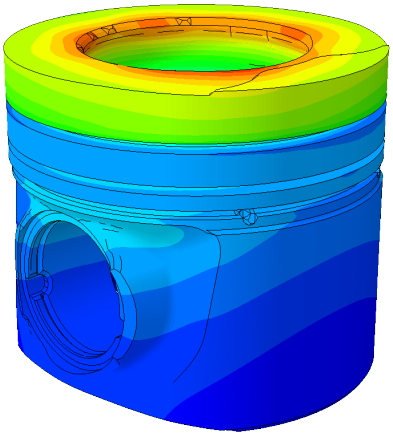

Figure A.40: Isometric view.

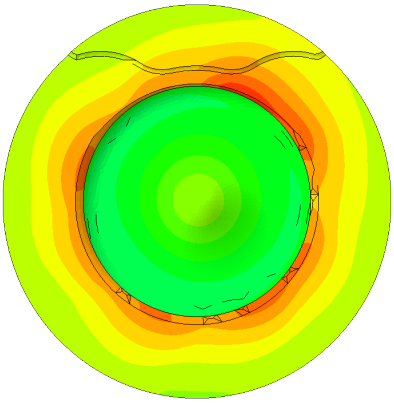

Figure A.41: Top view.

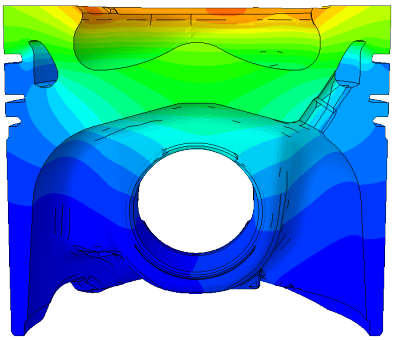

Figure A.42: View of ATS-TS cut section.

The temperature distribution in the piston structure after calibration for 170 kW at 4000 RPM is shown in Figures A.43 to A.45 with an isometric view, a top view and a cut view of the piston.

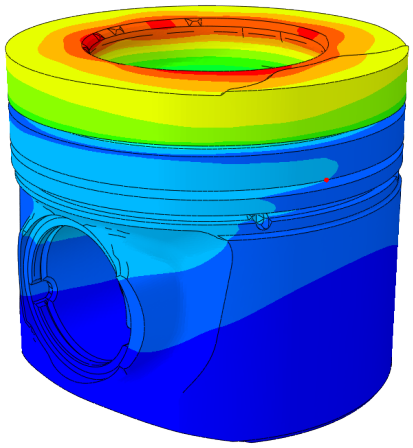

Figure A.43: Isometric view.

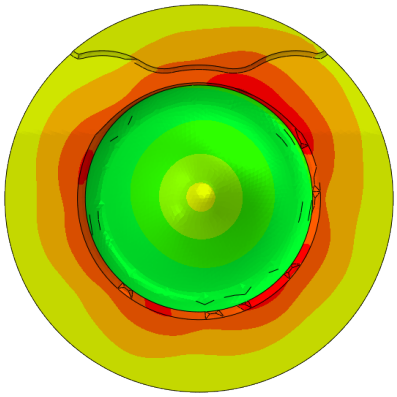

Figure A.44: Top view.

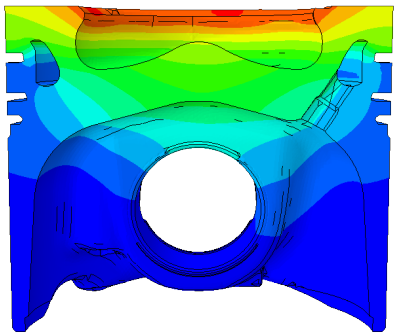

Figure A.45: View of ATS-TS cut section.

Presented in figure A.46 are the reference temperature differences and the heat flux distribution over the piston boundaries for the engine load cases presented in this section.

	100 kW | 2000 RPM	135 kW | 3000 RPM	170 kW | 4000 RPM
Reference temperature difference			
A1 Bowl Center :	9,4	6,8	12,2
A2 Bowl Rim TS :	9,0	3,4	3,3
A3 Bowl Rim ATS :	-2,0	-3,8	-6,7
A4 Bowl Rim FS :	-3,0	-2,2	1,5
A5 Bowl Ground ATS :	3,8	-0,9	-2,4
A6 Bowl Rim RS :	10,9	11,8	12,5
Piston Bowl mean error	4,7	2,5	3,4
B1 Groove 1 ATS :	5,0	9,9	12,9
B2 Groove 1 TS :	16,5	12,9	14,1
B3 Groove 1 FS :	-6,4	5,1	4,9
Piston Groove mean error	5,0	9,3	10,6
C1 Pin Boss RS :	2,4	0,6	-3,2
C2 Support FS :	-2,3	-1,4	-1,1
C3 Pin Boss FS :	2,2	-2,2	-2,7
Piston Pin Boss mean error	0,8	-1,0	-2,3
D1 Top Land FS :	-22,2	-13,1	-11,5
D2 Top Land ATS :	-11,5	-11,2	-13,2
Piston Top Land mean error	-16,9	-12,2	-12,4
Reference temperature RMS error			
RMS error	9,63	7,61	10,04
Heat Flux			
Heat input [W]	4050	4955	5372
Cooling gallery output [%]	57,53%	59,92%	59,94%
PRA output [%]	21,37%	20,42%	20,12%
Undercrown output [%]	10,50%	11,08%	10,41%
Skirt output [%]	5,06%	5,74%	6,06%
Pin boss output [%]	1,35%	1,54%	1,29%
Pin face output [%]	4,20%	1,27%	2,19%

Figure A.46: Reference temperature difference and piston boundary heat flux distribution.

A.5 Interpolated heat transfer coefficients

As stated in section 6.1, the interpolated HTC matrices for the remaining piston boundaries are illustrated in this section. The HTC matrices are shown in Figure A.47 to A.64

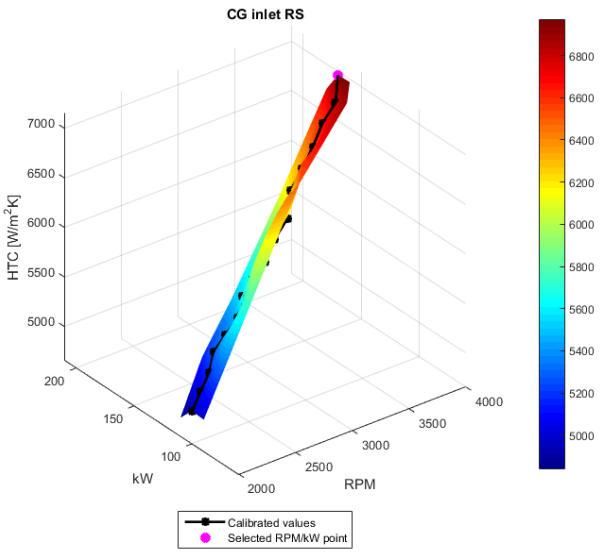

Figure A.47: Cooling gallery inlet.

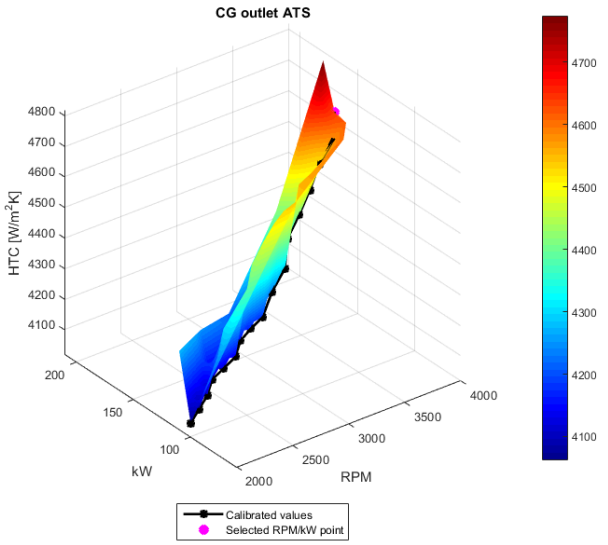

Figure A.48: Cooling gallery outlet.

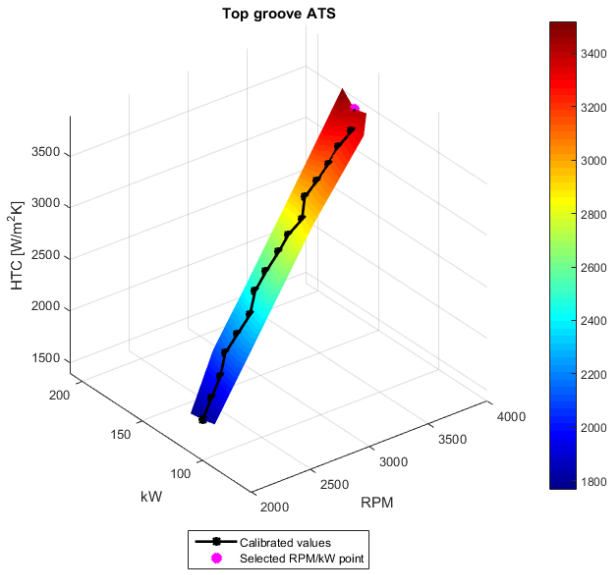

Figure A.49: Top groove ATS.

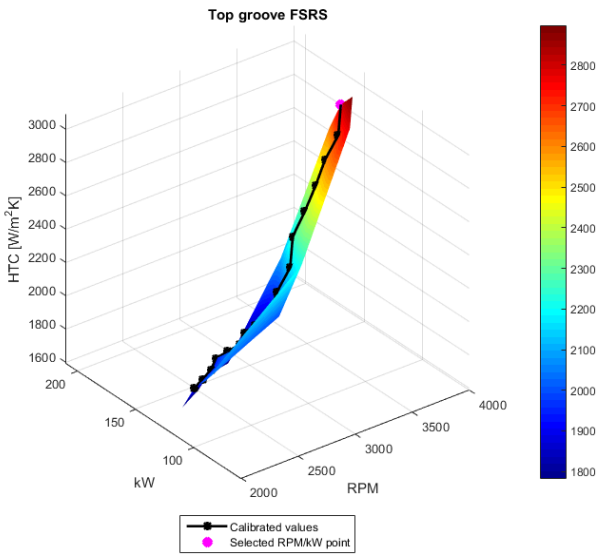

Figure A.50: Top groove FS/RS.

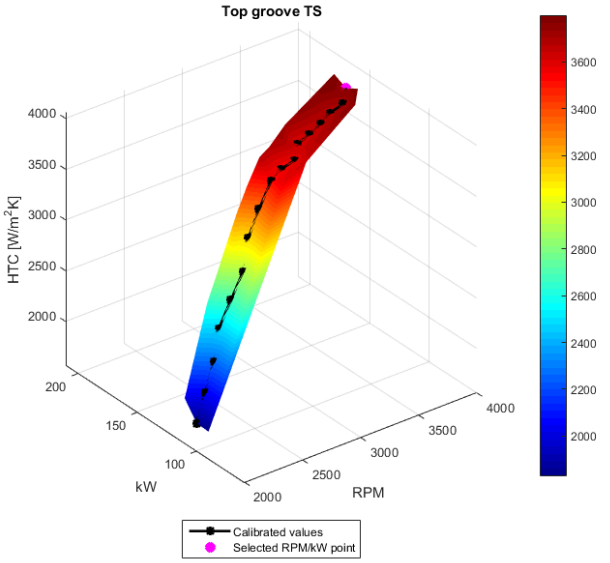

Figure A.51: Top groove TS.

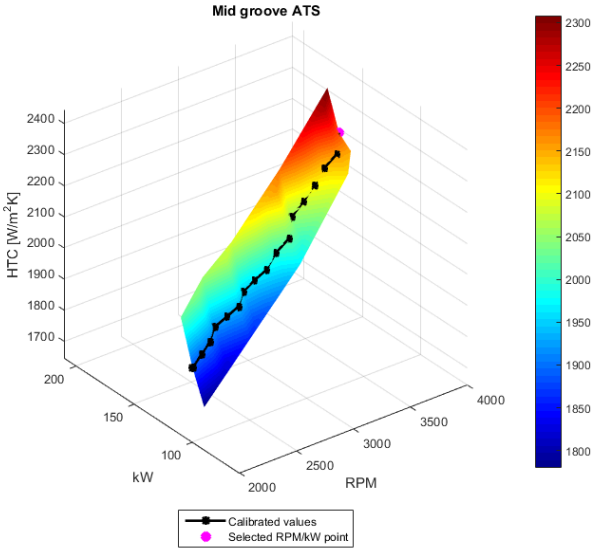

Figure A.52: Mid groove ATS.

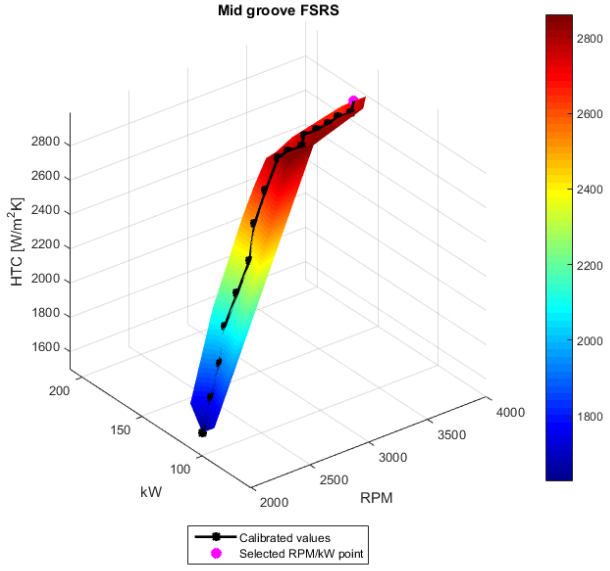

Figure A.53: Mid groove FS/RS

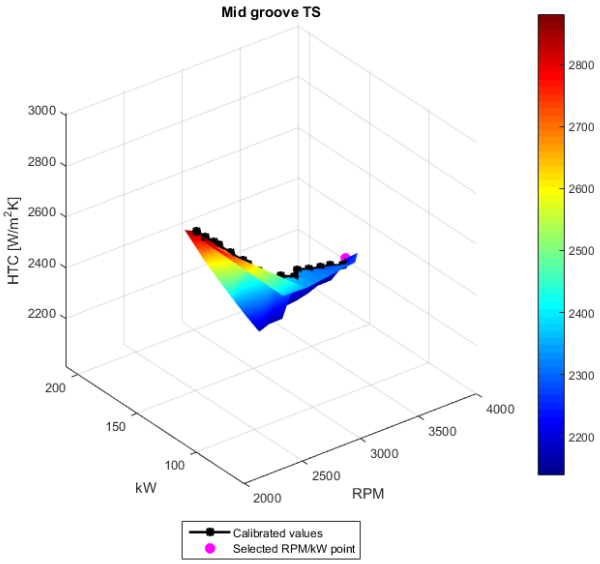

Figure A.54: Mid groove TS.

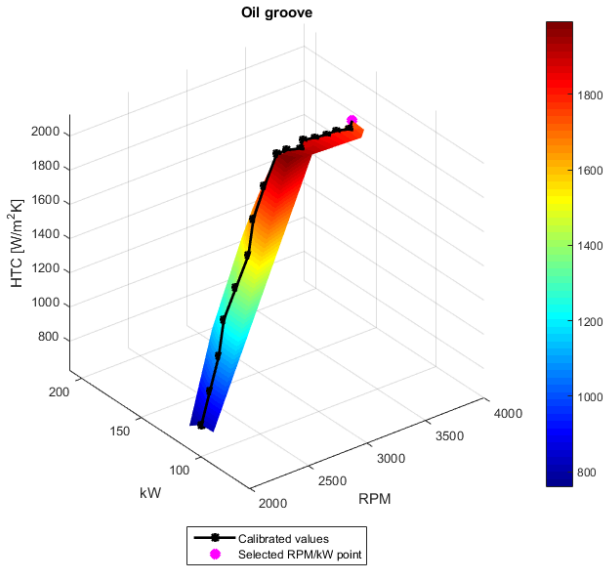

Figure A.55: Oil groove.

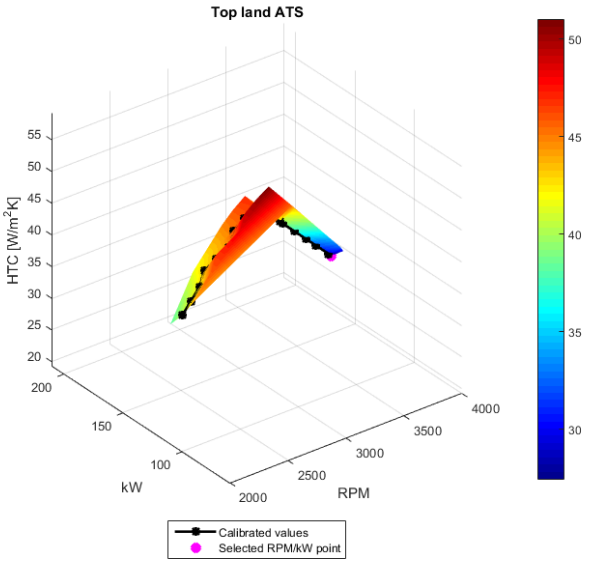

Figure A.56: Top land ATS.

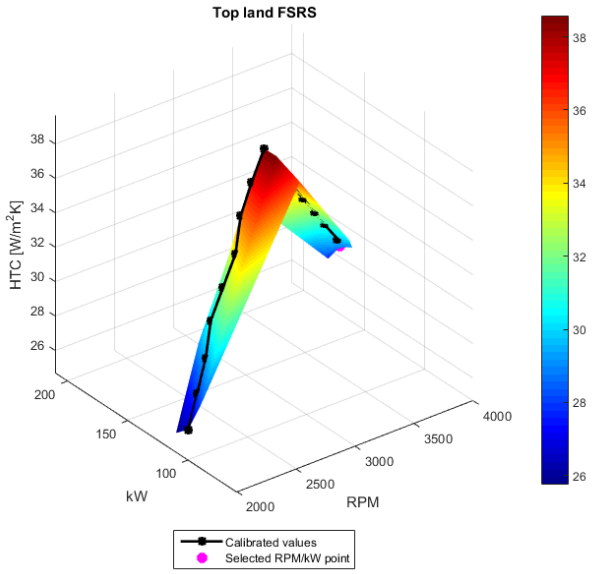

Figure A.57: Top land FS/RS.

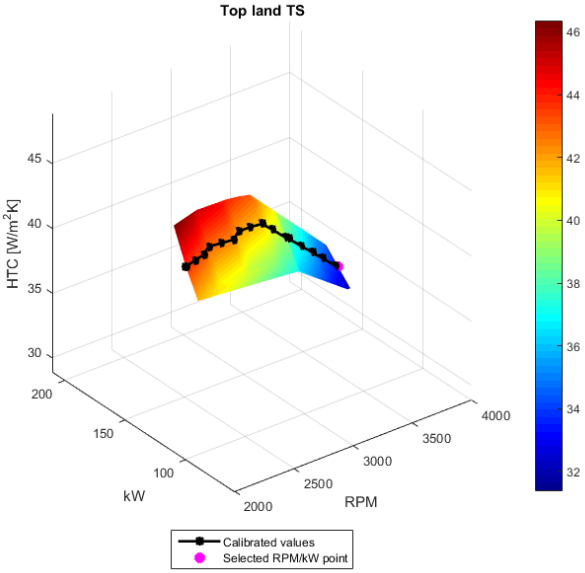

Figure A.58: Top land TS.

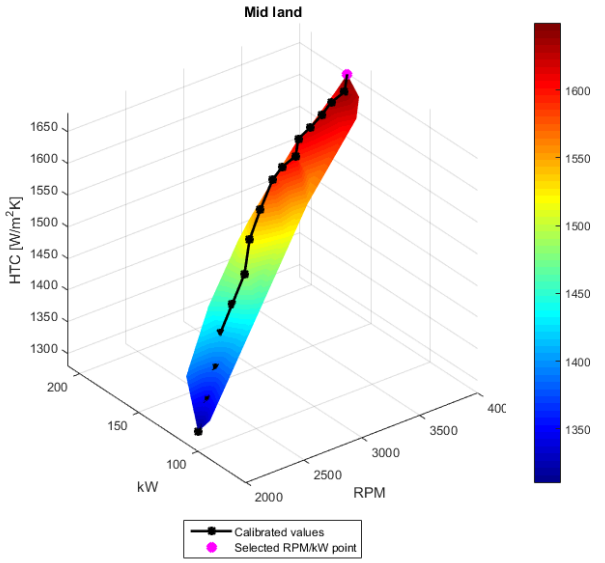

Figure A.59: Mid land.

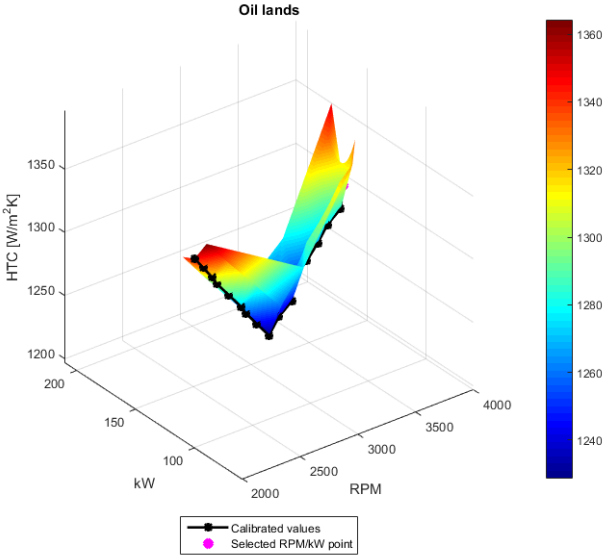

Figure A.60: Oil land.

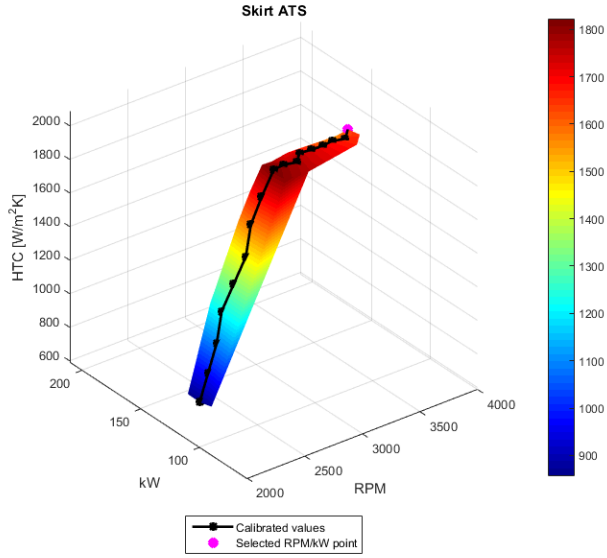

Figure A.61: Skirt ATS.

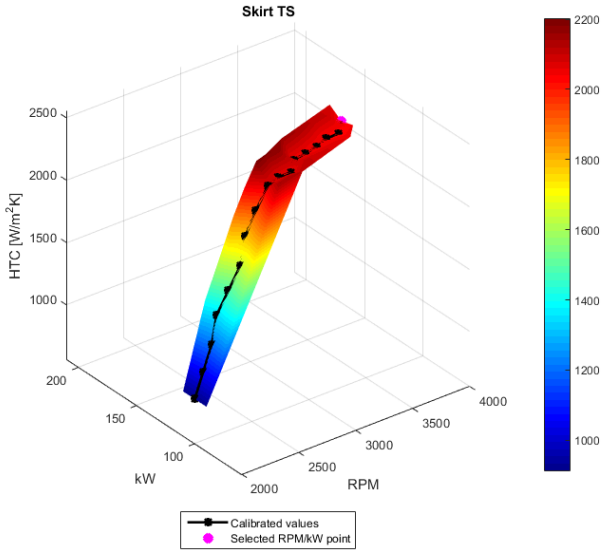

Figure A.62: Skirt TS.

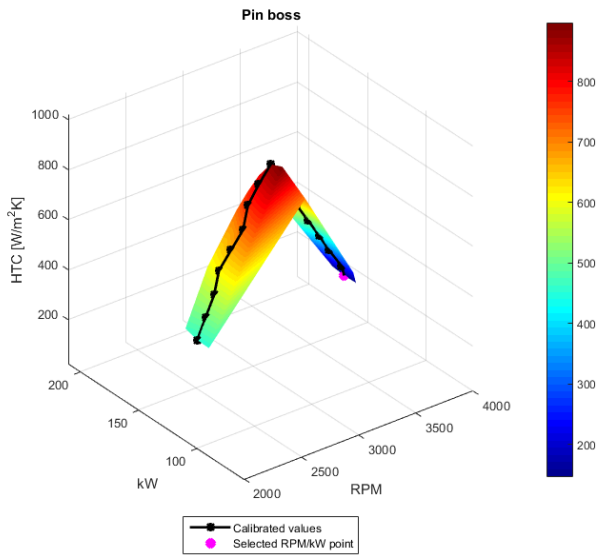

Figure A.63: Pin boss.

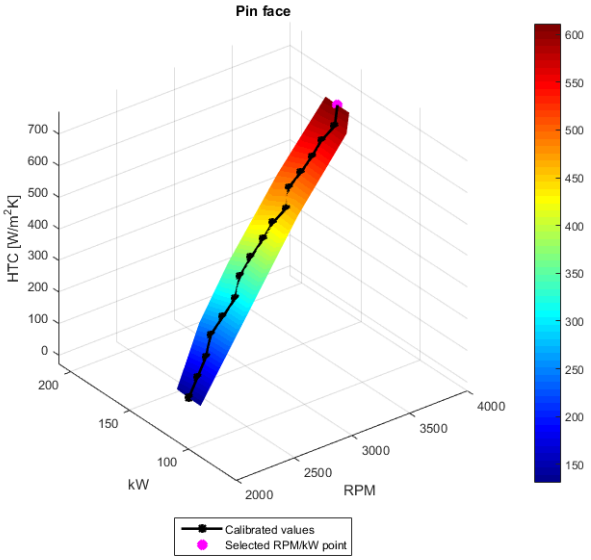

Figure A.64: Pin face.

The HTC and temperature distributions for the piston top load are presented in Figure A.65 and Figure A.66. The HTC- and temperature distributions in Figure A.65 and Figure A.66 are presented for the engine load case of 170 kW at 4000 RPM.

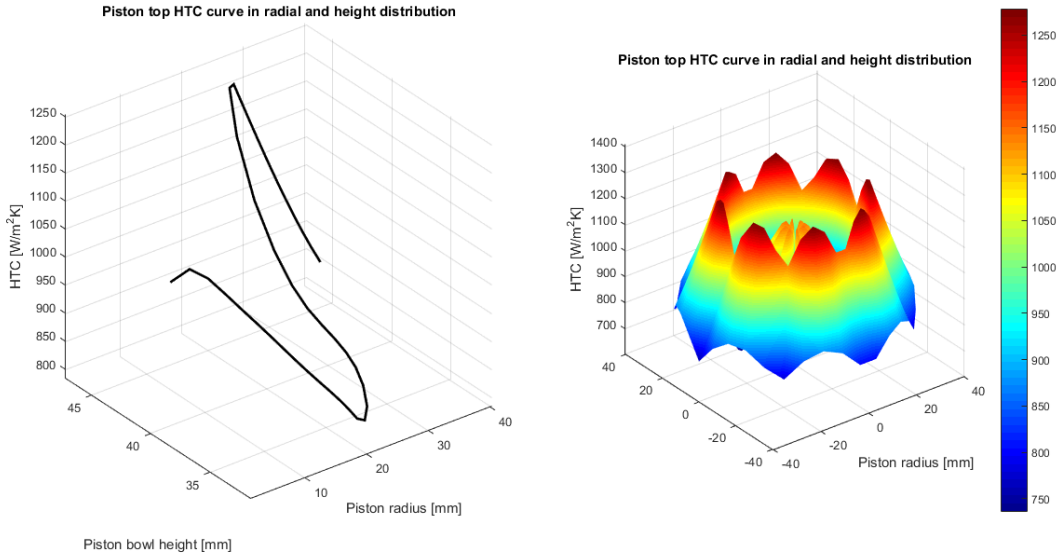

Figure A.65: Piston top load surface HTC distribution for 170 kW at 4000 RPM.

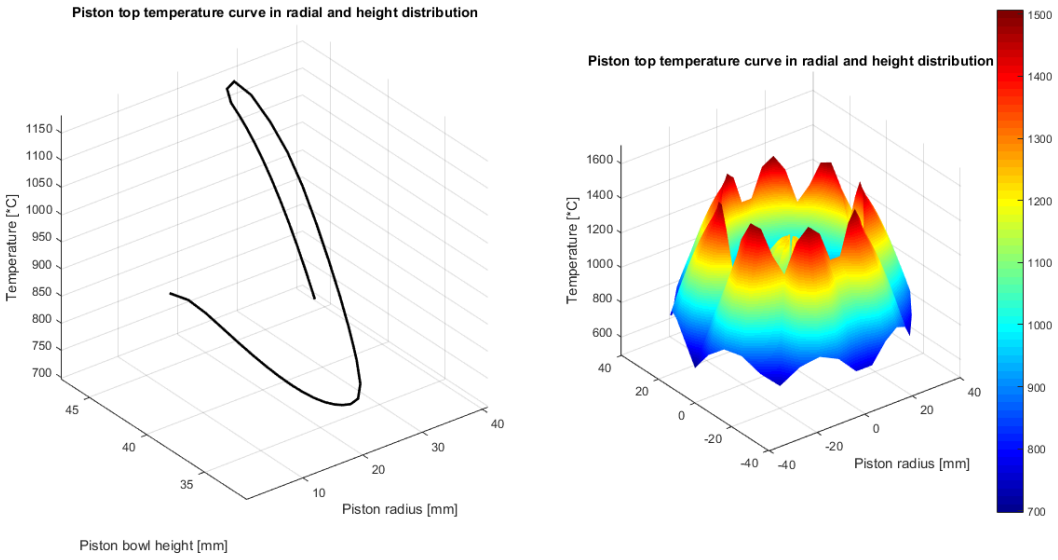

Figure A.66: Piston top load surface temperature distribution for 170 kW at 4000 RPM.

Additionally, the undercrown HTC distribution for 170 kW at 4000 RPM is illustrated in Figure A.67.

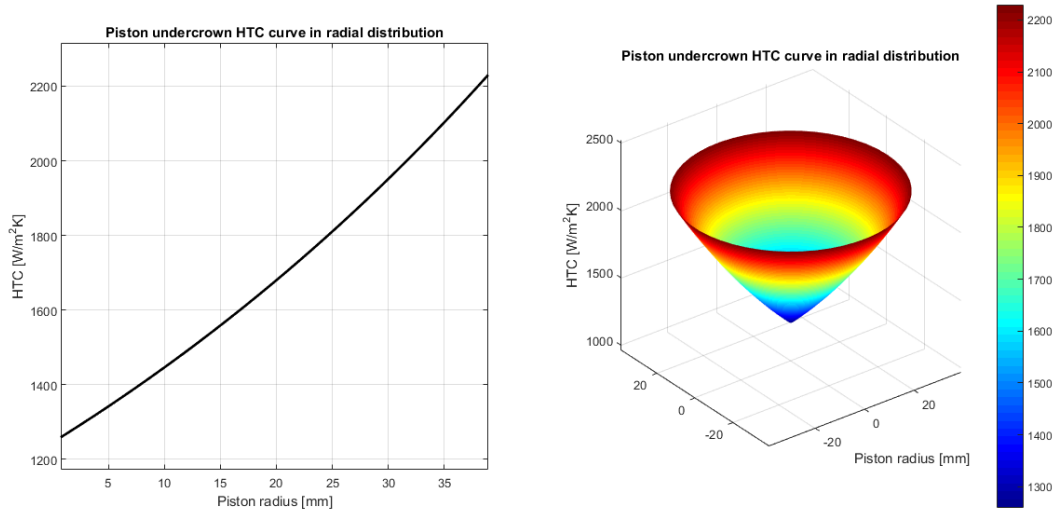

Figure A.67: Piston undercrown HTC distribution for 170 kW at 4000 RPM.